Synthetic [C II] emission maps of a simulated molecular cloud in formation

A. Franeck[1]⋆, S. Walch[1], D. Seifried[1], S. Clarke[1], V. Ossenkopf-Okada[1]
S.C.O. Glover[2], R.S. Klessen[2,3], P. Girichidis[4], T. Naab[5], R. Wünsch[6],
P.C. Clark[7], E. Pellegrini[2], T. Peters[5]

[1] *I. Physikalisches Institut, Universität zu Köln, Zülpicher Straße 77, Germany*
[2] *Universität Heidelberg, Zentrum für Astronomie, Institut für Theoretische Astrophysik, Albert-Ueberle-Straße 2, 69120 Heidelberg, Germany*
[3] *Universität Heidelberg, Institut für wissenschaftliches Rechnen (IWR), Im Neuenheimer Feld 205, 69120 Heidelberg*
[4] *Leibniz-Institut für Astrophysik Potsdam (AIP), An der Sternwarte 16, 14482 Potsdam, Germany*
[5] *Max-Planck-Institut für Astrophysik, Karl-Schwarzschild-Straße 1, 85748 Garching, Germany*
[6] *Astronomical Institute, Czech Academy of Sciences, Bocni II 1401, 141 00 Prague, Czech Republic*
[7] *School of Physics & Astronomy, Cardiff University, 5 The Parade, Cardiff CF24 3AA, Wales, UK*

ABSTRACT

The C^+ ion is an important coolant of interstellar gas, and so the [C II] fine structure line is frequently observed in the interstellar medium. However, the physical and chemical properties of the [C II]-emitting gas are still unclear. We carry out non-LTE radiative transfer simulations with RADMC–3D to study the [C II] line emission from a young, turbulent molecular cloud before the onset of star formation, using data from the SILCC-Zoom project. The [C II] emission is optically thick over 40% of the observable area with $I_{\rm [CII]} > 0.5$ K km s^{-1}. To determine the physical properties of the [C II] emitting gas, we treat the [C II] emission as optically thin. We find that the [C II] emission originates primarily from cold, moderate density gas ($40 \lesssim T \lesssim 65$ K and $50 \lesssim n \lesssim 440$ cm^{-3}), composed mainly of atomic hydrogen and with an effective visual extinction between ~ 0.50 and ~ 0.91. Gas dominated by molecular hydrogen contributes only $\lesssim$20% of the total [C II] line emission. Thus, [C II] is not a good tracer for CO-dark H_2 at this early phase in the cloud's lifetime. We also find that the total gas, H and C^+ column densities are all correlated with the integrated [C II] line emission, with power law slopes ranging from 0.5 to 0.7. Further, the median ratio between the total column density and the [C II] line emission is $Y_{\rm CII} \approx 1.1 \times 10^{21}$ cm^{-2} (K km s^{-1})$^{-1}$, and $Y_{\rm CII}$ scales with $I_{\rm [CII]}^{-0.3}$. We expect $Y_{\rm CII}$ to change in environments with a lower or higher radiation field than simulated here.

Key words: galaxies: ISM – ISM: structure – clouds – astrochemistry – radiative transfer – infrared: ISM

1 INTRODUCTION

The [C II] line of ionized carbon is one of the dominant coolants in the interstellar medium (ISM; Tielens & Hollenbach 1985; Klessen & Glover 2016). It originates from the fine structure transition $^2P_{3/2} \rightarrow {}^2P_{1/2}$ of singly ionized carbon (C^+). The transition occurs at a wavelength of $\lambda_{\rm [CII]} = 157.741$ μm ($\nu_{\rm [CII]} = 1900.537$ GHz). Only 11.26 eV are needed to ionize carbon atoms to C^+, and therefore this ion can coexist with neutral hydrogen, which is ionized by photons with energies equal to or more than 13.6 eV.

On the other hand, 24.4 eV is necessary to bring C^+ into a higher ionization state (Goldsmith et al. 2012; Pineda et al. 2013; Kapala et al. 2015), and so C^+ is still present in the warm, moderately ionized medium. It is therefore not trivial to observationally disentangle from which phase of the ISM the [C II] line emission signal originates.

[C II] line emission accounts for 0.1–1% of the total infrared emission from the Milky Way (Stacey et al. 1991) and is produced in photon dominated regions (PDRs, e.g. Ossenkopf et al. 2013), in shock fronts (Appleton et al. 2013; Lesaffre et al. 2013), but also in forming molecular clouds

⋆ E-mail: franeck@ph1.uni-koeln.de (AF)

(e.g. Beuther et al. 2014). Within the GOT C+ survey[1], the [C II] line emission was studied in the Milky Way along 452 lines of sight, distributed in an approximately volume-weighted fashion in the Galactic plane (Pineda et al. 2013). Analysing these data and correlating the [C II] line emission with the emission of CO and H I, Velusamy & Langer (2014) found that ∼62% of the [C II] line emission is associated with H_2 gas, ∼18% with H I gas and ∼21% with the warm interstellar medium (WIM). However, according to Pineda et al. (2013, 2014) between ∼30% and ∼47% of the [C II] line emission originates from PDRs. Therefore, these values vary depending on the regions analysed. Since the [C II] line emission is observed in connection with molecular clouds, there have been attempts to use it as a tracer for star formation (e.g. De Looze et al. 2011, 2014; Pineda et al. 2014; Herrera-Camus et al. 2015; Kapala et al. 2015) as well as for CO-dark H_2 gas (Wolfire et al. 2010; Langer et al. 2014). However, to judge its suitability as a tracer, it is essential to understand from which phase of the ISM the [C II] line emission originates. In this work we study this question with numerical simulations of a forming molecular cloud, before the onset of star formation.

Synthetic [C II] line observations of the ISM were carried out in earlier studies, e.g. by Accurso et al. (2017). They run a suite of 1D models, coupling STARBURST99 (Leitherer et al. 1999, 2010; Vázquez & Leitherer 2005; Conroy 2013), MOCASSIN (Ercolano et al. 2003) and 3D-PDR (Bisbas et al. 2012) to find the [C II] line emission as a function of e.g. the specific star formation rate, the gas phase metallicity, the electron number density, and the dust mass fraction. For a galaxy in the local neighbourhood they predict 60–80% of the [C II] line emission to originate from regions dominated by molecular gas. Synthetic [C II] line emission studies on the scales of molecular clouds have been carried out by Bisbas et al. (2017) and Bertram et al. (2016). The work of Bisbas et al. (2017) investigates whether [C II] line emission can be used as a tracer for giant molecular cloud collisions. Bertram et al. (2016) study a molecular cloud in a galactic center like environment. They compare the difference in the evolution of the molecular clouds when the virial parameter is changed by varying the amount of kinetic energy in the simulation. Overall, they find that atomic tracers like [C II], [O I] (63 μm) or [O I] (145 μm) accurately reflect most of the physical properties of the H_2 gas and the total gas of the cloud, whereas molecular tracers (^{12}CO or ^{13}CO) do not. Synthetic [C II] line emission studies have also been carried out for star-forming galaxies at high redshift ($z \sim 6$) by e.g. Olsen et al. (2017), who investigate whether the [C II] line emission can be used as a star formation tracer at these epochs. For this purpose they also study the origin of the [C II] line emission and find giant molecular clouds to be the source of a majority of the [C II] emission.

Our work builds on 3D hydrodynamical simulations of a molecular cloud. In the framework of the

SILCC simulations,[2] the evolution of the ISM is modelled self-consistently within a piece of a galactic plane ($0.5\,\mathrm{kpc} \times 0.5\,\mathrm{kpc} \times \pm 5\,\mathrm{kpc}$) with initial conditions inspired by the values of the solar neighbourhood (Walch et al. 2015; Girichidis et al. 2016; Gatto et al. 2015, 2017; Peters et al. 2017). One important feature of these simulations is their use of simplified chemical network, which calculates the non-equilibrium evolution of hydrogen and carbon species within the gas. Based on the SILCC simulations, Seifried et al. (2017) carried out zoom-in simulations of the evolution of two molecular clouds and their chemistry using a greatly improved resolution ($\mathrm{d}x \geqslant 0.122$ pc) as part of the SILCC-Zoom project. In these zoom-in simulations, although high resolution is applied within the molecular cloud region, the surrounding galactic environment is retained, albeit at lower resolution. This allows for the galactic environment to influence the growth of molecular clouds via large-scale turbulent flows in a self-consistent manner.

In this paper, we post-process the results of one of these zoom-in simulations using the RADMC–3D radiative transfer code (Dullemond et al. 2012) in order to produce synthetic [C II] emission maps. Our aim is to understand how much [C II] emission is produced during the formation of a typical molecular cloud and from which regions in the cloud this emission comes. In addition, we briefly discuss the numerical resolution required in order to produce numerical converged predictions for the [C II] emission. We note that, since we do not model the formation of stars within the growing molecular clouds in this work, we are not able to account for the [C II] emission produced in PDRs around newly-formed massive stars. Instead, we concentrate on an earlier stage in the lifetime of the cloud, before massive star formation has fully got underway (as observed in e.g. Beuther et al. 2014). We focus on analysing the origin of the velocity-integrated [C II] line emission, deferring any discussion of [C II] as a kinematic tracer to future work.

The structure of the paper is as follows. In Section 2 Methods section.2, we briefly describe the method for producing the zoom-in simulations and the radiative transfer post-processing. In Section 3 Synthetic emission maps at different resolutions section.3, we investigate the impact of the numerical resolution of the simulations on the synthetic [C II] line emission maps. In Section 4 Origin of the [C II] line emission section.4 we study the origin of the [C II]-emitting gas and try to disentangle its 3D structure. Here, to avoid optical depth effects, we treat the [C II] emission as being optically thin. We then analyse the correlation between the total gas, H and C^+ column densities and the [C II] line emission in Section 5 Correlation with column densities section.5, and close with a discussion and summary of our results in Sections 6 Discussion section.6 and 7 Conclusion section.7.

---

2 METHODS

2.1 SILCC Zoom-in simulations

The simulations of molecular clouds (zoom-ins, SILCC-Zoom project) are based on the SILCC simulations (Walch et al. 2015; Girichidis et al. 2016). The zoom-ins and the applied technique were presented in Seifried et al. (2017, hereafter S17). In the following we briefly describe the numerical methods used. For more details we refer the reader to the aforementioned papers.

The simulations are performed with the adaptive mesh refinement code FLASH 4.3 (Fryxell et al. 2000; Dubey et al. 2008) using a magneto-hydrodynamics solver which guarantees positive entropy and density (Bouchut et al. 2007; Waagan 2009). The chemical evolution of the ISM is modelled using a simplified chemical network for H^+, H, H_2, C^+, CO, e^-, and O (Nelson & Langer 1997; Glover & Mac Low 2007b; Glover & Clark 2012). We do not include high-temperature shock chemistry, as our simulations do not have sufficient resolution to resolve the hot and thin post-shock cooling zones behind highly supersonic shocks. We assume solar metallicity with elemental abundances of carbon and oxygen relative to hydrogen given by 1.4×10^{-4} and 3.16×10^{-4}, respectively (Sembach et al. 2000). The chemical network also follows the thermal evolution of the gas including the most relevant heating and cooling processes. The ISM is embedded in an interstellar radiation field (ISRF) of $G_0 = 1.7$ in units of Habing (1968), that is in line with Draine (1978). The ISRF is shielded in dense regions according to the surrounding column densities of the total gas, dust, H_2, and CO, calculated via the TreeRay OpticalDepth module (Wünsch et al. 2018) based on the TreeCol algorithm (Clark et al. 2012). This enables us to calculate the photochemical reaction rates and radiative heating rates as well as the dust temperature. We solve the Poisson equation for self-gravity with a tree-based method (Wünsch et al. 2018) and include a background potential due to the pre-existing stellar component in the galactic disc, which is modeled as an isothermal sheet with $\Sigma_{star} = 30$ $M_\odot$ pc^{-2} and a scale height of 100 pc (Spitzer 1942).

The SILCC simulation setup represents a small section of a galactic disc with solar neighbourhood properties and a size of 500 pc × 500 pc × ±5 kpc. We apply periodic boundary conditions along the x- and y-directions and outflow conditions along the z-direction, which are Neumann boundary conditions, with the additional requirement that the velocity vector is pointing outwards. Otherwise the velocity is set to zero, thus only allowing for outflow. The initial vertical distribution of the gas has a Gaussian profile with a scale height of 30 pc and a midplane density of 9×10^{-24} g cm^{-3}, which gives us a total gas surface density of $\Sigma_{gas} = 10$ $M_\odot$ pc^{-2}. The gas around the disc midplane has an initial temperature of 4500 K. Hydrogen in this gas is assumed to start in atomic form, while the carbon is present initially as C^+.

From the start we inject SNe up to $t_0 = 11.9$ Myr with a constant rate of 15 SNe Myr^{-1} in order to allow a self-consistent three-phase ISM to develop. This SN rate is chosen in agreement with the Kennicutt-Schmidt star formation rate surface density for $\Sigma_{gas} = 10$ $M_\odot$ pc^{-2} (Schmidt 1959; Kennicutt 1998). Half of the SNe explode within the density peaks, and the other half are randomly placed (mixed driving; see Walch et al. 2015, for more details). For a single SN explosion 10^{51} erg is injected (see Gatto et al. 2015, for more details).

The grid resolution up to t_0 is 3.9 pc. At t_0 we stop the injection of further SNe since we want to study a molecular cloud which is unaffected by SNe in its further evolution. We choose two regions in which molecular clouds (MCs) — henceforth denoted as "zoom-ins", or MC1 and MC2 — are about to form (see S17 for more details). At this point, the zoom-in regions have typical densities below a few times 10 cm^{-3}. We then continue the simulation for another 1.5 Myr and progressively increase the spatial resolution dx in these two regions from the refinement level "L5" with dx = 3.9 pc to the refinement level "L10" with dx = 0.122 pc (see table 2 in S17). In the surroundings of the zoom-ins we retain the SILCC simulation box at the lower resolution of 3.9 pc, thus keeping the effect of accretion onto the cloud from the larger-scale, galactic environment. After reaching the highest resolution level (L10 with dx = 0.122 pc), we continue the simulation at that level. As shown in S17, this resolution is sufficient (and required) to accurately model both the chemical and dynamical evolution of the clouds. Furthermore, this resolution allows us to resolve the filamentary substructure of the clouds.

Since both MC1 and MC2 have qualitatively similar properties, in particular with respect to their [C II] emission, we chose to present our analysis for MC2. In particular, we study MC2 at an evolutionary time of $t_{tot} = t_0 + 2$ Myr = 13.9 Myr. In S17, we present the CO-to-H_2 conversion factor for MC1 and MC2 at t_{tot} = 13.9 Myr (see their figs. 17 and 18). The zoom-in region of MC2 has a size of 104 pc × 88 pc × 71 pc, centred around the midplane. In total, this region contains a gas mass of 8×10^4 $M_\odot$. The mass-weighted mean velocity dispersion of MC2, defined for number density thresholds between 30 cm^{-3} and 300 cm^{-3}, is about 4 km s^{-1} (see fig. 10 in S17).

In order to study the effect of the resolution of the 3D simulation on the obtained [C II] emission, we consider runs with different maximum resolution levels ranging from "L5" to "L10". For this we simply stop the progressive refinement approach at a lower maximum resolution level. In this way we guarantee that except for the different maximum resolution, the individual simulations are as close to each other as possible. In Table 1List of the zoom-in simulations used here, as named in S17 (first column) and named after their resolution level (second column). The third column gives the spatial resolution dx. Further, we list for the $x - z$ projection the integrated peak intensities and total luminosities L_{tot} for the opacity affected and the optically thin [C II] synthetic emission maps (fourth to seventh column, respectively; see Section 3Synthetic emission maps at different resolutionssection.3). table.caption.1 we list all simulations investigated in this work. In column 1, we list the run names as used by S17, where "tau" denotes the further simulation time after starting the refinement

procedure, and "dx" denotes the minimum cell size. In this work, we call the simulations by their maximum resolution level, i.e. "L7" corresponds to run MC2_tau-0.5_dx-1.0 (see column 2).

2.2 Radiative transfer simulations

We post-process the simulations with the radiative transfer code RADMC–3D[3] (Dullemond et al. 2012, version 0.40) to study the signal of the [C II] emission line. Here we briefly sketch the mode of operation of RADMC–3D and refer to Appendix ADetails of the radiative transfer simulationsappendix.A for a more detailed description, and to the manual of RADMC–3D for even more information.

We carry out the radiative transfer for the [C II] line emission at $\nu_{[CII]}$ = 1900.537 GHz ($\lambda_{[CII]}$ = 157.741 μm). Since the [C II] line emission can become optically thick, we calculate in this paper the (i) [C II] line emission that is influenced by opacity and corresponds to the case of [^{12}CII] emission ("opacity affected" case), and (ii) the [C II] line emission that we treat as if it would be optically thin ("optically thin" case). For the latter, we modify the number density of n_{C^+} by dividing it by a factor chosen such that the optically thin [C II] line emission corresponds to the optically thin [^{13}C II] line emission. Following Wakelam & Herbst (2008), the standard isotopic ratio of $^{12}C^+/^{13}C^+$ = 67. The fine structure transition in $^{13}C^+$ splits into three [^{13}C II] hyperfine structure lines $F - F'$ = 2 − 1, 1 − 0, 1 − 1, where F refers to the hyperfine structure level, with intensity ratios of 0.625:0.250:0125 (Ossenkopf et al. 2013). Taking the fraction of the brightest line among these three, we define $n_{C^+,\text{opt. thin}}$ as

$$n_{C^+,\text{opt. thin}} = n_{C^+} \times \frac{0.625}{67}. \qquad (1)$$

We take the same frequency to calculate the [C II] line emission for both the opacity affected and the optically thin case.

RADMC–3D solves the radiative transfer equation under the assumption that the profile function is equal for the emission and absorption (complete redistribution). Absorption and emission are calculated internally, using a Gaussian profile function of the line as well as the fractional level populations of the C^+ ion. We assume that the line is broadened thermally (a_{therm}) and via microturbulence (a_{turb}). We set $a_{\text{turb}} = a_{\text{therm}}$, with $a_{\text{therm}} = \sqrt{\frac{2k_B T}{\mu m_H}}$. Here, T denotes the kinetic temperature, k_B is the Boltzmann constant, m_H is the mass of a hydrogen atom, and μ is the molecular weight of the emitting $^{12}C^+$ particle ($\mu = 12$). We have further investigated whether convergence of our synthetic [C II] emission maps with increasing resolution is improved if we adopt a value of a_{turb} that depends on the size of the grid cell, following eq. 1 in Larson (1981). However, we find that in practice this does not make a significant difference (Appendix BTesting Larson's
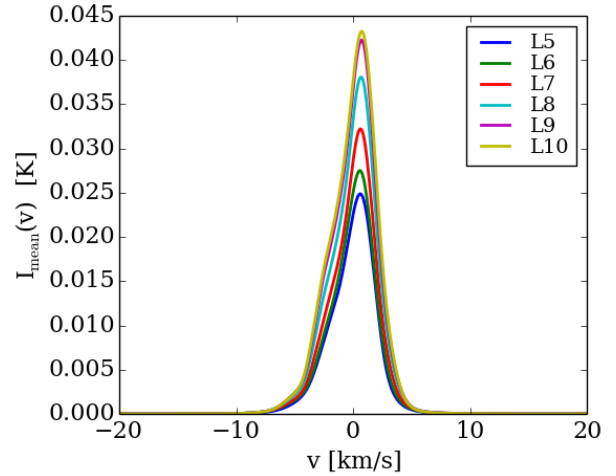
[3] http://www.ita.uni-heidelberg.de/~dullemond/software/radmc-3d/

Figure 1. Averaged [C II] spectra for the opacity affected case of the whole synthetic emission map. 201 velocity channels are chosen in a velocity range of ±20 km s^{-1} (dv = 0.2 km s^{-1}) around the rest frequency of 1900.537 GHz. Different spatial resolutions are colour-coded (see Table 1List of the zoom-in simulations used here, as named in S17 (first column) and named after their resolution level (second column). The third column gives the spatial resolution dx. Further, we list for the $x − z$ projection the integrated peak intensities and total luminosities L_{tot} for the opacity affected and the optically thin [C II] synthetic emission maps (fourth to seventh column, respectively; see Section 3Synthetic emission maps at different resolutionssection.3). table.caption.1).

microturbulenceappendix.B).

In a low density medium the population of the energy levels of C^+ does not correspond to the thermal distribution, and thus we do not assume local thermal equilibrium (LTE) in our calculations. In order to calculate the level populations of C^+ for the upper and lower levels, we therefore consider collisions with molecular hydrogen (ortho-H$_2$ and para-H$_2$), atomic hydrogen, and electrons (Goldsmith et al. 2012; Lique et al. 2013). We use the large velocity gradient (LVG) approximation (see Shetty et al. 2011a,b), i.e. lines_mode = 3 of RADMC–3D. We tested several maximum values for the Sobolev length (2 pc and 70 pc) and found that this has a negligible impact on our results (Appendix CTesting escape probability lengthsappendix.C). In regions of dense gas the level populations approach their LTE values.

In order to capture the contribution of Doppler-shifted emission, we consider a velocity range of ±20 km s^{-1}, centred around $\nu_{[CII]}$. We divide this range into 201 equally spaced velocity channels, corresponding to a spectral resolution of dv = 0.2 km s^{-1}. The choice of this spectral resolution is inspired by the *Herschel* observations of the [C II] line emission in Orion (Goicoechea et al. 2015, with dv = 0.2 km s^{-1}). In Appendix DSpectral resolutionappendix.D we test different spectral resolutions.The radiative transfer calculation is done for every pixel in the projected image. The spatial resolution of the synthetic emission maps corresponds to the maximum resolution dx, as listed in Table 1List of the zoom-in simulations used here, as named in S17 (first column) and

Table 1. List of the zoom-in simulations used here, as named in S17 (first column) and named after their resolution level (second column). The third column gives the spatial resolution dx. Further, we list for the $x - z$ projection the integrated peak intensities and total luminosities $L_{\rm tot}$ for the opacity affected and the optically thin [C II] synthetic emission maps (fourth to seventh column, respectively; see Section 3Synthetic emission maps at different resolutionssection.3).

Run name in S17	resolution level	dx	[C II], opac. aff.		[C II], opt. thin	
			$I_{\rm peak}$	$L_{\rm tot}$	$I_{\rm peak}$	$L_{\rm tot}$
		[pc]	[K km s^{-1}]	[L$_\odot$]	[K km s^{-1}]	[L$_\odot$]
MC2_dx-3.9	L5	3.9	1.36	353	0.01	3.00
MC2_tau-0.0_dx-2.0	L6	2	1.90	390	0.02	3.45
MC2_tau-0.5_dx-1.0	L7	1	3.60	459	0.04	4.23
MC2_tau-1.0_dx-0.5	L8	0.5	5.82	555	0.06	5.30
MC2_tau-1.25_dx-0.24	L9	0.25	10.30	628	0.12	6.14
MC2_tau-1.5_dx-0.12	L10	0.122	10.56	652	0.21	6.52

named after their resolution level (second column). The third column gives the spatial resolution dx. Further, we list for the $x - z$ projection the integrated peak intensities and total luminosities $L_{\rm tot}$ for the opacity affected and the optically thin [C II] synthetic emission maps (fourth to seventh column, respectively; see Section 3Synthetic emission maps at different resolutionssection.3). table.caption.1. Figure 1Averaged [C II] spectra for the opacity affected case of the whole synthetic emission map. 201 velocity channels are chosen in a velocity range of ± 20 km s^{-1} (d$v = 0.2$ km s^{-1}) around the rest frequency of 1900.537 GHz. Different spatial resolutions are colour-coded (see Table 1List of the zoom-in simulations used here, as named in S17 (first column) and named after their resolution level (second column). The third column gives the spatial resolution dx. Further, we list for the $x - z$ projection the integrated peak intensities and total luminosities $L_{\rm tot}$ for the opacity affected and the optically thin [C II] synthetic emission maps (fourth to seventh column, respectively; see Section 3Synthetic emission maps at different resolutionssection.3). table.caption.1).figure.caption.2 depicts the averaged spectrum of MC2 at different resolution levels (colour-coded). The average spectrum shows the mean intensity calculated over the whole zoom-in region in each velocity channel. Most of the emission comes from velocities between ± 10 km s^{-1}. With an increasing resolution level the maximum of the averaged spectrum grows and converges for the higher resolution levels L9 and L10. As described in Section 3Synthetic emission maps at different resolutionssection.3, the density within the simulation increases with increasing resolution, resulting in higher intensities.

We provide RADMC–3D with the collisional rates and the number densities of C$^+$ and its collisional partners as well as with the gas temperatures in order to carry out the radiative transfer calculation. In the following we discuss these input parameters in more detail.

2.2.1 Collisional rates

The de-excitation rate coefficients of ortho- and para-molecular hydrogen, atomic hydrogen and electrons with C$^+$ are taken from the Leiden Atomic and Molecular Database[4] (LAMDA, Schöier et al. 2005), and extrapolated to higher temperatures following Goldsmith et al. (2012). RADMC–3D converts the de-excitation rates internally into excitation rates as described in Appendix ADetails of the radiative transfer simulationsappendix.A. Since the temperature ranges present in the SILCC simulations are larger than the temperature ranges for which the coefficients are given, we extrapolate the de-excitation rate coefficients to higher temperatures. A detailed description of how we obtain the collisional rates is presented in Appendix ADetails of the radiative transfer simulationsappendix.A.

2.2.2 Number densities

To obtain information about the number densities within the zoom-in region, we convert the FLASH data to RADMC–3D input data. The information of the FLASH grid structure within the zoom-in region is passed to the RADMC–3D input data by creating an oct-tree structured binary file. This is identical to the original FLASH grid structure. Compared to an uniform grid structure at the highest resolution, the oct-tree structure allows us to reduce the memory requirements. The RADMC–3D input data only include the information of the zoom-in region of $(104 \times 88 \times 71)$ pc^3. By this we ensure that we study only the emission from the molecular cloud itself and that we are not contaminated by fore- and background emission from unresolved regions.
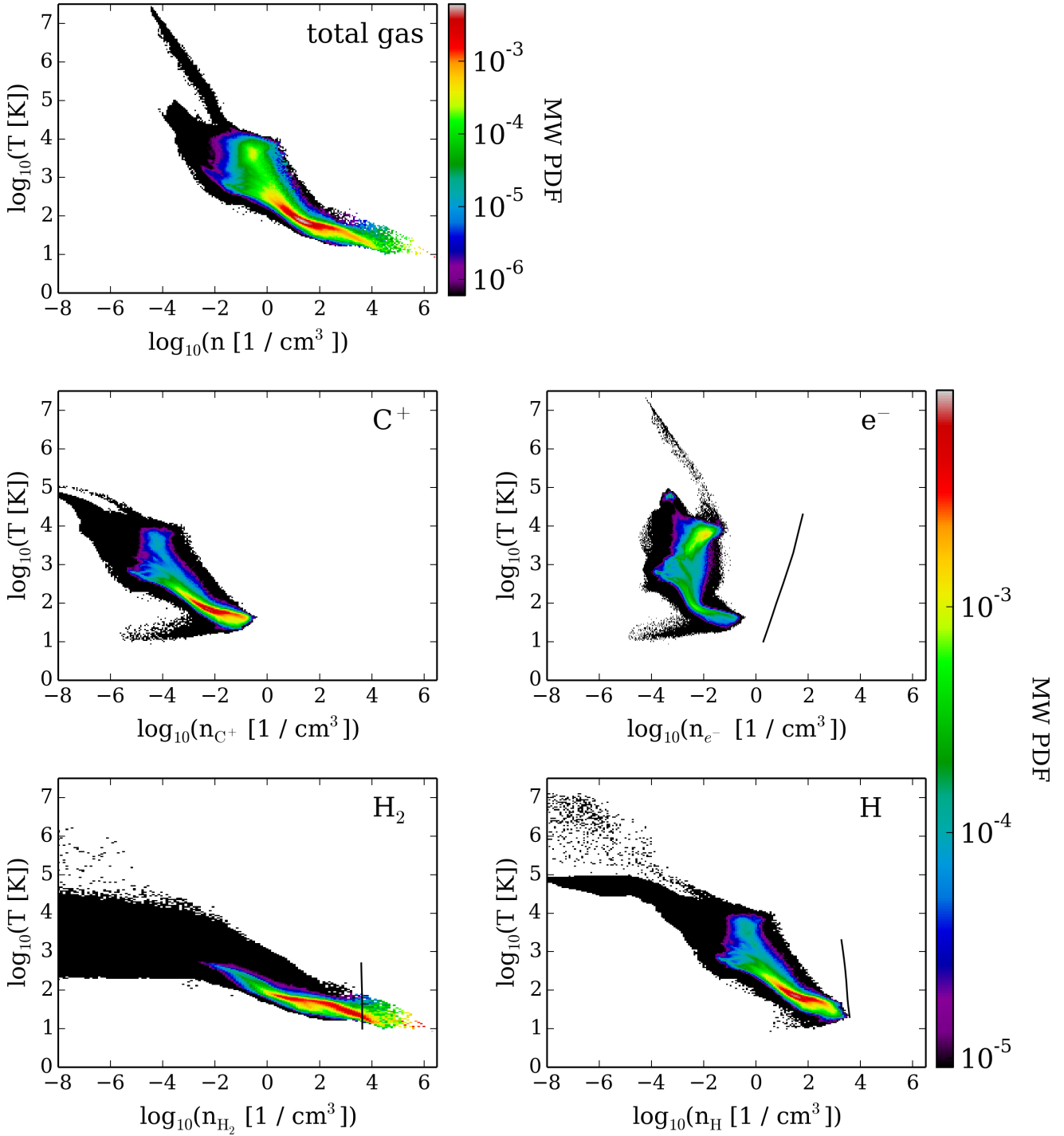
Figure 2Mass-weighted 2D-PDFs as a function of the total gas temperature T and number density of each chemical species in the L10 simulation for the total gas (upper left panel), and for C$^+$ and its primary collisional partners, e^-, H$_2$, and H (as indicated in the plots). The colour-coding shows the mass fraction normalized to the total gas mass of the respective species. The black lines indicate the critical densities of each collisional partner. For all but H$_2$ the number densities of the individual collisional partners are below the critical densities. We therefore expect the excitation of C$^+$ to be subthermal in all gas apart from regions which are dominated by H$_2$.figure.caption.3 illustrates the mass-weighted 2D probability distribution function (2D-PDF, equivalent to a

---
[4] http://home.strw.leidenuniv.nl/~moldata/

Figure 2. Mass-weighted 2D-PDFs as a function of the total gas temperature T and number density of each chemical species in the L10 simulation for the total gas (upper left panel), and for C^+ and its primary collisional partners, e^-, H_2, and H (as indicated in the plots). The colour-coding shows the mass fraction normalized to the total gas mass of the respective species. The black lines indicate the critical densities of each collisional partner. For all but H_2 the number densities of the individual collisional partners are below the critical densities. We therefore expect the excitation of C^+ to be subthermal in all gas apart from regions which are dominated by H_2.

two-dimensional histogram)[5] of the L10 simulation for

the total gas (upper left panel), as well as for C^+, e^-,

[5] In a two-dimensional mass-weighted PDF we show a parameter space of two quantities, and plot how the mass is distributed

within this parameter space. The colour-coding indicates the fraction of mass.

H$_2$ and H (lower four panels). The 2D-PDFs show the distributions of the gas as a function of the number density of each chemical species and the gas temperature, with bin sizes of $\Delta\log_{10}(T) = 0.03$, $\Delta\log_{10}(n\ [\mathrm{cm}^{-3}]) = 0.05$, $\Delta\log_{10}(n_{\mathrm{C+}}\ [\mathrm{cm}^{-3}]) = 0.06$, $\Delta\log_{10}(n_e\ [\mathrm{cm}^{-3}]) = 0.02$, $\Delta\log_{10}(n_{\mathrm{H_2}}) = 0.1$ and $\Delta\log_{10}(n_{\mathrm{H}}\ [\mathrm{cm}^{-3}]) = 0.07$. We derive the number densities of the chemical species in the following way:

$n_{\mathrm{C+}}$: The simplified chemical model used in the SILCC simulations does not include higher ionization states of carbon such as C^{2+} or C^{3+}. If we simply were to take the C$^+$ abundance from the simulation data, we would therefore overestimate the C$^+$ number density in gas warmer than $T \sim 20\,000$ K. To correct for this, we post-process the C$^+$ number densities obtained from the SILCC simulations by applying an ionization correction factor (ICF). The ICF is taken from Sutherland & Dopita (1993, fig. 3 therein) and assumes collisional ionization equilibrium (CIE). By multiplying the C$^+$ number density from the simulation with the ICF, it is reduced in gas with $T > 20\,000$ K and for $T > 200\,000$ K all carbon is in a multiply ionized state. The resulting C$^+$ number density is denoted with $n_{\mathrm{C+}}$. We expect this procedure to have a minor impact on the resulting synthetic emission maps, since the density of the hot gas is very low. The resulting 2D-PDF for C$^+$ is shown in the middle left panel of Fig. 2Mass-weighted 2D-PDFs as a function of the total gas temperature T and number density of each chemical species in the L10 simulation for the total gas (upper left panel), and for C$^+$ and its primary collisional partners, e^-, H$_2$, and H (as indicated in the plots). The colour-coding shows the mass fraction normalized to the total gas mass of the respective species. The black lines indicate the critical densities of each collisional partner. For all but H$_2$ the number densities of the individual collisional partners are below the critical densities. We therefore expect the excitation of C$^+$ to be subthermal in all gas apart from regions which are dominated by H$_2$.figure.caption.3.

n_{e^-}: The middle right panel of Fig. 2Mass-weighted 2D-PDFs as a function of the total gas temperature T and number density of each chemical species in the L10 simulation for the total gas (upper left panel), and for C$^+$ and its primary collisional partners, e^-, H$_2$, and H (as indicated in the plots). The colour-coding shows the mass fraction normalized to the total gas mass of the respective species. The black lines indicate the critical densities of each collisional partner. For all but H$_2$ the number densities of the individual collisional partners are below the critical densities. We therefore expect the excitation of C$^+$ to be subthermal in all gas apart from regions which are dominated by H$_2$.figure.caption.3 shows the 2D-PDF for the electrons. We assume that the gas is electrically neutral overall, which means that the number density of free electrons must balance the total number density of ions. Therefore, the two ions we track in our chemical model, H$^+$ and C$^+$, determine the electron number density. Since the fraction of carbon is very low compared to the fraction of hydrogen in the simulations, H$^+$ is the main donor of electrons in highly ionized regions. In cold gas, the H$^+$ abundance can become very small; in these conditions, C$^+$ provides most of the free electrons.

We therefore have

$$n_e = n_{\mathrm{H+}} + n_{\mathrm{C+}}. \tag{2}$$

This expression neglects the contribution to n_e from other metals with ionization potentials below 13.6 eV (e.g. Si, Mg, Fe), but in regions where C$^+$ is abundant, this is at most a small correction. In dense gas with a low C$^+$ abundance, these low ionization potential metals can contribute a much larger fraction of the total electron abundance, but these regions produce little [C II] emission.

$n_{\mathrm{H_2}}$: The number density of H$_2$ is taken directly from the simulation (Fig. 2Mass-weighted 2D-PDFs as a function of the total gas temperature T and number density of each chemical species in the L10 simulation for the total gas (upper left panel), and for C$^+$ and its primary collisional partners, e^-, H$_2$, and H (as indicated in the plots). The colour-coding shows the mass fraction normalized to the total gas mass of the respective species. The black lines indicate the critical densities of each collisional partner. For all but H$_2$ the number densities of the individual collisional partners are below the critical densities. We therefore expect the excitation of C$^+$ to be subthermal in all gas apart from regions which are dominated by H$_2$.figure.caption.3, lower left panel). Additionally, we distinguish between the two nuclear spin states of H$_2$, in which the spins of the nuclei are parallel ($I = 1$, ortho-H$_2$) or antiparallel ($I = 0$, para-H$_2$). When many different rotational levels are populated (e.g. at high temperatures and densities), the equilibrium ortho-to-para ratio is given by the ratio of the nuclear statistical weights $g_I = 2I + 1$ and hence, it is 3:1. At low temperatures ($T \lesssim 150$ K), where only the $J = 0$ and $J = 1$ rotational levels are populated, the ortho-to-para ratio is given instead by (Rachford et al. 2009)

$$\frac{n(\text{ortho-H}_2)}{n(\text{para-H}_2)} = 9 \cdot e^{-171\,\mathrm{K}/T_{\mathrm{rot}}}, \tag{3}$$

where T_{rot} is the rotational temperature. We here use the kinetic temperature T_{kin} as an approximation for T_{rot}. Although this is a rough estimate, it is sufficient for our purpose, since the collisional rates for ortho-H$_2$ and para-H$_2$ are similar and distinguishing between them has only a minor impact on the [C II] line emission.

n_{H}: The number density of atomic hydrogen is taken directly from the SILCC simulation.

The black lines in the 2D-PDFs of the collisional partners in Fig. 2Mass-weighted 2D-PDFs as a function of the total gas temperature T and number density of each chemical species in the L10 simulation for the total gas (upper left panel), and for C$^+$ and its primary collisional partners, e^-, H$_2$, and H (as indicated in the plots). The colour-coding shows the mass fraction normalized to the total gas mass of the respective species. The black lines indicate the critical densities of each collisional partner. For all but H$_2$ the number densities of the individual collisional partners are below the critical densities. We therefore expect the excitation of C$^+$ to be subthermal in all gas apart from regions which are dominated by H$_2$.figure.caption.3 indicate the critical densities. The critical density (Tielens & Hollenbach (1985) or Draine (2011), chapter 17.2) is defined as the ratio of the spontaneous emission rate — described by the Einstein

coefficient A_{ul} — and the collisional de-excitation rate coefficient R_{ul} — with

$$n_{\mathrm{crit}} = \frac{A_{ul}}{R_{ul}}. \qquad (4)$$

Since the size of R_{ul} depends on the collision partner, we obtain a different critical density for each main collision partner. If the number density of any of these collision partners exceeds the corresponding critical density, then collisional de-excitation occurs more rapidly on average than radiative de-excitation. In these conditions, the C^+ level populations approach their LTE values. From Fig. 2Mass-weighted 2D-PDFs as a function of the total gas temperature T and number density of each chemical species in the L10 simulation for the total gas (upper left panel), and for C^+ and its primary collisional partners, e^-, H_2, and H (as indicated in the plots). The colour-coding shows the mass fraction normalized to the total gas mass of the respective species. The black lines indicate the critical densities of each collisional partner. For all but H_2 the number densities of the individual collisional partners are below the critical densities. We therefore expect the excitation of C^+ to be subthermal in all gas apart from regions which are dominated by H_2.figure.caption.3, we see that in some regions (although not everywhere), H_2 has a number density greater than $n_{\mathrm{crit,H_2}}$. On the other hand, hydrogen atoms and electrons always have number densities less than their corresponding critical densities. Therefore, we expect C^+ to be subthermally excited in regions dominated by atomic or ionized hydrogen, but to be thermally excited in dense molecular regions.

3 SYNTHETIC EMISSION MAPS AT DIFFERENT RESOLUTIONS

With the method described above we obtain channel maps for each frequency in the velocity range ± 20 km s^{-1} for a snapshot of MC2 at an evolutionary time of $t_{\mathrm{tot}} = t_0 + 2\,\mathrm{Myr} = 13.9$ Myr. We integrate the intensity over the whole velocity range and refer to the resulting maps as synthetic emission maps. In the first row of Fig. 3Synthetic [C II] emission maps (opacity affected case, first row) of MC2 in the zoom-in region of $(104 \times 88 \times 71)\,\mathrm{pc}^3$ at the resolution level L10 shown for all three projections, as indicated above the images. The following rows present the C^+, CO, H, H_2, and total gas column density of the cloud, respectively. The [C II] emission mostly traces the atomic hydrogen column density.figure.caption.4, the opacity affected [C II] synthetic emission maps are shown for MC2 at the maximum refinement level L10. The integrated intensity is colour-coded and presented in units of [K km s^{-1}]. The three columns show the cloud in different projections (as indicated above the columns). The second to sixth rows show the C^+, CO, H, H_2 and total gas column densities of the cloud. H_2 is present in almost all regions of the molecular cloud, and H in the envelopes of these regions. CO forms at even higher visual extinction and is therefore only present in the dense parts of the molecular cloud (cf. Röllig et al. 2007; Glover et al. 2010; Smith et al. 2014; Duarte-Cabral & Dobbs 2016; Xu et al. 2016, S17). Since no atomic carbon is considered in the chemical network, we might slightly overestimate the production of CO and

consequently underestimate the amount of C^+ present in dense gas (Glover & Clark 2012). C^+, as the left-over from carbon that is not in the form of CO, is distributed in most parts of the cloud and is only reduced in dense regions, where CO is present. The [C II] line emission recovers in general the density structure of the cloud. However, in regions with high column densities, $N \gtrsim 10^{23}$ cm^{-2}, CO becomes abundant, C^+ is reduced and therefore also the [C II] line emission drops. One example for this can be seen in the center of the synthetic emission map for the $y - z$ projection (third column).

In Table 1List of the zoom-in simulations used here, as named in S17 (first column) and named after their resolution level (second column). The third column gives the spatial resolution dx. Further, we list for the $x - z$ projection the integrated peak intensities and total luminosities L_{tot} for the opacity affected and the optically thin [C II] synthetic emission maps (fourth to seventh column, respectively; see Section 3Synthetic emission maps at different resolutionssection.3). table.caption.1 we list the maximum intensities as well as the luminosities of the maps, and in Fig. 4Histogram of the integrated [C II] intensity for the $x - z$ projection for the opacity affected case (left) and the optically thin case (middle). X_i/X_{tot} denotes the fraction of pixels in a given intensity bin. The different resolutions are colour-coded (see Table 1List of the zoom-in simulations used here, as named in S17 (first column) and named after their resolution level (second column). The third column gives the spatial resolution dx. Further, we list for the $x - z$ projection the integrated peak intensities and total luminosities L_{tot} for the opacity affected and the optically thin [C II] synthetic emission maps (fourth to seventh column, respectively; see Section 3Synthetic emission maps at different resolutionssection.3). table.caption.1). The histograms converge for a resolution level higher than L9. In the right panel, we compare the histograms of the opacity affected and optically thin [C II] line emission. To bring the intensities to a comparable range, we scale the optically thin emission by a factor of 107, according to Eq. (1Radiative transfer simulationsequation.2.1). The histograms are identical, except in the range for $I_{\mathrm{[CII]}} \geqslant 0.1$ K km s^{-1}, where the emission is optically thick.figure.caption.5 we show the histogram of the integrated [C II] intensities (with a bin size of $\Delta \log_{10}(I\,[\mathrm{K\,km\,s^{-1}}]) = 0.05$) for the $x - z$ projection for the opacity affected emission (left) and the optically thin emission (middle). The distributions demonstrate that the maximum integrated intensity increases with refinement level. The distributions of all maps slowly converge for L9 and higher, in particular for the opacity affected case. Otherwise the optically thin case, which is a proxy for the [^{13}C II] emission, resembles the opacity affected case. These findings are in line with the averaged spectrum in Fig. 1Averaged [C II] spectra for the opacity affected case of the whole synthetic emission map. 201 velocity channels are chosen in a velocity range of ± 20 km s^{-1} (d$v = 0.2$ km s^{-1}) around the rest frequency of 1900.537 GHz. Different spatial resolutions are colour-coded (see Table 1List of the zoom-in simulations used here, as named in S17 (first column) and named after their resolution level (second column). The third column gives the spatial resolution dx.
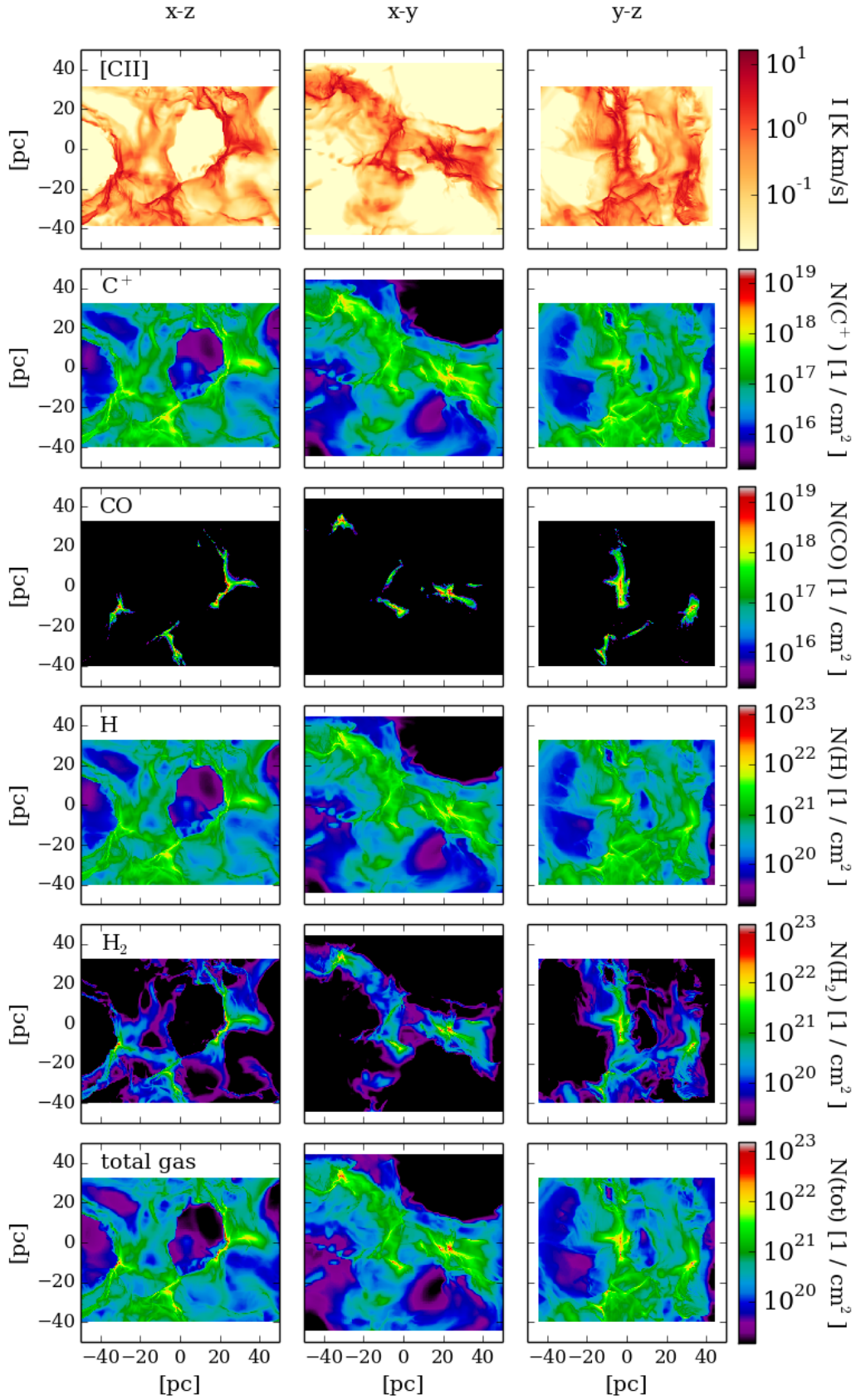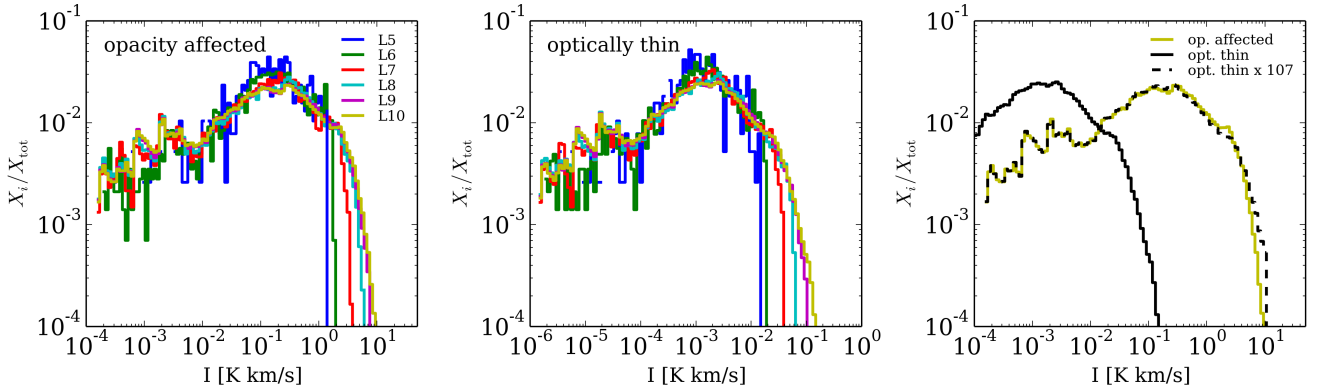
Figure 3. Synthetic [C II] emission maps (opacity affected case, first row) of MC2 in the zoom-in region of $(104 \times 88 \times 71)\,\mathrm{pc}^3$ at the resolution level L10 shown for all three projections, as indicated above the images. The following rows present the C^+, CO, H, H_2, and total gas column density of the cloud, respectively. The [C II] emission mostly traces the atomic hydrogen column density.

Figure 4. Histogram of the integrated [C II] intensity for the $x - z$ projection for the opacity affected case (left) and the optically thin case (middle). X_i/X_{tot} denotes the fraction of pixels in a given intensity bin. The different resolutions are colour-coded (see Table 1List of the zoom-in simulations used here, as named in S17 (first column) and named after their resolution level (second column). The third column gives the spatial resolution dx. Further, we list for the $x - z$ projection the integrated peak intensities and total luminosities L_{tot} for the opacity affected and the optically thin [C II] synthetic emission maps (fourth to seventh column, respectively; see Section 3Synthetic emission maps at different resolutionssection.3). table.caption.1). The histograms converge for a resolution level higher than L9. In the right panel, we compare the histograms of the opacity affected and optically thin [C II] line emission. To bring the intensities to a comparable range, we scale the optically thin emission by a factor of 107, according to Eq. (1Radiative transfer simulationsequation.2.1). The histograms are identical, except in the range for $I_{[CII]} \geqslant 0.1$ K km s^{-1}, where the emission is optically thick.

Further, we list for the $x - z$ projection the integrated peak intensities and total luminosities L_{tot} for the opacity affected and the optically thin [C II] synthetic emission maps (fourth to seventh column, respectively; see Section 3Synthetic emission maps at different resolutionssection.3). table.caption.1).figure.caption.2, where the peak intensity increases with the higher resolution. In the right panel of Fig. 4Histogram of the integrated [C II] intensity for the $x - z$ projection for the opacity affected case (left) and the optically thin case (middle). X_i/X_{tot} denotes the fraction of pixels in a given intensity bin. The different resolutions are colour-coded (see Table 1List of the zoom-in simulations used here, as named in S17 (first column) and named after their resolution level (second column). The third column gives the spatial resolution dx. Further, we list for the $x - z$ projection the integrated peak intensities and total luminosities L_{tot} for the opacity affected and the optically thin [C II] synthetic emission maps (fourth to seventh column, respectively; see Section 3Synthetic emission maps at different resolutionssection.3). table.caption.1). The histograms converge for a resolution level higher than L9. In the right panel, we compare the histograms of the opacity affected and optically thin [C II] line emission. To bring the intensities to a comparable range, we scale the optically thin emission by a factor of 107, according to Eq. (1Radiative transfer simulationsequation.2.1). The histograms are identical, except in the range for $I_{[CII]} \geqslant 0.1$ K km s^{-1}, where the emission is optically thick.figure.caption.5 we directly compare the histograms of the opacity affected and optically thin [C II] integrated intensities. Note, that in order to compare the intensities, we scaled the optically thin [C II] line emission by a factor of 107, in line with Eq. (1Radiative transfer simulationsequation.2.1). Only for intensities of $I_{[CII]} \geqslant 0.1$ K km s^{-1}, where the emission becomes partially optically thick, some minor differences are visible. Further convergence studies for the synthetic [C II]

emission maps are presented in Appendix E1Convergence of the emission mapssubsection.E.1. There we show the synthetic emission maps for the opacity affected and optically thin [C II] line emission in Figs. E1Synthetic [C II] line emission maps (opacity affected) of the zoom-in simulation at different resolution levels as listed in Table 1List of the zoom-in simulations used here, as named in S17 (first column) and named after their resolution level (second column). The third column gives the spatial resolution dx. Further, we list for the $x - z$ projection the integrated peak intensities and total luminosities L_{tot} for the opacity affected and the optically thin [C II] synthetic emission maps (fourth to seventh column, respectively; see Section 3Synthetic emission maps at different resolutionssection.3). table.caption.1. The crosses mark the position with the maximum integrated intensity in each map. From the refinement level L5 to L9 this position changes due to varying optical depths. figure.caption.24 and E2Similar to Fig. E1Synthetic [C II] line emission maps (opacity affected) of the zoom-in simulation at different resolution levels as listed in Table 1List of the zoom-in simulations used here, as named in S17 (first column) and named after their resolution level (second column). The third column gives the spatial resolution dx. Further, we list for the $x - z$ projection the integrated peak intensities and total luminosities L_{tot} for the opacity affected and the optically thin [C II] synthetic emission maps (fourth to seventh column, respectively; see Section 3Synthetic emission maps at different resolutionssection.3). table.caption.1. The crosses mark the position with the maximum integrated intensity in each map. From the refinement level L5 to L9 this position changes due to varying optical depths. figure.caption.24, the synthetic [C II] line emission maps for the optically thin case. The crosses mark the position with the maximum integrated intensity in each map. Here, the position remains in the same area from L6 on, as the emission is optically thin. figure.caption.25, respectively. In

addition we analyse the convergence between the resolution levels and find that the synthetic emission maps of L9 and L10 converge to within 0.5%, as calculated over the whole map.

Further, we investigate the optical depth for the [C II] line emission. With RADMC–3D we calculate whether the emission along a line of sight becomes optically thick ($\tau_{\rm [CII]} \geqslant 1$) for a specific wavelength. We find optically depths up to $\tau \leqslant 10$ in our simulation. The sum over all the channels that contain optically thick emission along one line-of-sight defines the velocity range Δv, which is colour-coded in Fig. 5Maps of the different projections for L10, showing where the [C II] line emission becomes optically thick ($\tau_{\rm [CII]} \geqslant 1$) in at least one velocity channel. The colour-coding shows the width in velocity space over which the emission is optically thick. The black contours mark the observable area for which $I_{\rm [CII]} \geqslant 0.5$ K km s^{-1}. About 39%, 34% and 47% of the observable area is optically thick for the projections $x - z$, $x - y$ and $y - z$, respectively.figure.caption.6. In all projections around 10% of the total area is optically thick, accounting for 45%, 54% and 40% of the total luminosity in the $x - z$, $x - y$ and $y - z$ projections, respectively. However, large portions of the synthetic [C II] emission maps show low integrated intensities, as can be seen in Fig. 3Synthetic [C II] emission maps (opacity affected case, first row) of MC2 in the zoom-in region of $(104 \times 88 \times 71)\,\mathrm{pc}^3$ at the resolution level L10 shown for all three projections, as indicated above the images. The following rows present the C$^+$, CO, H, H$_2$, and total gas column density of the cloud, respectively. The [C II] emission mostly traces the atomic hydrogen column density.figure.caption.4 (first row). We assume that pixels with integrated intensities $I_{\rm [CII]} \geqslant 0.5$ K km s^{-1} are observable.[6] In the following, we call the area with integrated intensities $I_{\rm [CII]} \geqslant 0.5$ K km s^{-1} "observable area", as opposed to the "total area" of the map. By accounting now only for pixels fulfilling $I_{\rm [CII]} \geqslant 0.5$ K km s^{-1} (black contours), about 21%, 16% and 27% of the total map are observable in the $x - z$, $x - y$ and $y - z$ projection. This observable area contains about 80% of the total luminosity. If we consider only this observable region, we find that about 39%, 34% and 47% of the observable area is optically thick in the three projections.

---

[6] This number is roughly comparable with the 3σ detection limits of Velusamy & Langer (2014) and Croxall et al. (2012). For example, in the work of Croxall et al. (2012), [C II] maps from nearby spiral galaxies are studied, observed with the PACS instrument on board of the *Herschel* satellite. They report a 3σ detection limit of approximately 0.04×10^{-7} W m^{-2} sr^{-1} = 4×10^{-6} erg s^{-1} sr^{-1} cm^{-2}. In temperature units, this is equivalent to the integrated intensity 0.57 K km s^{-1}. Better sensitivities can be achieved for observations of [C II] concentrating on one or a few pointings, but a value of 0.5 K km s^{-1} remains representative of the limiting sensitivity that can be achieved in extended maps of [C II] with current facilities.

4 ORIGIN OF THE [C II] LINE EMISSION

We aim to study how much of the [C II] line emission originates from gas in different temperature and density regimes. In Fig. 5Maps of the different projections for L10, showing where the [C II] line emission becomes optically thick ($\tau_{\rm [CII]} \geqslant 1$) in at least one velocity channel. The colour-coding shows the width in velocity space over which the emission is optically thick. The black contours mark the observable area for which $I_{\rm [CII]} \geqslant 0.5$ K km s^{-1}. About 39%, 34% and 47% of the observable area is optically thick for the projections $x - z$, $x - y$ and $y - z$, respectively.figure.caption.6 we have shown that the [C II] line emission is affected by optical depth effects in 10% of the total area and $\sim$40% of the observable area ($I_{\rm [CII]} \geqslant 0.5$ K km s^{-1}), respectively. Hence, we analyse the origin of the [C II] line emission for both, the opacity affected and the optically thin cases, and for the total as well as the observable area. With the optically thin tracer we eliminate optical depth effects and demonstrate that our results are not biased by them. Essentially, we find that both analyses yield qualitatively similar results. This behaviour is in line with the findings of Goldsmith et al. (2012), where the sufficiently weak integrated [C II] line emission is proportional to the C$^+$ column density along a line of sight. Goldsmith et al. (2012) call this behaviour "effectively optically thin". We present the differences between the opacity affected and optically thin [C II] line emission on the example of the origin of the emission as a function of the gas temperature (see Sec. 4.1Temperature dependencesubsection.4.1) and carry out all following analyses with the optically thin [C II] line. The results for all analyses are summarized in Tables 2Summary of the parameter space of the [C II] emitting gas, analysed for the optically thin [C II] line emission. We give the values of $T_{\rm kin}$, n, the fractional abundance of H$_2$ ($x_{\rm H_2}$), and the visual extinction (A$_{\rm V}$) at which 25%, 50% (median) and 75% of the total luminosity are reached. The corresponding plots are shown in Figs. 7*Upper row, left:* Plot of the optically thin [C II] line luminosity originating from gas with $T \leqslant T_i$ for the total map (solid line) and the assumed observable region (dashed line). The cyan line represents the expectation if all of the C$^+$ ions were in LTE. The red shaded area and the grey, dashed vertical line mark the interquartile range and the median of the distribution derived for the total map. *Upper row, right:* The slope of the cumulative luminosity distribution, derived by taking the derivative of the luminosity with respect to the temperature. Most of the emission comes from $40 \lesssim T \lesssim 60$ K. *Bottom row, left:* Mass-weighted temperature distributions of the included species. $M_i/M_{\rm species,\ tot}$ indicates the mass fraction of every species with respect to the total hydrogen, carbon or electron mass, respectively. All collisional partners (H$_2$, H, e$^-$) coexist in the gas from which most of the [C II] line emission stems, although H is the most abundant one, followed by H$_2$. *Bottom row, right:* Mass-weighted excitation coefficients for every species (Eq. (A9RADMC–3Dequation.A.9)) as a function of the temperature. For $T < 40$ K collisions with H$_2$ dominate, whereas for $T > 40$ K collisions with H contribute most to the [C II] line emission. figure.caption.10 and 10Total (solid line) and observable (dashed line) luminosity of the optically thin [C II] line emission originating from
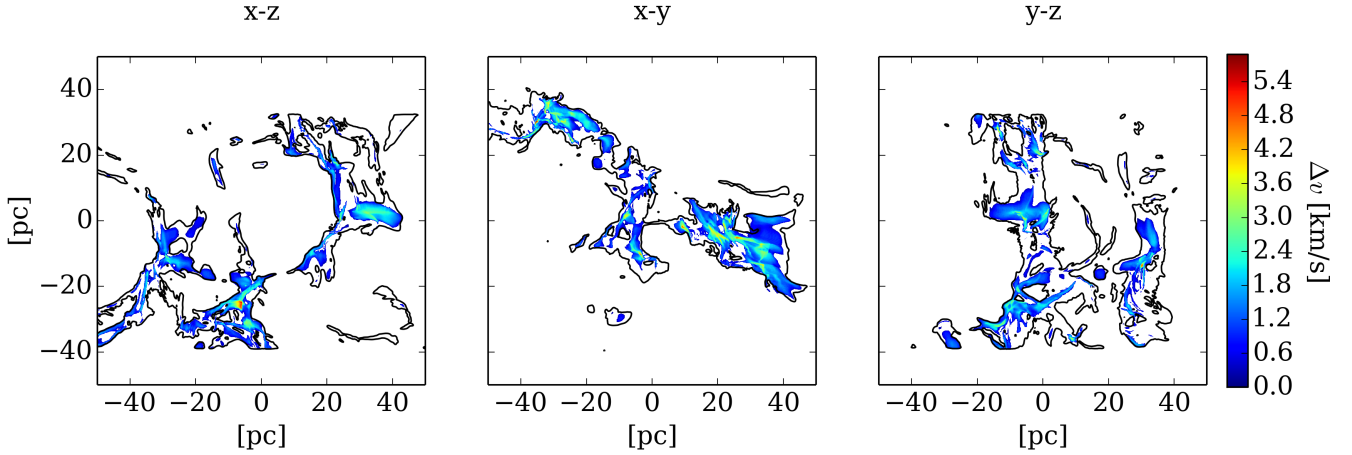
Figure 5. Maps of the different projections for L10, showing where the [C II] line emission becomes optically thick ($\tau_{[CII]} \geqslant 1$) in at least one velocity channel. The colour-coding shows the width in velocity space over which the emission is optically thick. The black contours mark the observable area for which $I_{[CII]} \geqslant 0.5$ K km s^{-1}. About 39%, 34% and 47% of the observable area is optically thick for the projections $x - z$, $x - y$ and $y - z$, respectively.

the gas distinguished by its number density with $n > n_i$ (first row), its fractional abundance of H$_2$ (x_{H_2}; middle row), and its visual extinction (A$_V$; bottom row). In the left column, we show the cumulative distribution and in the middle column its derivative. Note that dense gas appears on the left-hand side of the x-axes. The right column depicts the mass-weighted species distributions (see Section 4.1Temperature dependencesubsection.4.1). The red shaded area and the grey, dashed vertical line mark the median and the interquartile range for the emission of the total map. figure.caption.13. The results are presented for the whole map and the observable region (where $I_{[CII]} \geqslant 0.5$ K km s^{-1}). table.caption.8 and 3Same as Table 2Summary of the parameter space of the [C II] emitting gas, analysed for the optically thin [C II] line emission. We give the values of T_{kin}, n, the fractional abundance of H$_2$ (x_{H_2}), and the visual extinction (A$_V$) at which 25%, 50% (median) and 75% of the total luminosity are reached. The corresponding plots are shown in Figs. 7*Upper row, left:* Plot of the optically thin [C II] line luminosity originating from gas with $T \leqslant T_i$ for the total map (solid line) and the assumed observable region (dashed line). The cyan line represents the expectation if all of the C$^+$ ions were in LTE. The red shaded area and the grey, dashed vertical line mark the interquartile range and the median of the distribution derived for the total map. *Upper row, right:* The slope of the cumulative luminosity distribution, derived by taking the derivative of the luminosity with respect to the temperature. Most of the emission comes from $40 \lesssim T \lesssim 60$ K. *Bottom row, left:* Mass-weighted temperature distributions of the included species. $M_i/M_{species, tot}$ indicates the mass fraction of every species with respect to the total hydrogen, carbon or electron mass, respectively. All collisional partners (H$_2$, H, e$^-$) coexist in the gas from which most of the [C II] line emission stems, although H is the most abundant one, followed by H$_2$. *Bottom row, right:* Mass-weighted excitation coefficients for every species (Eq. (A9RADMC–3Dequation.A.9)) as a function of the temperature. For $T < 40$ K collisions with H$_2$ dominate, whereas for $T > 40$ K collisions with H contribute most

to the [C II] line emission. figure.caption.10 and 10Total (solid line) and observable (dashed line) luminosity of the optically thin [C II] line emission originating from the gas distinguished by its number density with $n > n_i$ (first row), its fractional abundance of H$_2$ (x_{H_2}; middle row), and its visual extinction (A$_V$; bottom row). In the left column, we show the cumulative distribution and in the middle column its derivative. Note that dense gas appears on the left-hand side of the x-axes. The right column depicts the mass-weighted species distributions (see Section 4.1Temperature dependencesubsection.4.1). The red shaded area and the grey, dashed vertical line mark the median and the interquartile range for the emission of the total map. figure.caption.13. The results are presented for the whole map and the observable region (where $I_{[CII]} \geqslant 0.5$ K km s^{-1}). table.caption.8, but analysed for the opacity affected [C II] line emission. The values of the parameters are similar to the optically thin [C II] line emission. However, note that the results of the opacity affected [C II] line emission overestimate the total emission. This table is included here for the sake of completeness. table.caption.9.

4.1 Temperature dependence

From the simulation we know the temperature in every cell and can select cells up to a certain value T_i. We calculate the synthetic emission maps for each regime i, for which we include gas with $T_{kin} \leqslant T_i$. We increase T_i from 10 K to 10^5 K. In addition, we perform the inverse analysis by selecting all cells with $T_{kin} > T_i$. In the ideal case of an optically thin tracer, the emission for $T \leqslant T_i$ and $T > T_i$ adds up to the total emission in the map. In Fig. 6Cumulative distributions of the [C II] luminosity arising from regions with $T \leqslant T_i$ and $T > T_i$ for the opacity affected (dashed red line) and the optically thin (solid black line) case. Summing both lines should give the total luminosity. This is fulfilled for the optically thin [C II] line emission (solid blue line), but for the optically thick case the total adds up to more than 100% (dashed
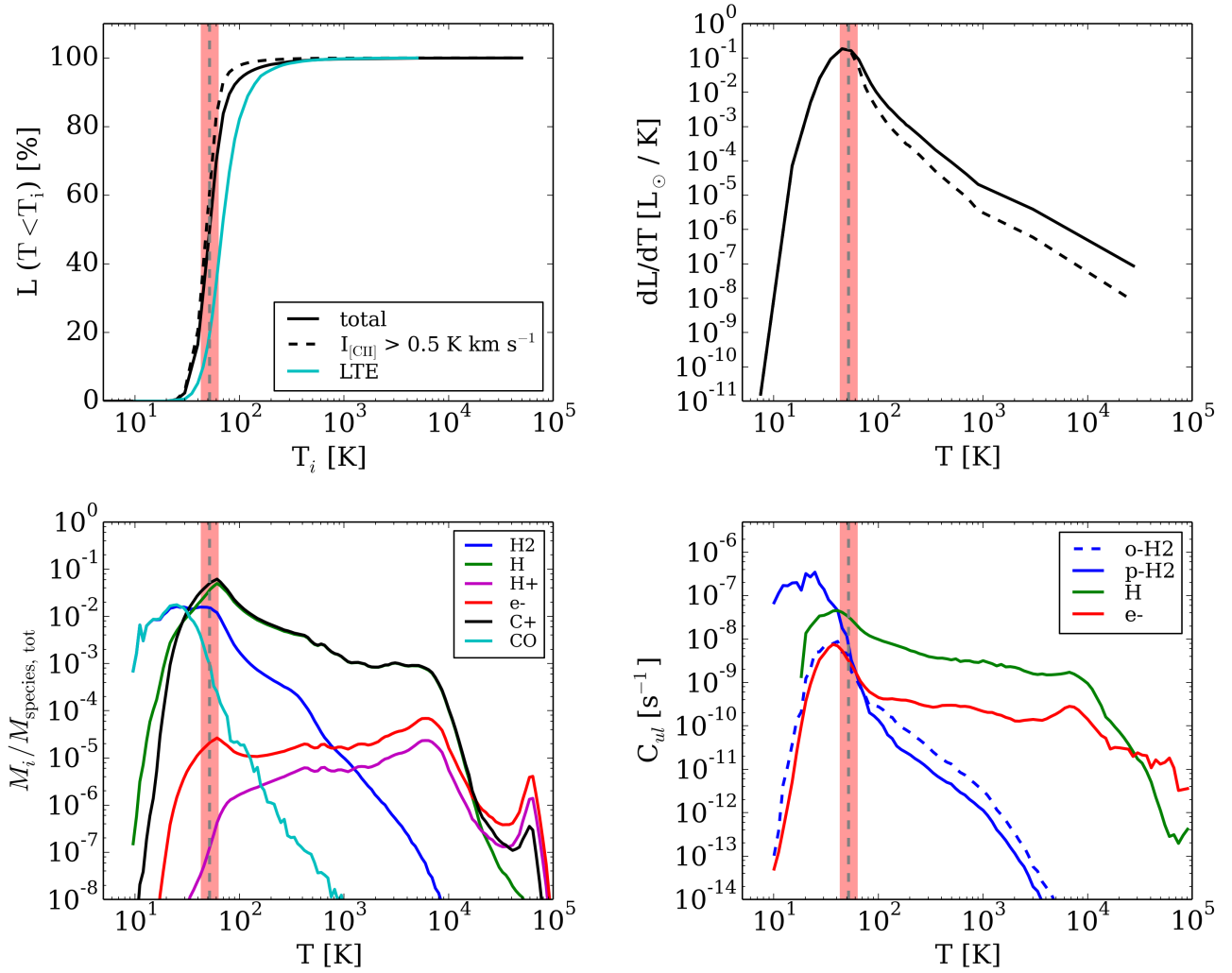
Figure 7. *Upper row, left:* Plot of the optically thin [C II] line luminosity originating from gas with $T \leqslant T_i$ for the total map (solid line) and the assumed observable region (dashed line). The cyan line represents the expectation if all of the C^+ ions were in LTE. The red shaded area and the grey, dashed vertical line mark the interquartile range and the median of the distribution derived for the total map. *Upper row, right:* The slope of the cumulative luminosity distribution, derived by taking the derivative of the luminosity with respect to the temperature. Most of the emission comes from $40 \lesssim T \lesssim 60$ K. *Bottom row, left:* Mass-weighted temperature distributions of the included species. $M_i/M_{\text{species, tot}}$ indicates the mass fraction of every species with respect to the total hydrogen, carbon or electron mass, respectively. All collisional partners (H_2, H, e^-) coexist in the gas from which most of the [C II] line emission stems, although H is the most abundant one, followed by H_2. *Bottom row, right:* Mass-weighted excitation coefficients for every species (Eq. (A9RADMC–3Dequation.A.9)) as a function of the temperature. For $T < 40$ K collisions with H_2 dominate, whereas for $T > 40$ K collisions with H contribute most to the [C II] line emission.

magenta line). figure.caption.7 we show how much of the opacity affected [C II] line emission (red, dashed lines) and the optically thin [C II] line emission (black, solid lines) originates from gas with $T \leqslant T_i$ (growing from left to right) and $T > T_i$ (dropping off from left to right). If we add up the emission for $T \leqslant T_i$ and $T > T_i$ for the opacity affected [C II] (dashed, magenta line), we see that the total emission is overestimated by about 10% for values of T_i between 30 K and 100 K. This occurs because when we include only part of the full range of temperatures, we change the C^+ optical depth and hence the fraction of the emission able to reach the observer. However, for

the optically thin [C II] emission the contributions from $T \leqslant T_i$ and $T > T_i$ recover 100% of the total emission (blue, solid line) for all temperature thresholds. Otherwise, the local emission properties are basically the same for the opacity affected and optically thin [C II] line emission.

In Fig. 7 *Upper row, left:* Plot of the optically thin [C II] line luminosity originating from gas with $T \leqslant T_i$ for the total map (solid line) and the assumed observable region (dashed line). The cyan line represents the expectation if all of the C^+ ions were in LTE. The red shaded area and the grey, dashed vertical line mark the interquartile
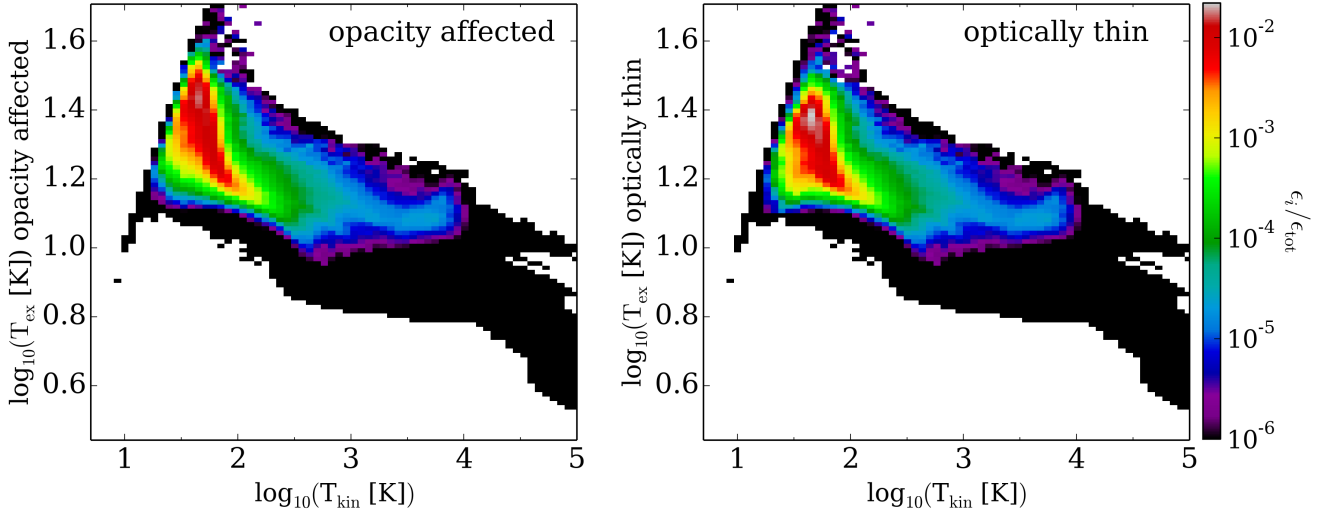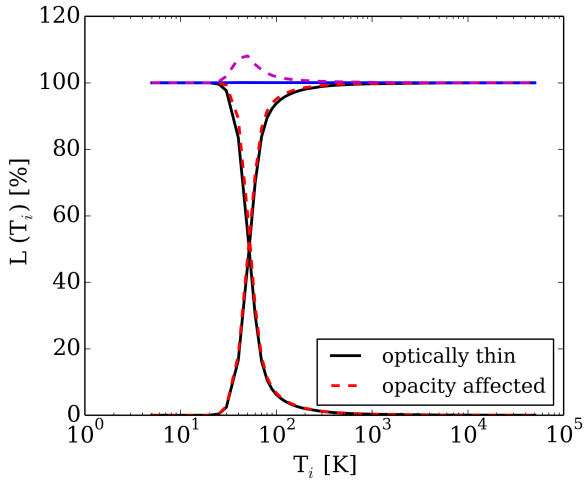
Figure 8. Emissivity-weighted 2D-PDFs as a function of the kinetic temperature $T_{\rm kin}$ and the excitation temperature $T_{\rm ex}$ for the opacity affected [C II] (left) and the optically thin [C II] line emission (right). $T_{\rm ex}$ is calculated internally by RADMC–3D and determines the level populations of C^+. The colour-coding shows the emissivity from the gas. The identity $T_{\rm kin} = T_{\rm ex}$ can be recognised as the straight upper left boundary of the populated area.

Figure 6. Cumulative distributions of the [C II] luminosity arising from regions with $T \leqslant T_i$ and $T > T_i$ for the opacity affected (dashed red line) and the optically thin (solid black line) case. Summing both lines should give the total luminosity. This is fulfilled for the optically thin [C II] line emission (solid blue line), but for the optically thick case the total adds up to more than 100% (dashed magenta line).

stems, although H is the most abundant one, followed by H_2. *Bottom row, right:* Mass-weighted excitation coefficients for every species (Eq. (A9RADMC–3Dequation.A.9)) as a function of the temperature. For $T < 40$ K collisions with H_2 dominate, whereas for $T > 40$ K collisions with H contribute most to the [C II] line emission. figure.caption.10 we show the cumulative distribution of the optically thin [C II] luminosity as function of the temperature of the emitting gas (in the upper left panel), and how much of the emission stems from the different temperature regimes (in the upper right panel). The latter is calculated as the first derivative of the cumulative plot. The solid lines present the analysis for the whole emission map, the dashed lines only for the observable region (where $I_{[CII]} \geqslant 0.5$ K km s^{-1}). Below 20 K the [C II] line emission is negligible. For both the analysis with all pixels and only the observable pixels of the synthetic emission maps, almost all of the [C II] line emission originates from 20 K $\leqslant T \leqslant$ 100 K. In Table 2Summary of the parameter space of the [C II] emitting gas, analysed for the optically thin [C II] line emission. We give the values of $T_{\rm kin}$, n, the fractional abundance of H_2 (x_{H_2}), and the visual extinction (A_V) at which 25%, 50% (median) and 75% of the total luminosity are reached. The corresponding plots are shown in Figs. 7*Upper row, left:* Plot of the optically thin [C II] line luminosity originating from gas with $T \leqslant T_i$ for the total map (solid line) and the assumed observable region (dashed line). The cyan line represents the expectation if all of the C^+ ions were in LTE. The red shaded area and the grey, dashed vertical line mark the interquartile range and the median of the distribution derived for the total map. *Upper row, right:* The slope of the cumulative luminosity distribution, derived by taking the derivative of the luminosity with respect to the temperature. Most of the emission comes from $40 \lesssim T \lesssim 60$ K. *Bottom row, left:* Mass-weighted temperature distributions of the included species. $M_i/M_{\rm species,\ tot}$

range and the median of the distribution derived for the total map. *Upper row, right:* The slope of the cumulative luminosity distribution, derived by taking the derivative of the luminosity with respect to the temperature. Most of the emission comes from $40 \lesssim T \lesssim 60$ K. *Bottom row, left:* Mass-weighted temperature distributions of the included species. $M_i/M_{\rm species,\ tot}$ indicates the mass fraction of every species with respect to the total hydrogen, carbon or electron mass, respectively. All collisional partners (H_2, H, e$^-$) coexist in the gas from which most of the [C II] line emission

Table 2. Summary of the parameter space of the [C II] emitting gas, analysed for the optically thin [C II] line emission. We give the values of T_{kin}, n, the fractional abundance of $\mathrm{H_2}$ ($x_{\mathrm{H_2}}$), and the visual extinction ($\mathrm{A_V}$) at which 25%, 50% (median) and 75% of the total luminosity are reached. The corresponding plots are shown in Figs. 7 *Upper row, left:* Plot of the optically thin [C II] line luminosity originating from gas with $T \leqslant T_i$ for the total map (solid line) and the assumed observable region (dashed line). The cyan line represents the expectation if all of the $\mathrm{C^+}$ ions were in LTE. The red shaded area and the grey, dashed vertical line mark the interquartile range and the median of the distribution derived for the total map. *Upper row, right:* The slope of the cumulative luminosity distribution, derived by taking the derivative of the luminosity with respect to the temperature. Most of the emission comes from $40 \lesssim T \lesssim 60$ K. *Bottom row, left:* Mass-weighted temperature distributions of the included species. $M_i/M_{\mathrm{species,\,tot}}$ indicates the mass fraction of every species with respect to the total hydrogen, carbon or electron mass, respectively. All collisional partners ($\mathrm{H_2}$, H, $\mathrm{e^-}$) coexist in the gas from which most of the [C II] line emission stems, although H is the most abundant one, followed by $\mathrm{H_2}$. *Bottom row, right:* Mass-weighted excitation coefficients for every species (Eq. (A9RADMC–3Dequation.A.9)) as a function of the temperature. For $T < 40$ K collisions with $\mathrm{H_2}$ dominate, whereas for $T > 40$ K collisions with H contribute most to the [C II] line emission. figure.caption.10 and 10Total (solid line) and observable (dashed line) luminosity of the optically thin [C II] line emission originating from the gas distinguished by its number density with $n > n_i$ (first row), its fractional abundance of $\mathrm{H_2}$ ($x_{\mathrm{H_2}}$; middle row), and its visual extinction ($\mathrm{A_V}$; bottom row). In the left column, we show the cumulative distribution and in the middle column its derivative. Note that dense gas appears on the left-hand side of the x-axes. The right column depicts the mass-weighted species distributions (see Section 4.1Temperature dependencesubsection.4.1). The red shaded area and the grey, dashed vertical line mark the median and the interquartile range for the emission of the total map. figure.caption.13. The results are presented for the whole map and the observable region (where $I_{\mathrm{[CII]}} \geqslant 0.5$ K km s^{-1}).

[C II], opt. thin	taken pixels	L/L_{tot}		
		$\geqslant 25\%$	$\geqslant 50\%$	$\geqslant 75\%$
T_{kin}	total	43 K	52 K	64 K
	observable	41 K	48 K	57 K
n	total	53 cm^{-3}	166 cm^{-3}	438 cm^{-3}
	observable	103 cm^{-3}	247 cm^{-3}	524 cm^{-3}
$x_{\mathrm{H_2}}$	total	0.08	0.14	0.22
	observable	0.11	0.17	0.23
$\mathrm{A_V}$	total	0.50	0.68	0.91
	observable	0.60	0.76	0.96

indicates the mass fraction of every species with respect to the total hydrogen, carbon or electron mass, respectively. All collisional partners ($\mathrm{H_2}$, H, $\mathrm{e^-}$) coexist in the gas from which most of the [C II] line emission stems, although H is the most abundant one, followed by $\mathrm{H_2}$. *Bottom row, right:* Mass-weighted excitation coefficients for every species (Eq. (A9RADMC–3Dequation.A.9)) as a function of the temperature. For $T < 40$ K collisions with $\mathrm{H_2}$ dominate, whereas for $T > 40$ K collisions with H contribute most to the [C II] line emission. figure.caption.10 and 10Total

(solid line) and observable (dashed line) luminosity of the optically thin [C II] line emission originating from the gas distinguished by its number density with $n > n_i$ (first row), its fractional abundance of $\mathrm{H_2}$ ($x_{\mathrm{H_2}}$; middle row), and its visual extinction ($\mathrm{A_V}$; bottom row). In the left column, we show the cumulative distribution and in the middle column its derivative. Note that dense gas appears on the left-hand side of the x-axes. The right column depicts the mass-weighted species distributions (see Section 4.1Temperature dependencesubsection.4.1). The red shaded area and the grey, dashed vertical line mark the median and the interquartile range for the emission of the total map. figure.caption.13. The results are presented for the whole map and the observable region (where $I_{\mathrm{[CII]}} \geqslant 0.5$ K km s^{-1}). table.caption.8 we list the temperatures at which 25%, 50% (median) and 75% of the total luminosity are reached. In Fig. 7 *Upper row, left:* Plot of the optically thin [C II] line luminosity originating from gas with $T \leqslant T_i$ for the total map (solid line) and the assumed observable region (dashed line). The cyan line represents the expectation if all of the $\mathrm{C^+}$ ions were in LTE. The red shaded area and the grey, dashed vertical line mark the interquartile range and the median of the distribution derived for the total map. *Upper row, right:* The slope of the cumulative luminosity distribution, derived by taking the derivative of the luminosity with respect to the temperature. Most of the emission comes from $40 \lesssim T \lesssim 60$ K. *Bottom row, left:* Mass-weighted temperature distributions of the included species. $M_i/M_{\mathrm{species,\,tot}}$ indicates the mass fraction of every species with respect to the total hydrogen, carbon or electron mass, respectively. All collisional partners ($\mathrm{H_2}$, H, $\mathrm{e^-}$) coexist in the gas from which most of the [C II] line emission stems, although H is the most abundant one, followed by $\mathrm{H_2}$. *Bottom row, right:* Mass-weighted excitation coefficients for every species (Eq. (A9RADMC–3Dequation.A.9)) as a function of the temperature. For $T < 40$ K collisions with $\mathrm{H_2}$ dominate, whereas for $T > 40$ K collisions with H contribute most to the [C II] line emission. figure.caption.10 the red shaded area marks the interquartile range, i.e. the difference between the 25th and the 75th percentile, for the cumulative plot when taking all pixels into account. The results for the optically thin and opacity affected [C II] line are similar (see Table 3Same as Table 2Summary of the parameter space of the [C II] emitting gas, analysed for the optically thin [C II] line emission. We give the values of T_{kin}, n, the fractional abundance of $\mathrm{H_2}$ ($x_{\mathrm{H_2}}$), and the visual extinction ($\mathrm{A_V}$) at which 25%, 50% (median) and 75% of the total luminosity are reached. The corresponding plots are shown in Figs. 7 *Upper row, left:* Plot of the optically thin [C II] line luminosity originating from gas with $T \leqslant T_i$ for the total map (solid line) and the assumed observable region (dashed line). The cyan line represents the expectation if all of the $\mathrm{C^+}$ ions were in LTE. The red shaded area and the grey, dashed vertical line mark the interquartile range and the median of the distribution derived for the total map. *Upper row, right:* The slope of the cumulative luminosity distribution, derived by taking the derivative of the luminosity with respect to the temperature. Most of the emission comes from $40 \lesssim T \lesssim 60$ K. *Bottom row, left:* Mass-weighted temperature distributions of the included species. $M_i/M_{\mathrm{species,\,tot}}$ indicates the mass fraction of every

species with respect to the total hydrogen, carbon or electron mass, respectively. All collisional partners (H$_2$, H, e$^-$) coexist in the gas from which most of the [C II] line emission stems, although H is the most abundant one, followed by H$_2$. *Bottom row, right:* Mass-weighted excitation coefficients for every species (Eq. (A9RADMC–3Dequation.A.9)) as a function of the temperature. For $T < 40$ K collisions with H$_2$ dominate, whereas for $T > 40$ K collisions with H contribute most to the [C II] line emission. figure.caption.10 and 10Total (solid line) and observable (dashed line) luminosity of the optically thin [C II] line emission originating from the gas distinguished by its number density with $n > n_i$ (first row), its fractional abundance of H$_2$ (x_{H_2}; middle row), and its visual extinction (A$_V$; bottom row). In the left column, we show the cumulative distribution and in the middle column its derivative. Note that dense gas appears on the left-hand side of the x-axes. The right column depicts the mass-weighted species distributions (see Section 4.1Temperature dependencesubsection.4.1). The red shaded area and the grey, dashed vertical line mark the median and the interquartile range for the emission of the total map. figure.caption.13. The results are presented for the whole map and the observable region (where $I_{[\mathrm{CII}]} \geqslant 0.5$ K km s^{-1}). table.caption.8, but analysed for the opacity affected [C II] line emission. The values of the parameters are similar to the optically thin [C II] line emission. However, note that the results of the opacity affected [C II] line emission overestimate the total emission. This table is included here for the sake of completeness. table.caption.9), with a median ($L/L_{\mathrm{tot}} \geqslant 50\%$) around 50 K.

The cyan line shows the LTE prediction for the [C II] line emission, that is proportional to

$$L_{\mathrm{LTE}} \propto h\nu A_{ul} n_{\mathrm{C}^+} \frac{g_u}{g_l} \frac{1}{Z(T)} e^{-\frac{h\nu_{ul}}{k_B T}}, \qquad (5)$$

with the Planck constant, h, the Einstein coefficient, A_{ul}, the number density of C$^+$, n_{C^+}, the statistical weights, $g_u = 4$ and $g_l = 2$, the Boltzmann constant, k_B, the temperature T, and the partition function $Z(T)$ defined as

$$Z(T) = 1 + \frac{g_u}{g_l} e^{-\frac{h\nu_{ul}}{k_B T}}. \qquad (6)$$

LTE would be obtained at high densities. The difference between the LTE curve and the curves from the simulations indicates that most of the [C II] emission is subthermal, in agreement with the fact that most of the gas in the simulation is below the critical density. As discussed already in Goldsmith et al. (2012), a large part of the [C II] emission in the Galaxy stems from thin, subthermally excited gas. Warmer gas is typically less dense than cooler gas, and hence has level populations further from their LTE values. As a result, we obtain a larger fraction of the total [C II] emission from cooler gas and a smaller fraction from warmer gas than we would expect if the emission were thermal throughout.

We compare the available collisional partners as a function of temperature in the lower left panel of Fig. 7*Upper row, left:* Plot of the optically thin [C II] line luminosity originating from gas with $T \leqslant T_i$ for the total map (solid

line) and the assumed observable region (dashed line). The cyan line represents the expectation if all of the C$^+$ ions were in LTE. The red shaded area and the grey, dashed vertical line mark the interquartile range and the median of the distribution derived for the total map. *Upper row, right:* The slope of the cumulative luminosity distribution, derived by taking the derivative of the luminosity with respect to the temperature. Most of the emission comes from $40 \lesssim T \lesssim 60$ K. *Bottom row, left:* Mass-weighted temperature distributions of the included species. $M_i/M_{\mathrm{species, \, tot}}$ indicates the mass fraction of every species with respect to the total hydrogen, carbon or electron mass, respectively. All collisional partners (H$_2$, H, e$^-$) coexist in the gas from which most of the [C II] line emission stems, although H is the most abundant one, followed by H$_2$. *Bottom row, right:* Mass-weighted excitati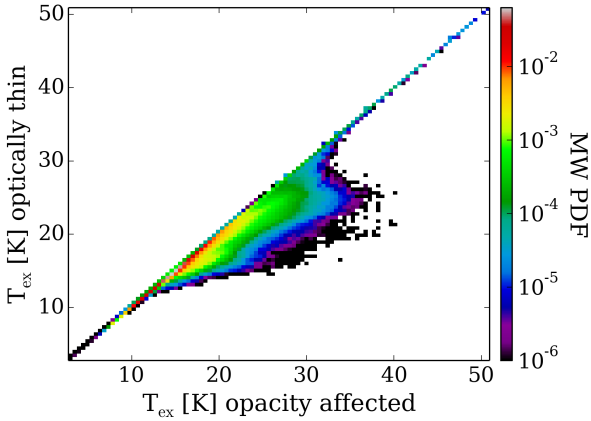on coefficients for every species (Eq. (A9RADMC–3Dequation.A.9)) as a function of the temperature. For $T < 40$ K collisions with H$_2$ dominate, whereas for $T > 40$ K collisions with H contribute most to the [C II] line emission. figure.caption.10. The temperature bin size is $\Delta \log_{10}(T \; [\mathrm{K}]) = 0.32$. We show the mass-weighted distributions of the included chemical species. The hydrogen species (H, H$_2$, and H$^+$) are normalized to the total hydrogen mass of $M_{\mathrm{H, \, tot}} = M_{\mathrm{H}_2} + M_{\mathrm{H}} + M_{\mathrm{H}^+}$, and the carbon species (CO and C$^+$) are normalized to the total mass of carbon-bearing species of $M_{\mathrm{C, \, tot}} = M_{\mathrm{CO}} + M_{\mathrm{C}^+}$. The free electrons are weighted by the mass of electrons that could potentially be free electrons: in our network a carbon species can give one electron, every hydrogen atom can give one, and thus we weight the mass of free electrons by $M_{\mathrm{e, \, tot}} = m_e \cdot (2n_{\mathrm{H}_2} + n_{\mathrm{H}} + n_{\mathrm{H}^+} + n_{\mathrm{CO}} + n_{\mathrm{C}^+}) \cdot d\mathrm{V}$. In this way, one can directly read off the relative abundance of the considered collisional partners, i.e. H, H$_2$ and free electrons, for each temperature. Within the interquartile range from which 50% of the [C II] line emission originates, atomic hydrogen is the most abundant collisional partner, followed by H$_2$. The amount of free electrons is negligible. Also, over the entire temperature regime the distribution of the C$^+$ ions is aligned with the distribution of atomic hydrogen. Less than 1% of the C$^+$ mass is at $T \leqslant 20$ K. About 73% of the total C$^+$ mass is present in gas at temperatures between 20 K and 100 K.

In the bottom right panel of Fig. 7*Upper row, left:* Plot of the optically thin [C II] line luminosity originating from gas with $T \leqslant T_i$ for the total map (solid line) and the assumed observable region (dashed line). The cyan line represents the expectation if all of the C$^+$ ions were in LTE. The red shaded area and the grey, dashed vertical line mark the interquartile range and the median of the distribution derived for the total map. *Upper row, right:* The slope of the cumulative luminosity distribution, derived by taking the derivative of the luminosity with respect to the temperature. Most of the emission comes from $40 \lesssim T \lesssim 60$ K. *Bottom row, left:* Mass-weighted temperature distributions of the included species. $M_i/M_{\mathrm{species, \, tot}}$ indicates the mass fraction of every species with respect to the total hydrogen, carbon or electron mass, respectively. All collisional partners (H$_2$, H, e$^-$) coexist in the gas from which most of the [C II] line emission stems, although H is the most abundant one, followed by H$_2$. *Bottom row, right:* Mass-weighted excitation coefficients for every species

Figure 9. Mass weighted 2D-PDF of the excitation temperatures, $T_{\rm ex}$, of the opacity affected and the optically thin [C II] line emission.

(Eq. (A9RADMC–3Dequation.A.9)) as a function of the temperature. For $T < 40$ K collisions with H_2 dominate, whereas for $T > 40$ K collisions with H contribute most to the [C II] line emission. figure.caption.10 we study the mass-weighted excitation rates for the chemical species as a function of kinetic temperature. Below 40 K, collisions with para-H_2 dominate. For temperatures $T \geqslant 40$ K atomic hydrogen becomes the dominant collisional partner, coinciding with the temperature range from which 50% of the emission originates, as marked with the red-shaded area. Although H remains the dominant chemical component for higher temperatures ($T > 100$ K), the further contribution to the total [C II] line emission is low because the density of the gas is small at high temperatures (see upper panels).

RADMC–3D calculates internally the level populations x_u and x_l for the upper (u) and lower level (l), respectively, of C^+. We use this output to recalculate the excitation temperature, $T_{\rm ex}$, with

$$T_{\rm ex} = \frac{-h\nu_{ul}}{k} \cdot \left[\ln \left(\frac{x_u}{x_l} \frac{g_l}{g_u} \right) \right]^{-1}. \qquad (7)$$

Figure 8Emissivity-weighted 2D-PDFs as a function of the kinetic temperature $T_{\rm kin}$ and the excitation temperature $T_{\rm ex}$ for the opacity affected [C II] (left) and the optically thin [C II] line emission (right). $T_{\rm ex}$ is calculated internally by RADMC–3D and determines the level populations of C^+. The colour-coding shows the emissivity from the gas. The identity $T_{\rm kin} = T_{\rm ex}$ can be recognised as the straight upper left boundary of the populated area. figure.caption.11 shows the 2D-PDF of the gas emissivities as a function of $T_{\rm ex}$ and $T_{\rm kin}$ for the opacity affected (left) and the optically thin (right) [C II] line emission (bin sizes are $\Delta \log_{10}(T_{\rm kin}$ [K]$) = 0.07$ and $\Delta \log_{10}(T_{\rm ex}$ [K]$) = 0.01$). The emissivities were calculated in analogy to Eq. (5Temperature dependenceequation.4.5), where we inserted $T_{\rm ex}$ as the temperature. In the low temperature regime ($T \leqslant 30$ K), LTE conditions are fulfilled ($T_{\rm kin} = T_{\rm ex}$), as the low temperature gas is correlated with high densities in this temperature regime. At $T_{\rm kin} \approx 50$ K, where a large fraction of the emission originates, the excitation temperature becomes significantly smaller than $T_{\rm kin}$ and drops to values around $T_{\rm ex} \approx 20$ K.

Therefore the emission is subthermal. The distributions for the opacity affected and optically thin [C II] line emission appear similar. However, around $T_{\rm kin} \sim 50$ K the excitation temperature tends to higher values for the opacity affected [C II] line emission compared to the optically thin case. This is caused by the optical depth effects and the resulting radiative excitation. We illustrate the difference between $T_{\rm ex}$ for the opacity affected and the optically thin [C II] line emission in Fig. 9Mass weighted 2D-PDF of the excitation temperatures, $T_{\rm ex}$, of the opacity affected and the optically thin [C II] line emission.figure.caption.12 with a 2D-PDF (bin size $\Delta T_{\rm ex} = 0.5$ K). $T_{\rm ex}$ deviates most in the optically thin range of 10 K $\lesssim T_{\rm ex} \lesssim 35$ K. Here the opacity affected $T_{\rm ex}$ is higher by up to 10 K.

4.2 Density dependence

We further constrain from which density range the [C II] line emission originates. For this we carry out an analysis in which we only select cells above a limiting number density n_i. The left panel of Fig. 10Total (solid line) and observable (dashed line) luminosity of the optically thin [C II] line emission originating from the gas distinguished by its number density with $n > n_i$ (first row), its fractional abundance of H_2 (x_{H_2}; middle row), and its visual extinction (A_V; bottom row). In the left column, we show the cumulative distribution and in the middle column its derivative. Note that dense gas appears on the left-hand side of the x-axes. The right column depicts the mass-weighted species distributions (see Section 4.1Temperature dependencesubsection.4.1). The red shaded area and the grey, dashed vertical line mark the median and the interquartile range for the emission of the total map. figure.caption.13 (first row) shows the resulting cumulative plot, and the middle panel the corresponding derivative. We find the [C II] line emission to originate from gas with densities between 53 cm^{-3} and 438 cm^{-3} (corresponding to the 25$^{\rm th}$ and the 75$^{\rm th}$ percentile) with the median of the cumulative luminosity distribution at 166 cm^{-3} (see also Table 2Summary of the parameter space of the [C II] emitting gas, analysed for the optically thin [C II] line emission. We give the values of $T_{\rm kin}$, n, the fractional abundance of H_2 (x_{H_2}), and the visual extinction (A_V) at which 25%, 50% (median) and 75% of the total luminosity are reached. The corresponding plots are shown in Figs. 7*Upper row, left:* Plot of the optically thin [C II] line luminosity originating from gas with $T \leqslant T_i$ for the total map (solid line) and the assumed observable region (dashed line). The cyan line represents the expectation if all of the C^+ ions were in LTE. The red shaded area and the grey, dashed vertical line mark the interquartile range and the median of the distribution derived for the total map. *Upper row, right:* The slope of the cumulative luminosity distribution, derived by taking the derivative of the luminosity with respect to the temperature. Most of the emission comes from $40 \lesssim T \lesssim 60$ K. *Bottom row, left:* Mass-weighted temperature distributions of the included species. $M_i/M_{\rm species,\ tot}$ indicates the mass fraction of every species with respect to the total hydrogen, carbon or electron mass, respectively. All collisional partners (H_2, H, e$^-$) coexist in the gas from which most of the [C II] line emission stems, although H is
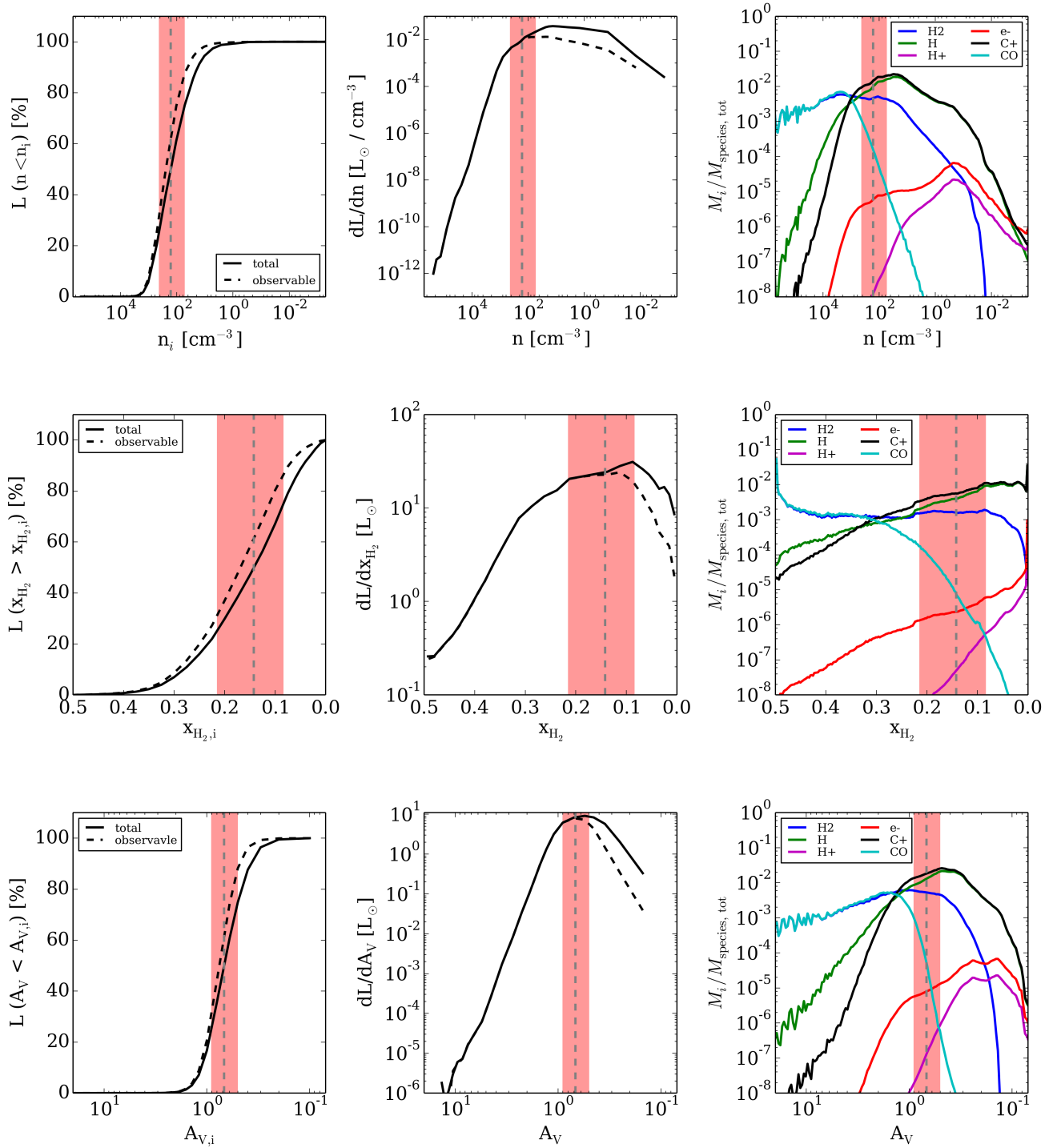
Figure 10. Total (solid line) and observable (dashed line) luminosity of the optically thin [C II] line emission originating from the gas distinguished by its number density with $n > n_i$ (first row), its fractional abundance of H_2 (x_{H_2}; middle row), and its visual extinction (A_V; bottom row). In the left column, we show the cumulative distribution and in the middle column its derivative. Note that dense gas appears on the left-hand side of the x-axes. The right column depicts the mass-weighted species distributions (see Section 4.1 Temperature dependence subsection.4.1). The red shaded area and the grey, dashed vertical line mark the median and the interquartile range for the emission of the total map.

the most abundant one, followed by H$_2$. *Bottom row, right:* Mass-weighted excitation coefficients for every species (Eq. (A9RADMC–3Dequation.A.9)) as a function of the temperature. For $T < 40$ K collisions with H$_2$ dominate, whereas for $T > 40$ K collisions with H contribute most to the [C II] line emission. figure.caption.10 and 10Total (solid line) and observable (dashed line) luminosity of the optically thin [C II] line emission originating from the gas distinguished by its number density with $n > n_i$ (first row), its fractional abundance of H$_2$ ($x_{\rm H_2}$; middle row), and its visual extinction (A$_{\rm V}$; bottom row). In the left column, we show the cumulative distribution and in the middle column its derivative. Note that dense gas appears on the left-hand side of the x-axes. The right column depicts the mass-weighted species distributions (see Section 4.1Temperature dependencesubsection.4.1). The red shaded area and the grey, dashed vertical line mark the median and the interquartile range for the emission of the total map. figure.caption.13. The results are presented for the whole map and the observable region (where $I_{\rm [CII]} \geqslant 0.5$ K km s^{-1}). table.caption.8). The same analysis carried out for the optically thick [C II] line emission results in slightly higher densities (see Table 3Same as Table 2Summary of the parameter space of the [C II] emitting gas, analysed for the optically thin [C II] line emission. We give the values of $T_{\rm kin}$, n, the fractional abundance of H$_2$ ($x_{\rm H_2}$), and the visual extinction (A$_{\rm V}$) at which 25%, 50% (median) and 75% of the total luminosity are reached. The corresponding plots are shown in Figs. 7*Upper row, left:* Plot of the optically thin [C II] line luminosity originating from gas with $T \leqslant T_i$ for the total map (solid line) and the assumed observable region (dashed line). The cyan line represents the expectation if all of the C$^+$ ions were in LTE. The red shaded area and the grey, dashed vertical line mark the interquartile range and the median of the distribution derived for the total map. *Upper row, right:* The slope of the cumulative luminosity distribution, derived by taking the derivative of the luminosity with respect to the temperature. Most of the emission comes from $40 \lesssim T \lesssim 60$ K. *Bottom row, left:* Mass-weighted temperature distributions of the included species. $M_i/M_{\rm species,\,tot}$ indicates the mass fraction of every species with respect to the total hydrogen, carbon or electron mass, respectively. All collisional partners (H$_2$, H, e$^-$) coexist in the gas from which most of the [C II] line emission stems, although H is the most abundant one, followed by H$_2$. *Bottom row, right:* Mass-weighted excitation coefficients for every species (Eq. (A9RADMC–3Dequation.A.9)) as a function of the temperature. For $T < 40$ K collisions with H$_2$ dominate, whereas for $T > 40$ K collisions with H contribute most to the [C II] line emission. figure.caption.10 and 10Total (solid line) and observable (dashed line) luminosity of the optically thin [C II] line emission originating from the gas distinguished by its number density with $n > n_i$ (first row), its fractional abundance of H$_2$ ($x_{\rm H_2}$; middle row), and its visual extinction (A$_{\rm V}$; bottom row). In the left column, we show the cumulative distribution and in the middle column its derivative. Note that dense gas appears on the left-hand side of the x-axes. The right column depicts the mass-weighted species distributions (see Section 4.1Temperature dependencesubsection.4.1). The red shaded area and the grey, dashed vertical line mark

the median and the interquartile range for the emission of the total map. figure.caption.13. The results are presented for the whole map and the observable region (where $I_{\rm [CII]} \geqslant 0.5$ K km s^{-1}). table.caption.8, but analysed for the opacity affected [C II] line emission. The values of the parameters are similar to the optically thin [C II] line emission. However, note that the results of the opacity affected [C II] line emission overestimate the total emission. This table is included here for the sake of completeness. table.caption.9). The higher densities are required since part of the emission is absorbed on the way to the observer. The right panel of Fig. 10Total (solid line) and observable (dashed line) luminosity of the optically thin [C II] line emission originating from the gas distinguished by its number density with $n > n_i$ (first row), its fractional abundance of H$_2$ ($x_{\rm H_2}$; middle row), and its visual extinction (A$_{\rm V}$; bottom row). In the left column, we show the cumulative distribution and in the middle column its derivative. Note that dense gas appears on the left-hand side of the x-axes. The right column depicts the mass-weighted species distributions (see Section 4.1Temperature dependencesubsection.4.1). The red shaded area and the grey, dashed vertical line mark the median and the interquartile range for the emission of the total map. figure.caption.13 (first row) shows the mass-weighted distributions of all species (with bin size $\Delta \log_{10}(n\,[\rm cm^{-3}]) = 0.05$). We find the distributions for C$^+$ and atomic hydrogen to be aligned for number densities below 1.2×10^3 cm^{-3}, the range from which most of the [C II] line emission originates.

4.3 Molecular gas dependence

As the [C II] line emission is used to estimate the fraction of CO-dark H$_2$ (Langer et al. 2014), we investigate how well the [C II] line emission traces the molecular gas phase in this cloud. We select cells with a particular fractional abundance of molecular hydrogen, $x_{\rm H_2}$, where $x_{\rm H_2} = 0.5$ if all hydrogen in a cell is is in molecular form. We use the optically thin [C II] line emission to present the results in the plots. As shown in the left panel of Fig. 10Total (solid line) and observable (dashed line) luminosity of the optically thin [C II] line emission originating from the gas distinguished by its number density with $n > n_i$ (first row), its fractional abundance of H$_2$ ($x_{\rm H_2}$; middle row), and its visual extinction (A$_{\rm V}$; bottom row). In the left column, we show the cumulative distribution and in the middle column its derivative. Note that dense gas appears on the left-hand side of the x-axes. The right column depicts the mass-weighted species distributions (see Section 4.1Temperature dependencesubsection.4.1). The red shaded area and the grey, dashed vertical line mark the median and the interquartile range for the emission of the total map. figure.caption.13 (second row), we find that the [C II] line emission starts to increase at $x_{\rm H_2,i} \sim 0.4$, where 80% of the hydrogen is in molecular form. Around 20% of the emission comes from gas regions with $x_{\rm H_2,i} \gtrsim 0.23$ ($\sim$47% of hydrogen in its molecular form). The median value of the cumulative plot (Table 2Summary of the parameter space of the [C II] emitting gas, analysed for the optically thin [C II] line emission. We give the values of $T_{\rm kin}$, n, the fractional abundance of H$_2$ ($x_{\rm H_2}$), and the visual extinction

(A_V) at which 25%, 50% (median) and 75% of the total luminosity are reached. The corresponding plots are shown in Figs. 7*Upper row, left:* Plot of the optically thin [C II] line luminosity originating from gas with $T \leqslant T_i$ for the total map (solid line) and the assumed observable region (dashed line). The cyan line represents the expectation if all of the C$^+$ ions were in LTE. The red shaded area and the grey, dashed vertical line mark the interquartile range and the median of the distribution derived for the total map. *Upper row, right:* The slope of the cumulative luminosity distribution, derived by taking the derivative of the luminosity with respect to the temperature. Most of the emission comes from $40 \lesssim T \lesssim 60$ K. *Bottom row, left:* Mass-weighted temperature distributions of the included species. $M_i/M_{\mathrm{species, tot}}$ indicates the mass fraction of every species with respect to the total hydrogen, carbon or electron mass, respectively. All collisional partners (H$_2$, H, e$^-$) coexist in the gas from which most of the [C II] line emission stems, although H is the most abundant one, followed by H$_2$. *Bottom row, right:* Mass-weighted excitation coefficients for every species (Eq. (A9RADMC–3Dequation.A.9)) as a function of the temperature. For $T < 40$ K collisions with H$_2$ dominate, whereas for $T > 40$ K collisions with H contribute most to the [C II] line emission. figure.caption.10 and 10Total (solid line) and observable (dashed line) luminosity of the optically thin [C II] line emission originating from the gas distinguished by its number density with $n > n_i$ (first row), its fractional abundance of H$_2$ (x_{H_2}; middle row), and its visual extinction (A_V; bottom row). In the left column, we show the cumulative distribution and in the middle column its derivative. Note that dense gas appears on the left-hand side of the x-axes. The right column depicts the mass-weighted species distributions (see Section 4.1Temperature dependencesubsection.4.1). The red shaded area and the grey, dashed vertical line mark the median and the interquartile range for the emission of the total map. figure.caption.13. The results are presented for the whole map and the observable region (where $I_{\mathrm{[CII]}} \geqslant 0.5$ K km s^{-1}). table.caption.8) is at $x_{\mathrm{H}_2} = 0.14$, meaning that 50% of the emission comes from gas in which less than 28% of hydrogen is in molecular form. Thus, we find most of the [C II] line emission to originate from the atomic gas phase. This is in agreement with the previous results. In the right panel we show the mass-weighted distributions of all species, this time as a function of x_{H_2} ($\Delta x_{\mathrm{H}_2} = 0.02$). C$^+$ is present for all x_{H_2}, but it only becomes more abundant than CO below $x_{\mathrm{H}_2} \lesssim 0.3$. This is only slightly deeper in the cloud than $x_{\mathrm{H}_2} = 0.25$, where the transition from H to H$_2$ dominated gas occurs.

4.4 Dependence on visual extinction

We further study from which gas phase the [C II] line emission originates in terms of the visual extinction, A_V, in the gas. In our version of the FLASH code, A_V is calculated for every cell in the computational domain using the TreeRay / OpticalDepth module (Wünsch et al. 2018). Thus, for any given cell, it is not integrated along a particular line of sight, but instead represents a local weighted average of the values along different lines of sight to that cell (see also Walch et al. 2015). We calculate the

synthetic emission maps including gas with $A_V < A_{V,i}$, and present the results in the bottom row of Fig. 10Total (solid line) and observable (dashed line) luminosity of the optically thin [C II] line emission originating from the gas distinguished by its number density with $n > n_i$ (first row), its fractional abundance of H$_2$ (x_{H_2}; middle row), and its visual extinction (A_V; bottom row). In the left column, we show the cumulative distribution and in the middle column its derivative. Note that dense gas appears on the left-hand side of the x-axes. The right column depicts the mass-weighted species distributions (see Section 4.1Temperature dependencesubsection.4.1). The red shaded area and the grey, dashed vertical line mark the median and the interquartile range for the emission of the total map. figure.caption.13. The left panel shows the resulting cumulative plot, its derivative and the mass-weighted distributions of all species ($\Delta \log_{10}(A_V) = 0.02$). All of the [C II] line emission comes from gas with $A_V < 2$, and 50% of the emission has $A_V < 0.68$. Gas in this regime consists predominantly of atomic hydrogen and ionized carbon, in line with the analyses done before. The median value as well as the 25th and the 75th percentile are listed in Table 2Summary of the parameter space of the [C II] emitting gas, analysed for the optically thin [C II] line emission. We give the values of T_{kin}, n, the fractional abundance of H$_2$ (x_{H_2}), and the visual extinction (A_V) at which 25%, 50% (median) and 75% of the total luminosity are reached. The corresponding plots are shown in Figs. 7*Upper row, left:* Plot of the optically thin [C II] line luminosity originating from gas with $T \leqslant T_i$ for the total map (solid line) and the assumed observable region (dashed line). The cyan line represents the expectation if all of the C$^+$ ions were in LTE. The red shaded area and the grey, dashed vertical line mark the interquartile range and the median of the distribution derived for the total map. *Upper row, right:* The slope of the cumulative luminosity distribution, derived by taking the derivative of the luminosity with respect to the temperature. Most of the emission comes from $40 \lesssim T \lesssim 60$ K. *Bottom row, left:* Mass-weighted temperature distributions of the included species. $M_i/M_{\mathrm{species, tot}}$ indicates the mass fraction of every species with respect to the total hydrogen, carbon or electron mass, respectively. All collisional partners (H$_2$, H, e$^-$) coexist in the gas from which most of the [C II] line emission stems, although H is the most abundant one, followed by H$_2$. *Bottom row, right:* Mass-weighted excitation coefficients for every species (Eq. (A9RADMC–3Dequation.A.9)) as a function of the temperature. For $T < 40$ K collisions with H$_2$ dominate, whereas for $T > 40$ K collisions with H contribute most to the [C II] line emission. figure.caption.10 and 10Total (solid line) and observable (dashed line) luminosity of the optically thin [C II] line emission originating from the gas distinguished by its number density with $n > n_i$ (first row), its fractional abundance of H$_2$ (x_{H_2}; middle row), and its visual extinction (A_V; bottom row). In the left column, we show the cumulative distribution and in the middle column its derivative. Note that dense gas appears on the left-hand side of the x-axes. The right column depicts the mass-weighted species distributions (see Section 4.1Temperature dependencesubsection.4.1). The red shaded area and the grey, dashed vertical line mark the median and the interquartile range for the

emission of the total map. figure.caption.13. The results are presented for the whole map and the observable region (where $I_{[\text{CII}]} \geqslant 0.5$ K km s^{-1}). table.caption.8 (and in Table 3Same as Table 2Summary of the parameter space of the [C II] emitting gas, analysed for the optically thin [C II] line emission. We give the values of T_{kin}, n, the fractional abundance of H$_2$ (x_{H_2}), and the visual extinction (A$_{\text{V}}$) at which 25%, 50% (median) and 75% of the total luminosity are reached. The corresponding plots are shown in Figs. 7*Upper row, left:* Plot of the optically thin [C II] line luminosity originating from gas with $T \leqslant T_i$ for the total map (solid line) and the assumed observable region (dashed line). The cyan line represents the expectation if all of the C$^+$ ions were in LTE. The red shaded area and the grey, dashed vertical line mark the interquartile range and the median of the distribution derived for the total map. *Upper row, right:* The slope of the cumulative luminosity distribution, derived by taking the derivative of the luminosity with respect to the temperature. Most of the emission comes from $40 \lesssim T \lesssim 60$ K. *Bottom row, left:* Mass-weighted temperature distributions of the included species. $M_i/M_{\text{species, tot}}$ indicates the mass fraction of every species with respect to the total hydrogen, carbon or electron mass, respectively. All collisional partners (H$_2$, H, e$^-$) coexist in the gas from which most of the [C II] line emission stems, although H is the most abundant one, followed by H$_2$. *Bottom row, right:* Mass-weighted excitation coefficients for every species (Eq. (A9RADMC–3Dequation.A.9)) as a function of the temperature. For $T < 40$ K collisions with H$_2$ dominate, whereas for $T > 40$ K collisions with H contribute most to the [C II] line emission. figure.caption.10 and 10Total (solid line) and observable (dashed line) luminosity of the optically thin [C II] line emission originating from the gas distinguished by its number density with $n > n_i$ (first row), its fractional abundance of H$_2$ (x_{H_2}; middle row), and its visual extinction (A$_{\text{V}}$; bottom row). In the left column, we show the cumulative distribution and in the middle column its derivative. Note that dense gas appears on the left-hand side of the x-axes. The right column depicts the mass-weighted species distributions (see Section 4.1Temperature dependencesubsection.4.1). The red shaded area and the grey, dashed vertical line mark the median and the interquartile range for the emission of the total map. figure.caption.13. The results are presented for the whole map and the observable region (where $I_{[\text{CII}]} \geqslant 0.5$ K km s^{-1}). table.caption.8, but analysed for the opacity affected [C II] line emission. The values of the parameters are similar to the optically thin [C II] line emission. However, note that the results of the opacity affected [C II] line emission overestimate the total emission. This table is included here for the sake of completeness. table.caption.9 for the optically thick case). As done for the other studies we likewise investigate how the result changes when we only take the assumed observable pixels (dashed lines). Since the faint emission stems from gas with low densities, the shielding in this gas is likewise small. Thus, when only taking the observable pixels, we miss the emission from the gas with low A$_{\text{V}}$ values, whereas the overall result remains.

5 CORRELATION WITH COLUMN DENSITIES

In extragalactic studies, [C II] line emission is sometimes used to constrain the mass of the observed system, with the aid of PDR modelling. For example, in studies of submillimetre galaxies (Swinbank et al. 2012) and starburst galaxies (Hailey-Dunsheath et al. 2010) the mass of the molecular and atomic gas, respectively, is calculated directly from the [C II] line emission. There are likewise studies correlating the [C II] line emission with column densities. Goicoechea et al. (2015) study Orion in [^{12}C II] and [^{13}C II] and calculate the column density of C$^+$ in the analysed region. In the Milky Way Langer et al. (2014) constrain the C$^+$ column density from the [C II] line emission, following the work by Goldsmith et al. (2012). Inspired by these studies, we analyse the correlation between the [C II] line emission and the column densities of the total and atomic hydrogen gas, as well as of C$^+$. We note that our molecular cloud is in its formation process before the onset of star formation and therefore no (radiative) feedback processes are considered. Here, we only have a constant ISRF of $G_0 = 1.7$, irradiating the cloud from all directions. Thus, classical PDRs forming around young, massive stars are not considered. However, our simulations are useful for examining [C II] line emission from gas which is not in a classical PDR.

In Fig. 11Correlation between the integrated [C II] line intensity (opacity affected) and the column densities of the total gas (left), H (middle) and C$^+$ (right). The top row shows the distribution including the data for the whole map. The red vertical lines mark the assumed observable limit of $I_{[\text{CII}]} \geqslant 0.5$ K km s^{-1}. The bottom row shows only the observable data with their overplotted linear fits. The colour-coding indicates the fraction of pixels with respect to the entire map (X_i/X_{tot}) and to the observable area ($X_i/X_{\text{tot, obs}}$). figure.caption.14 we show the correlation between the [C II] line emission (opacity affected) and the total (left), H (middle), and C$^+$ (right) column densities in the upper row in a 2D-PDF with bin sizes of $\Delta\log_{10}(I \,[\text{K km s}^{-1}]) = 0.07$, $\Delta\log_{10}(N_i \,[\text{cm}^{-2}]) = 0.06$ for the whole map (upper row) and $\Delta\log_{10}(I \,[\text{K km s}^{-1}]) = 0.02$, $\Delta\log_{10}(N_i \,[\text{cm}^{-2}]) = 0.04$ for the observable area (bottom row). The red dashed lines in the plots mark the assumed observable limit at $I_{[\text{CII}]} \geqslant 0.5$ K km s^{-1}. In a double-logarithmic plot the opacity affected [C II] line emission follows a power law as a function of all three column densities. Higher column densities do not necessarily result in a higher integrated [C II] line intensity, since the [C II] line emission is partially optically thick and C$^+$ is converted to CO. Therefore, the distributions steepen in the observable area. In the bottom row of Fig. 11Correlation between the integrated [C II] line intensity (opacity affected) and the column densities of the total gas (left), H (middle) and C$^+$ (right). The top row shows the distribution including the data for the whole map. The red vertical lines mark the assumed observable limit of $I_{[\text{CII}]} \geqslant 0.5$ K km s^{-1}. The bottom row shows only the observable data with their overplotted linear fits. The colour-coding indicates the fraction of pixels with respect to the entire map (X_i/X_{tot}) and to the observable area ($X_i/X_{\text{tot, obs}}$). figure.caption.14 we show the
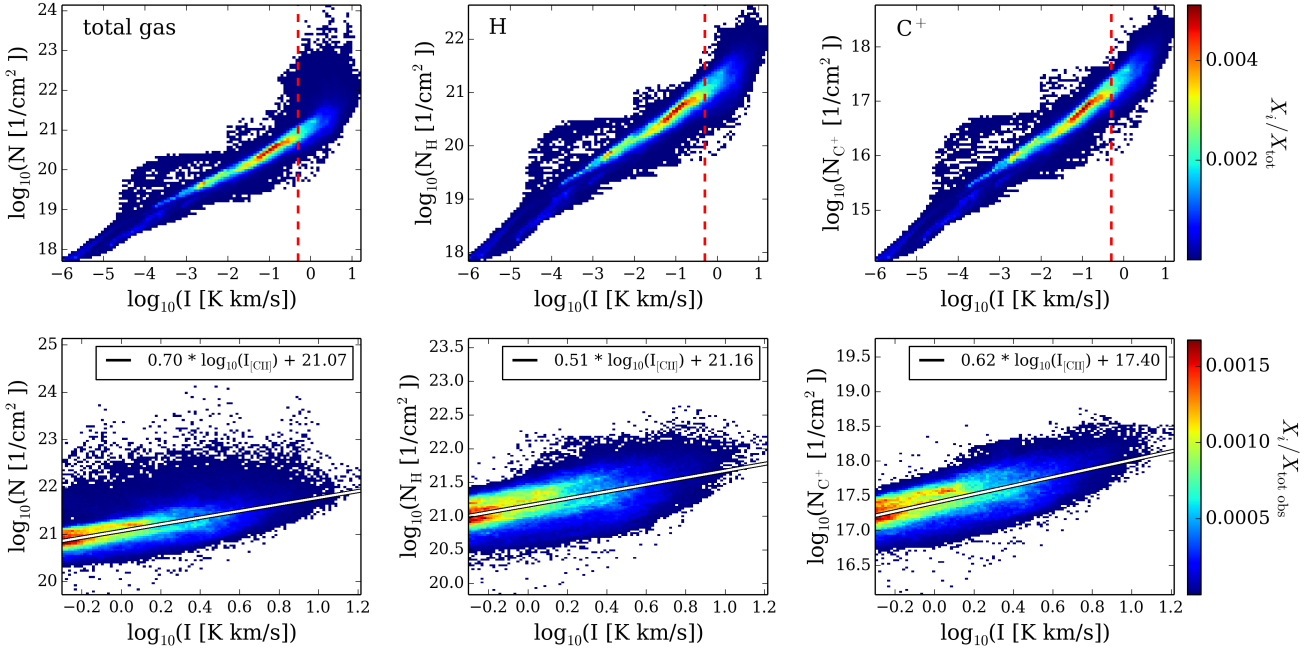
Figure 11. Correlation between the integrated [C II] line intensity (opacity affected) and the column densities of the total gas (left), H (middle) and C^+ (right). The top row shows the distribution including the data for the whole map. The red vertical lines mark the assumed observable limit of $I_{[CII]} \geqslant 0.5$ K km s^{-1}. The bottom row shows only the observable data with their overplotted linear fits. The colour-coding indicates the fraction of pixels with respect to the entire map (X_i/X_{tot}) and to the observable area ($X_i/X_{tot, obs}$).

2D-PDFs as a function of the opacity affected [C II] intensity and the column densities, restricted to the observable pixels. The colour-coding indicates the distribution of the fraction of the pixels. The distributions follow power laws that can be fitted[7] by

$$\log_{10}\left(\frac{N_{tot}}{cm^2}\right) = (0.702 \pm 0.002) \times \log_{10}\left(\frac{I_{[CII]}}{K\ km\ s^{-1}}\right) \\ + (21.0722 \pm 0.0005), \quad (8)$$

$$\log_{10}\left(\frac{N_H}{cm^2}\right) = (0.514 \pm 0.001) \times \log_{10}\left(\frac{I_{[CII]}}{K\ km\ s^{-1}}\right) \\ + (21.1595 \pm 0.0004), \quad (9)$$

$$\log_{10}\left(\frac{N_{C+}}{cm^2}\right) = (0.616 \pm 0.001) \times \log_{10}\left(\frac{I_{[CII]}}{K\ km\ s^{-1}}\right) \\ + (17.4008 \pm 0.0004). \quad (10)$$

In order to obtain a scale invariant quantity, we study the relation between the opacity affected [C II] integrated intensity (I) and the total column density of the molecular cloud (N_{tot}) with the Y_{CII} factor, defined as

$$Y_{CII} = \frac{N_{tot}}{I}. \quad (11)$$

A constant Y_{CII} in the whole map would indicate a linear behaviour between the intensity and the column density. We note that Y_{CII} is expected to strongly depend on the

local ISRF. The molecular cloud studied here is embedded in an ISRF with $G_0 = 1.7$. In clouds which are subject to a weaker/stronger ISRF, Y_{CII} might be larger/smaller.

In Fig. 12Map of Y_{CII}, as defined in Eq. (11Correlation with column densitiesequation.5.11), for the $x - z$ projection of the L10 simulation (left). The regions within the black contour line in the map belong to pixels that we assume to be observable, fulfilling $I_{[CII]} \geqslant 0.5$ K km s^{-1}. On the right, the normalized histograms of the Y_{CII} values for the total map (blue) and the observable pixels (green) for all three projections together are presented. X_i/X_{tot} indicates the fraction of pixels in every bin. figure.caption.15 we plot a map of Y_{CII} for the L10 simulation in the $x - z$ projection in the left panel. The regions within the black contour mark the observable region ($I_{[CII]} \geqslant 0.5$ K km s^{-1}). Over the whole map, the Y_{CII} distribution covers a large range with values between $10^{20} \lesssim Y_{CII} \lesssim 10^{24}$ cm^{-2} (K km s^{-1})$^{-1}$. All high values occur only in regions with unobservably low [C II] intensities. The median of the Y_{CII} distribution is at $2.83^{+3.15}_{-1.18} \times 10^{21}$ cm^{-2} (K km s^{-1})$^{-1}$, taking all pixels in the map into account, or $1.09^{+0.44}_{-0.36} \times 10^{21}$ cm^{-2} (K km s^{-1})$^{-1}$ if only observable pixels are considered. The other projections behave similarly. We therefore show in the right panel of Fig. 12Map of Y_{CII}, as defined in Eq. (11Correlation with column densitiesequation.5.11), for the $x - z$ projection of the L10 simulation (left). The regions within the black contour line in the map belong to pixels that we assume to be observable, fulfilling $I_{[CII]} \geqslant 0.5$ K km s^{-1}. On the right, the normalized his-

---

[7] The fit was obtained using the CURVE_FIT python package, where the error estimate is based on the Jacobian.
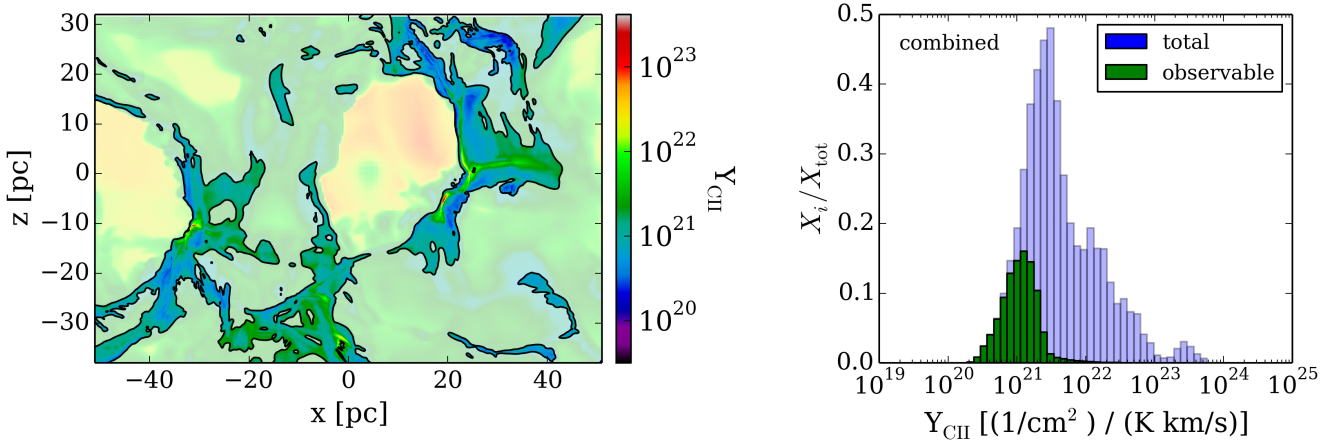
Figure 12. Map of Y_{CII}, as defined in Eq. (11Correlation with column densitiesequation.5.11), for the $x - z$ projection of the L10 simulation (left). The regions within the black contour line in the map belong to pixels that we assume to be observable, fulfilling $I_{[CII]} \geqslant 0.5$ K s^{-1}. On the right, the normalized histograms of the Y_{CII} values for the total map (blue) and the observable pixels (green) for all three projections together are presented. X_i/X_{tot} indicates the fraction of pixels in every bin.

Table 4. List of the 25%, 50%, and 75% values of the Y_{CII} factor for the $x - z$ projection and the combined data for all three projections. The upper part of the table contains the Y_{CII} values of those regions which are assumed to be observable ($I_{[CII]} \geqslant 0.5$ K s^{-1}), and the lower part contains the Y_{CII} values obtained when the whole map is taken into account.

projection		Y_{CII} [cm^{-2} (K km s^{-1})$^{-1}$]			
		25%	50% (median)	75%	mean
$x - z$	observable	7.27×10^{20}	1.09×10^{21}	1.53×10^{21}	1.37×10^{21}
combined	observable	7.48×10^{20}	1.11×10^{21}	1.59×10^{21}	1.44×10^{21}
$x - z$	total	1.65×10^{21}	2.83×10^{21}	5.98×10^{21}	7.23×10^{21}
combined	total	1.76×10^{21}	3.21×10^{21}	9.39×10^{21}	1.49×10^{22}

tograms of the Y_{CII} values for the total map (blue) and the observable pixels (green) for all three projections together are presented. X_i/X_{tot} indicates the fraction of pixels in every bin. figure.caption.15 the histogram of the fraction of pixels as a function of Y_{CII} combined for all three projections ($\Delta \log_{10}(Y_{CII}) = 0.08$). The blue coloured histogram represents all values in the map, whereas the green one includes only observable pixels. Table 4List of the 25%, 50%, and 75% values of the Y_{CII} factor for the $x - z$ projection and the combined data for all three projections. The upper part of the table contains the Y_{CII} values of those regions which are assumed to be observable ($I_{[CII]} \geqslant 0.5$ K s^{-1}), and the lower part contains the Y_{CII} values obtained when the whole map is taken into account.table.caption.16 lists the 25th and 75th percentiles as well as the median value of the Y_{CII} factors for the $x - z$ projection and the data combined for all three projections. If we assume that the observation of a molecular cloud is unresolved, we would obtain a single intensity value for the whole region ($\sim$0.4 K s^{-1} as the average integrated intensity over the whole map), and might have one single value for the column density ($\sim 6.3 \times 10^{20}$ cm^{-2}). Using these simplified values for obtaining Y_{CII}, we find $\sim 1.5 \times 10^{21}$ cm^{-2} (K km s^{-1})$^{-1}$.

We further analyse the correlation between Y_{CII} and $I_{[CII]}$ for the observable part in more detail. Express-

ing Eq. (8Correlation with column densitiesequation.5.8) in terms of Y_{CII} yields

$$\log_{10} \left(\frac{Y_{CII}}{cm^{-2}(K \ km \ s^{-1})^{-1}} \right) =$$

$$-(0.298 \pm 0.165) \times \log_{10} \left(\frac{I_{[CII]}}{K \ km \ s^{-1}} \right) + (21.0722 \pm 0.0005).$$

$$(12)$$

The y-intercept of this relation ($y = 21.0722 \pm 0.0005$) corresponds to a column density of $N_{tot} = 10^y \approx 10^{21}$ cm^{-2}. This is approximately the column density at which $A_V = 1$, and where the transition between atomic to molecular gas happens. Taking Eq. (12Correlation with column densitiesequation.5.12) might be better for extracting the Y_{CII} value and the total column density N_{tot} for an observation than just taking e.g. the median value of Y_{CII}. To prove this, we calculate the distribution of Y_{CII} around the fitting function Eq. (12Correlation with column densitiesequation.5.12) (not shown). The width of this distribution, measured with the interquartile range, $d_{iqr} = 7.5 \times 10^{20}$ cm^{-2} (K km s^{-1})$^{-1}$, is smaller compared to the distribution of the observable Y_{CII} values shown in the right panel of Fig. 12Map of Y_{CII}, as defined in Eq. (11Correlation with column densitiesequation.5.11), for the $x - z$ projection of the L10 simulation (left). The regions

within the black contour line in the map belong to pixels that we assume to be observable, fulfilling $I_{[\text{CII}]} \geqslant 0.5$ K km s^{-1}. On the right, the normalized histograms of the Y_{CII} values for the total map (blue) and the observable pixels (green) for all three projections together are presented. X_i/X_{tot} indicates the fraction of pixels in every bin. figure.caption.15, with $d_{\text{iqr}} = 8.4 \times 10^{20}$ cm^{-2} (K km s^{-1})$^{-1}$, which represents a small improvement. To further estimate the difference between the fit and the Y_{CII} distribution from the simulation, we calculate the deviation between the distribution of Y_{CII} values and the ones calculated with Eq. (12Correlation with column densitiesequation.5.12) as

$$\Delta_{Y_{\text{CII}}} = |Y_{\text{CII}}^{\text{fit}} - Y_{\text{CII}}^{\text{map}}| \cdot \frac{100\%}{Y_{\text{CII}}^{\text{fit}}}. \tag{13}$$

We find that 25%, 50%, 75% of the pixels have $\Delta_{Y_{\text{CII}}} \approx 16\%$, 33%, 54%, respectively.

We test the practical value of the Y_{CII} factor fitting by applying Eq. (12Correlation with column densitiesequation.5.12) to the simulation L10 in the $x - z$ projection. The whole simulation box contains a total mass of 8.4×10^4 M$_\odot$. About 70% of this mass ($m_{\text{proj}} = 5.8 \times 10^4$ M$_\odot$) is situated in regions of the $x - z$ projection above the assumed detection limit ($I_{[\text{CII}]} \geqslant 0.5$ K km s^{-1}). If we take only the pixels above the detection limit and recalculate the total mass of the cloud using Eq. (12Correlation with column densitiesequation.5.12), we obtain $m_{\text{cloud, YCII}} = (4.1_{-0.320}^{+0.405}) \times 10^4$ M$_\odot$, which is in the range of 65% to 78% of the projected mass. In Fig. 13Histogram of the column densities of the observed area (blue), and of the column densities calculated with Eq. (12Correlation with column densitiesequation.5.12) using the opacity affected [C II] integrated intensity. X_i/X_{tot} indicates the fraction of pixels as a function of the logarithmically binned column densities N_{tot}. We underestimate the projected mass by 22% to 35%.figure.caption.17 we show the histogram of the column densities of the observed area (blue) and of the column densities recalculated from the integrated opacity affected [C II] intensity (green) with a bin size of $\Delta \log_{10}(Y_{\text{CII}}) = 0.08$. We do not reproduce the small column densities at low intensities and likewise miss the high column density regions.

However, when using the mean value and the interquartile range of the Y_{CII} distribution $(1.11_{-0.37}^{+0.48} \times 10^{21}$ cm^{-2} (K km s^{-1})$^{-1})$ for estimating the mass, we obtain $m_{\text{cloud, YCII}} = (11.25_{-3.65}^{+4.85}) \times 10^4$ M$_\odot$. This corresponds to masses between 130% and 280% of m_{proj}. We therefore conclude that Y_{CII} is not constant, but it is better estimated when assuming that it scales as $I_{[\text{CII}]}^{-0.3}$ (Eq. (12Correlation with column densitiesequation.5.12)).

6 DISCUSSION

6.1 Discussion of general results

In observations, optical depth effects of the [C II] line emission are mainly discussed in the context of regions with star formation feedback, as in classical PDRs (Boreiko &
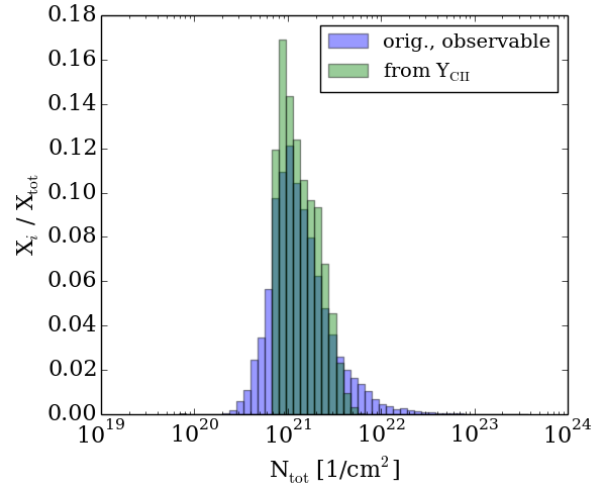
Figure 13. Histogram of the column densities of the observed area (blue), and of the column densities calculated with Eq. (12Correlation with column densitiesequation.5.12) using the opacity affected [C II] integrated intensity. X_i/X_{tot} indicates the fraction of pixels as a function of the logarithmically binned column densities N_{tot}. We underestimate the projected mass by 22% to 35%.

Betz 1997; Stacey et al. 2010; Graf et al. 2012; Ossenkopf et al. 2013; Neri et al. 2014; Gullberg et al. 2015). When studying molecular clouds in observations, the [C II] line emission is assumed to be optically thin (e.g. Langer et al. 2010; Pineda et al. 2013; Langer et al. 2014). In our model of a forming molecular cloud before the onset of star formation we find the [C II] line emission to be optically thick in ~40% of the assumed observable region (defined as the area where $I_{[\text{CII}]} \geqslant 0.5$ K km s^{-1}) with optical depths up to $\tau \sim 10$. However, only a small part of the map is affected by high optical depths. Therefore, the approach of the [C II] line emission being "effectively optically thin" holds for most of the emission (Goldsmith et al. 2012), so that the [C II] line emission is linearly correlated with the C$^+$ column density (c.f. Fig. 11Correlation between the integrated [C II] line intensity (opacity affected) and the column densities of the total gas (left), H (middle) and C$^+$ (right). The top row shows the distribution including the data for the whole map. The red vertical lines mark the assumed observable limit of $I_{[\text{CII}]} \geqslant 0.5$ K km s^{-1}. The bottom row shows only the observable data with their overplotted linear fits. The colour-coding indicates the fraction of pixels with respect to the entire map (X_i/X_{tot}) and to the observable area ($X_i/X_{\text{tot, obs}}$). figure.caption.14).

For studying the local properties (density, temperature, visual extinction, and molecular gas fraction) of the [C II] emitting gas, we perform a second set of radiative transfer simulations, where we treat the C$^+$ gas as optically thin. For this we reduce the C$^+$ abundance such that this corresponds to emission from ^{13}C$^+$. We find that in the studied young molecular cloud the [C II] line emission originates from the cold, atomic gas phase with temperatures between ~40 K and ~65 K and number densities of the total gas between ~50 cm^{-3} and ~440 cm^{-3}. In the absence of turbulence, molecular hydrogen forms in the ISM on a timescale

$t_{H_2} \approx 1\,\mathrm{Gyr}/n$ (Hollenbach et al. 1971), corresponding to a timescale of between 2 and 20 Myr for gas in this density range. The presence of turbulence can accelerate the H_2 formation rate by a factor of a few (Glover et al. 2010), but even when we account for this, much of the [C II]-bright gas still has an H_2 formation timescale that is comparable to or longer than the age of the cloud at the moment that we analyze it. It is therefore quite likely that the atomic hydrogen in the cloud is still in the process of becoming molecular at the time at which we analyse the cloud (see Section 2.1SILCC Zoom-in simulationssubsection.2.1 above). During this transition phase, we expect much of the [C II] emission to come from gas dominated by atomic hydrogen, in line with what we find in this study, but in more evolved clouds it is likely that a greater fraction of the emission would come from H_2-dominated gas (c.f. Glover & Smith 2016).

As our chemical network includes carbon as CO and C^+, but misses the atomic form, we might overestimate the amount of CO in the simulation (Glover & Clark 2012). Including the atomic carbon would also reduce the amount of C^+. However, the main effect of this would be to shift the ranges in temperature and density of the [C II] emitting gas to slightly higher temperatures and lower densities. Therefore, the correlation between [C II] emission and the atomic gas in the transition phase would remain.

6.2 Comparison with observations

There are studies analysing the origin of the emission on a galaxy wide scale, as it is done in the GOT C+ survey along different lines of sight (e.g. Pineda et al. 2013; Velusamy & Langer 2014). By comparing the [C II] components with ancillary H I, ^{12}CO, ^{13}CO and $C^{18}O$ emission, they identify the phase from which the [C II] line emission originates. According to Pineda et al. (2013) and Pineda et al. (2014), 30–50% of the [C II] line emission stems from PDRs, 25–28% from CO-dark H_2, 21–25% from gas associated with H I, and 4–20% from the ionized gas phase. Since our simulations do not include the feedback from stars, we only account for the 50% to 70% of the emission that does not come from PDRs or the ionized gas phase. We find that about 20% of the [C II] line emission stems from H_2 dominated gas, where more than 50% of hydrogen is in form of H_2, and 80% of the [C II] line emission originates from the atomic gas phase. Thus, our fraction associated with the atomic gas phase is larger than found by Pineda et al. (2013, 2014). The difference likely arises from the fact that the GOT C+ survey includes numerous molecular clouds, with a range of ages. Those clouds which are young and are forming, such as the cloud in our simulation, will predominately contribute to the [C II] emission associated with the atomic phase. Clouds which are more evolved will predominately contribute to the [C II] emission associated with the molecular phase. We will investigate the effect of the cloud age on the [C II] emission in a follow-up paper.

The [C II] line emission is studied in infrared dark clouds e.g. by Beuther et al. (2014), or recently Bisbas et al. (2018). They find the [C II] line emission to exhibit diverse mor-

phologies, ranging from a non-detection in the most quiescent region, to stronger emission in more actively star-forming regions. According to Beuther et al. (2014), the [C II] line emission traces the environment around the dense gas and is sensitive to the external UV field. Our simulations confirm that the [C II] line emission is a good tracer for the envelope of the densest parts of molecular clouds, tracing mostly atomic hydrogen. We further suggest that the [C II] line emission is even detectable before the onset of star formation. However, the emission properties as well as the derived Y_{CII} (see Section 5Correlation with column densitiessection.5) are expected to depend on the local interstellar radiation field. Here we study a cloud which is irradiated by an ISRF of $G_0 = 1.7$. For a UV dominated cloud, we expect a correlation with the molecular gas, observable in CO. Thus, it is therefore important to have multispecies observations to better understand the physical properties of a cloud. Beuther et al. (2014) further find promising kinematic signatures in their [C II] detections, and a strong velocity gradient for G48.66. From this, they suggest to discern between various cloud assembly processes by using observations of [C II]. In our model of a forming molecular cloud we find the [C II] emission to stem from the atomic envelope. Since the cloud is still in formation and the gas collapsing inwards, we expect this movement of the gas to be visible in kinematic signatures of the [C II] line. A future work will address these kinematic signatures.

6.3 Comparison with simulations

The origin of the [C II] line emission is likewise studied in simulations. Smith et al. (2014) simulate the ISM within a torus mimicking the outer parts of the Milky Way. Their simulations are done with the moving mesh code AREPO (Springel 2010), accounting for a galactic potential, but neglecting the feedback from star formation and neglecting self-gravity. They simulate the chemical evolution of the gas with the same chemical network as we use (Glover & Mac Low 2007a,b; Nelson & Langer 1997). In Glover & Smith (2016) they study the [C II] line properties in those simulations. Instead of taking a radiative transfer code for synthetic observations, they estimate the [C II] emissivity in every cell assuming that the line is optically thin. Thus, the emission they calculate is comparable to the optically thin [C II] line emission in our work. Glover & Smith (2016) find a small part of the [C II] line emission to originate from the warm neutral medium (WNM) with densities around $0.2\ \mathrm{cm}^{-3}$ and temperatures around 10^4 K. We do not see a contribution from the WNM. However, our zoom-in region only contains the molecular cloud, and we therefore do not account for the large volume of warm gas that Glover & Smith (2016) have in their simulation. They obtain a larger contribution from the cold atomic, and CO-dark molecular gas, which is broadly distributed around densities of $20\ \mathrm{cm}^{-3}$ and temperatures of 100 K. Similar to Smith et al. (2014) and Glover & Smith (2016), we do not include stellar feedback in the underlying 3D simulation, and therefore only study the [C II] line emission from the cold, molecular and atomic gas, but not from PDRs. Our results show in the same way a large contribution from the cold gas phase, although we find that most of the emission comes from gas in the temperature range

$40 < T < 65$ K, while Glover & Smith (2016) find that the largest contribution comes from gas close to 100 K. Glover & Smith (2016) further distinguish the gas by its amount of atomic hydrogen and find that half of the emission from the cold gas phase is associated with H_2-dominated regions (defined as having more than 50% of the hydrogen mass in the form of H_2), counting this fraction as CO-dark H_2. We, on the other hand, only find $\sim 20\%$ of the [C II] line emission associated with the molecular gas phase following the same definition. These differences may be due to the fact that the simulation presented in Glover & Smith (2016) does not contain self-gravity, thus the clouds extend to much lower densities and are unlikely to ever form much CO. Here, we focus on a single gravitationally-bound molecular cloud.

Accurso et al. (2017) investigate in simulations how much of the [C II] line emission ($f_{\rm [CII],mol}$) is correlated with the molecular gas phase. Their setup consists of a multiphase 3D radiative interface that couples the stellar spectrophotometric code STARBURST99 (Leitherer et al. 1999, 2010; Vázquez & Leitherer 2005; Conroy 2013) with the photoionization and astrochemistry codes MOCASSIN (Ercolano et al. 2003) and 3D-PDR (Bisbas et al. 2012). They model entire star-forming regions and thus, their simulations include the part of feedback that we do not account for. On the other hand, when modelling the spherically symmetric geometry with an ionizing source in the centre of the cloud, hydrodynamical effects, as turbulence and shocks, are neglected (Accurso et al. 2017). Our simulations in contrast focus on the hydrodynamical evolution of the gas before the onset of star formation in a turbulent molecular cloud. Accurso et al. (2017) assume that the physical conditions found in each of their clouds can represent the average physical conditions found on galaxy-wide scales. By using a Bayesian formalism and statistical weights for the clouds, they fit $f_{\rm [CII],mol}$ as a function of the density, dust mass fraction, specific star formation rate (SSFR), and the metallicity. In general, $f_{\rm [CII],mol}$ increases with the density and decreases with SSFR. For a galaxy matching the parameter space of the Milky Way, they find that around 75% of the [C II] emission is correlated with the molecular gas (where the molecular gas is defined as all gas with more than 1% of hydrogen in the form of H_2). In our observable area, 99.8% of the [C II] emission comes from molecular gas defined in this way. Our simulations (Walch et al. 2015; Girichidis et al. 2016, S17) represent an ISM, in which C^+ is formed dynamically, and turbulent mixing of the chemical species is taken into account (see S17). The model of Accurso et al. (2017), on the other hand, represents an ISM dominated by UV radiation. They further assume that the chemistry has reached equilibrium, which is both not required and not the case in our setup. The different approaches have an impact on the formation of the PDRs in the model, that in turn cause the difference in the results.

Overall, we find that the substructure of the molecular cloud, which is set by gas accretion, turbulence, self-gravity, and the local radiation field, is essentially shaping the [C II] emitting regions, which envelop the dense, CO-rich filaments and cores. The origin of the [C II] emission is hence sensitive to the physical conditions as well as the evolutionary stage of the molecular cloud.

7 CONCLUSION

We present synthetic [C II] line emission maps of a molecular cloud embedded in a piece of a galactic disc. The turbulent molecular cloud simulation has been carried out with the 3D AMR code FLASH (Fryxell et al. 2000; Dubey et al. 2008) including a simple chemical network and is presented in the SILCC-Zoom project (Seifried et al. 2017). We study this molecular cloud at an early evolutionary stage, before the onset of star formation, with an ISRF of $G_0 = 1.7$. The radiative transfer simulations for the [C II] line are done with RADMC–3D (Dullemond 2012). We do not assume the gas to be in LTE. Instead, we calculate the level populations by considering collisions with H_2, H, and electrons and use the LVG approximation.

We investigate the influence of the spatial resolution on the synthetic emission maps. Different versions of the zoom-ins were done for spatial resolutions ranging from $dx = 3.9$ pc to $dx = 0.122$ pc. We find the [C II] intensity distributions of the maps to converge for resolutions better than ~ 0.25 pc. All further analyses are based on the highest resolution run with $dx = 0.122$ pc (run L10).

If we assume an observable limit of $I_{\rm [CII]} \geqslant 0.5$ K km s^{-1}, then we recover 80% of the total [C II] luminosity. This demonstrates that a molecular cloud should be observable in [C II] line emission prior to the onset of massive star formation, potentially allowing us to trace the assembly of the cloud. The observable luminosity stems from $16\% - 27\%$ of the total area of the map. [^{12}C II] becomes optically thick in $\sim 10\%$ of the total map area, corresponding to $\sim 40\%$ of the observable area. Although the [C II] line emission behaves as "effectively optically thin" (Goldsmith et al. 2012), observers should bare in mind that the observed [C II] emission becomes optically thick up to $\tau \sim 10$.

To determine the physical properties of the [C II] emitting gas, we compare the opacity affected [^{12}C II] emission with an optically thin equivalent, corresponding to [^{13}C II] emission. We do this by reducing the number density of C^+ by a factor of 107. We find the [C II] line emission to be emitted from gas in the temperature range of 43 K and 64 K and in the number density range of 53 cm^{-3} and 438 cm^{-3}, while the visual extinction is between 0.50 and 0.91. We further study the correlation with molecular hydrogen and find that $\lesssim 20\%$ of the [C II] emission comes from gas which is dominated by H_2, meaning that more than 50% of the hydrogen is in the form of H_2. Thus, we conclude that the [C II] line emission is generally correlated with atomic hydrogen in transition to the molecular phase in our young, dynamically evolving molecular cloud. As a consequence, we conclude that [C II] is not a suitable tracer for CO–dark H_2 in this scenario. Instead, we expect the H I line to be correlated with the [C II] line emission.

In observational studies the [C II] line emission is used

to constrain the total column density as well as the C^+ column densities (Langer et al. 2014; Goicoechea et al. 2015). Here we define a new quantity, the Y_{CII} factor, as the ratio between the total gas column density and the integrated [C II] line emission, that can be used in those studies. The median value is $Y_{CII} \approx 1.1 \times 10^{21}$ cm^{-2} (K km s^{-1})$^{-1}$, but to constrain the total gas column density (and hence the total mass of the cloud) using Y_{CII} and $I_{[CII]}$, it is better to use $Y_{CII} \propto I_{[CII]}^{-0.3}$. We note that this particular value of Y_{CII} applies to our young molecular cloud, which is embedded in a uniform ISRF with strength $G_0 = 1.7$. We expect Y_{CII} to be lower / higher in regions with a higher / lower ISRF.

APPENDIX A: DETAILS OF THE RADIATIVE TRANSFER SIMULATIONS

A1 RADMC–3D

RADMC–3D provides the possibility of calculating the line emission of ions under the condition that the local thermodynamic equilibrium is not fulfilled. It solves the radiative transfer equation

$$\frac{dI_\nu(\zeta, s)}{ds} = j_\nu(\zeta, s) - \alpha_\nu(\zeta, s) I_\nu(\zeta, s), \quad (A1)$$

with the emission and absorption coefficients $j_\nu(\zeta, s)$ and $\alpha_\nu(\zeta, s)$. Following the local notation of van der Tak et al. (2007), these coefficients are calculated internally in RADMC–3D by

$$j_\nu(\zeta, s) = \frac{h\nu}{4\pi} n_{C^+} x_u A_{ul} \phi_{ul}(\zeta, s) \quad (A2)$$

$$\alpha_\nu(\zeta, s) = \frac{h\nu}{4\pi} n_{C^+} (x_l B_{lu} - x_u B_{ul}) \phi_{ul}(\zeta, s). \quad (A3)$$

Here, n_{C^+} is the number density of C^+, x_u and x_l are the fractional level populations of the upper ($^2P_{3/2}$, indicated with u) and lower ($^2P_{1/2}$, indicated with l) level. A_{ul}, B_{ul} and B_{lu} are the Einstein coefficients. The profile function $\phi_{ul}(\zeta, s)$ is used in its co-moving form $\tilde{\phi}_{ul}$ around the line-center frequency ν_{ul}. It is approximated by a Doppler profile:

$$\tilde{\phi}_{ul} = \frac{c}{a_{tot} \nu_{ul} \sqrt{\pi}} \exp\left\{ -\frac{c^2(\nu - \nu_{ul})^2}{a_{tot}^2 \nu_{ul}^2} \right\}, \quad (A4)$$

where $a_{tot} = \sqrt{a_{therm}^2 + a_{turb}^2}$ is the line-width composed of the contributions from the thermal line-width, $a_{therm} = \sqrt{\frac{2k_B T}{\mu m_H}}$, and a turbulent line-width a_{turb}. We set $a_{turb} = a_{therm}$. The kinetic temperature is inserted for T, k_B is the Boltzmann constant, m_H is the mass of a hydrogen atom, and μ is the molecular weight of the emitting $^{12}C^+$ particle ($\mu = 12$).

To calculate the emission and absorption coefficients, and hence, the radiative transfer equation, the fractional level populations of C^+ (x_u, x_l) is needed. The level populations of C^+ is considered not to be in the local thermal equilibrium (LTE), since a large fraction of the gas is in dilute medium. RADMC–3D uses the large velocity gradient (LVG, Sobolev 1960; Ossenkopf 1997; Shetty et al. 2011a) approximation, also known as Sobolev approximation, for calculating the level populations. In that approximation the optical depth τ_{ul}^{LVG} is derived from the absolute value of the velocity gradient $|\nabla \vec{v}|$. In general, the optical depth is defined as $d\tau_{ul} \equiv \alpha_{ul} ds$. Following the local formulation of van der Tak et al. (2007), this can be expressed as

$$\tau_{ul}^{LVG} = \frac{ch}{4\pi} \frac{n_{C^+}}{1.064 |\nabla \vec{v}|} (x_l B_{lu} - x_u B_{ul}). \quad (A5)$$

This is used to calculate the escape probability β_{ul}. For the line within the LVG approximation the escape probability is set to

$$\beta_{ul} = \frac{1 - e^{-\tau_{ul}}}{\tau_{ul}}, \quad (A6)$$

(Sobolev 1960; van der Tak et al. 2007). Although this is an assumption for a different geometry, it is used in RADMC–3D (e.g. Ossenkopf 1997, for a further discussion). β_{ul} is in turn taken to derive the line integrated mean intensity J_{ul} as

$$J_{ul} = (1 - \beta_{ul}) S_{ul} + \beta_{ul} J_{ul}^{bg}. \quad (A7)$$

S_{ul} denotes the source function with

$$S_{ul} = \frac{j_\nu}{\alpha_\nu}, \quad (A8)$$

and J_{ul}^{bg} is the background radiation field at the rest frequency. Since at $\nu_{[CII]}$ the continuum background radiation in the diffuse interstellar medium is low (Draine 2011) and in observations the continuum background is likewise subtracted, we neglect it for our purpose.

A further ingredient needed for calculating the level populations is the set of collisional excitation and de-excitation rates between C^+ and its main collision partners, ortho-H_2, para-H_2, H and e^-. We use collisional de-excitation rates taken from the Leiden Atomic and Molecular Database (LAMDA, Schöier et al. 2005). For ortho-H_2 and para-H_2, these come originally from Wiesenfeld & Goldsmith (2014), for atomic H from Barinovs et al. (2005) and for electrons from Wilson & Bell (2002). The fits given in LAMDA do not cover the whole range of temperatures encountered in our simulation, and so at high temperatures we extrapolate the rates following (Goldsmith et al. 2012, see Fig. A1The collisional de-excitation rates for the different collisional partners of C^+ as a function of the kinetic temperature T_{kin}. The rates for the electrons, atomic hydrogen and ortho- and para-molecular hydrogen (red triangles, green squares and blue and magenta circles, respectively) are taken from the Leiden database (Schöier et al. 2005). To cover the full temperature range of the simulations, we interpolate these database rates and extrapolate them towards higher temperatures. For both ortho- and para-H_2 we assume the database value at $T = 500$ K for higher temperatures.figure.caption.19). Given the collisional de-excitation rate coefficient for each collision partner, the total rate then follows as

$$C_{ul} = \sum_{cp} n_{cp} R_{ul}^{cp}, \qquad (A9)$$

where n_{cp} is the number density of the collision partner. The collisional excitation rate then follows via the principle of detailed balance:

$$C_{lu} = C_{ul} \frac{g_u}{g_l} e^{-\frac{\Delta E}{k_B T}}, \qquad (A10)$$

where g_u and g_l are the statistical weights of the upper and lower levels respectively.

The Einstein coefficients and the collisional rates per C^+ ion are used to calculate the level populations of the upper and lower level (x_u and x_l, respectively). They are derived by solving the equations of statistical equilibrium. In the case of the fine structure transition of the C^+ ion with the two levels i and j this reduces to

$$-\left[x_u A_{ul}\beta_{ul} + (x_u B_{ul} - x_l B_{lu})\beta_{ul}J_{ul}^{bg}\right] + [x_l C_{lu} - x_u C_{ul}] = 0. \qquad (A11)$$

Since the escape probability β_{ul} changes with the level populations, equations (A6RADMC–3Dequation.A.6) and (A11RADMC–3Dequation.A.11) are iteratively solved until convergence is reached.

In cases where the co-moving line-width is narrower than the Doppler shift, there could be velocity channels with no contribution to the emission in the simulations. However, these so-called Doppler jumps are numerical artefacts and do not occur in nature. In order to avoid them in our simulations we use the Doppler-catching method,
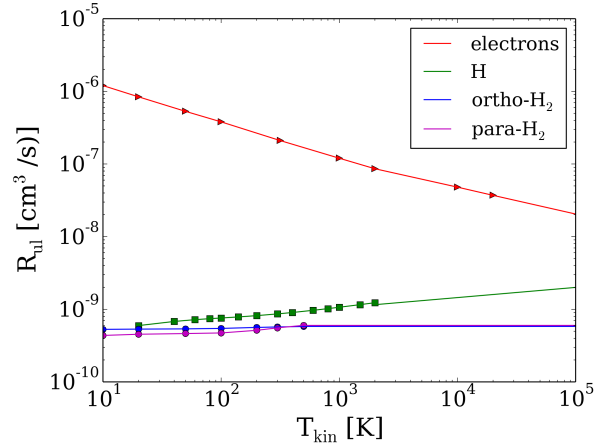

Figure A1. The collisional de-excitation rates for the different collisional partners of C^+ as a function of the kinetic temperature T_{kin}. The rates for the electrons, atomic hydrogen and ortho- and para-molecular hydrogen (red triangles, green squares and blue and magenta circles, respectively) are taken from the Leiden database (Schöier et al. 2005). To cover the full temperature range of the simulations, we interpolate these database rates and extrapolate them towards higher temperatures. For both ortho- and para-H_2 we assume the database value at $T = 500$ K for higher temperatures.

described by Pontoppidan et al. (2009), which ensures a smooth behaviour (see Shetty et al. 2011a,b).

A2 Calculating the collisional rates

$R(H_2)$: For molecular hydrogen the LAMDA database provides de-excitation rate coefficients for temperatures $T_{kin} \leqslant 500$ K for ortho- and para-H_2 (Wiesenfeld & Goldsmith 2014). There is no good fit for the coefficients distinguishing between the two nuclear spin states that could be extrapolated to higher temperatures. We expect that collisions between C^+ and H_2 at temperatures $T > 500$ K will not contribute significantly to the [C II] line emission, as in the simulations there is a negligible amount of H_2 in regions warmer than 500 K ($\sim 0.1\%$ of the H_2 mass). Therefore, at $T > 500$ K, we assume that the collisional rate coefficients for collisions with ortho- and para-H_2 have the same values as for $T = 500$ K.

$R(H)$: For atomic hydrogen the de-excitation collisional rates are given for temperatures $T_{kin} \leqslant 2\,000$ K in the Leiden database using the data by Barinovs et al. (2005). Goldsmith et al. (2012) fitted the data in the range $20 \text{ K} \leqslant T_{kin} \leqslant 2\,000$ K and found the relation between the coefficients and the kinetic temperature to be

$$R_{ul}(H) = 7.6 \times 10^{-10} \left(\frac{T_{kin}}{100\,\text{K}}\right)^{0.14} \text{cm}^3\text{s}^{-1}. \qquad (A12)$$

We assume that the same relation holds at $T > 2\,000$ K.

$R(e^-)$: De-excitation rate coefficients for collisions with electrons are given for $T_{kin} \leqslant 20\,000$ K in the Leiden database (Wilson & Bell 2002). For the coefficients at larger temper-

Figure B1. Distribution of the intensities in the [C II] emission maps (opacity affected) at different resolution, calculated assuming a microturbulence according to Larson (1981). X_i/X_{tot} denotes the fraction of pixels in every intensity bin. For comparison, the distribution of intensities for the simulation at L10, for which a thermal microturbulence was assumed, is plotted as black line. The microturbulence has only a negligible influence on the emission maps, and does not influence the behaviour of convergence among the resolution levels.

atures we use again a fit by Goldsmith et al. (2012)

$$R_{ul}(e^-) = 8.7 \times 10^{-8} \left(\frac{T_e}{2000\,\mathrm{K}} \right)^{-0.37} \mathrm{cm^3 s^{-1}}, \quad (A13)$$

where we replace the electron temperature T_e by the kinetic temperature T_{kin}.

APPENDIX B: TESTING LARSON'S MICROTURBULENCE

To test whether our choice of the microturbulence influences our results, we additionally calculate the synthetic [C II] line emission maps assuming a microturbulence according to Larson (1981), following his eq. (20) that is

$$\frac{a_{turb}}{\mathrm{km\,s^{-1}}} = 1.1 \times \left(\frac{L}{\mathrm{pc}} \right)^{0.38}. \quad (B1)$$

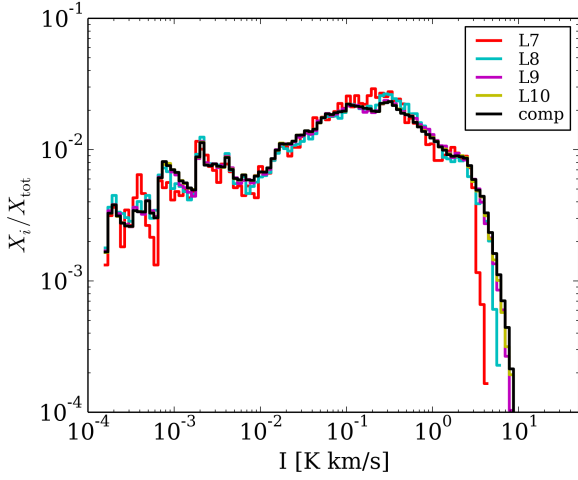In Fig. B1Distribution of the intensities in the [C II] emission maps (opacity affected) at different resolution, calculated assuming a microturbulence according to Larson (1981). X_i/X_{tot} denotes the fraction of pixels in every intensity bin. For comparison, the distribution of intensities for the simulation at L10, for which a thermal microturbulence was assumed, is plotted as black line. The microturbulence has only a negligible influence on the emission maps, and does not influence the behaviour of convergence among the resolution levels. figure.caption.20 we show the distribution of the intensities of those [C II] line emission maps (opacity affected) for the different resolution levels with a bin size of $\Delta \log_{10}(I\,[\mathrm{K\,km\,s^{-1}}]) = 0.05$. For comparison, we plot the distribution for the simulation at L10, as calculated in Section 3Synthetic emission maps at different resolutionssection.3 with the thermal microtubulence (black

Figure C1. Distribution of the intensities for the simulation at L10, when assuming different escape probability length scales. X_i/X_{tot} denotes the fraction of pixels in every intensity bin. $L_{max} = \infty$ is chosen for the calculations within this work. Specifying L_{max} for the simulation has only a negligible influence on the synthetic emission map.

Figure C2. Mass-weighted 2D-PDF of the excitation temperatures T_{ex} for the opacity affected [C II] line emission calculated without an escape probability length ($L_{max} = \infty$, x-axis) and with $L_{max} = 2$ pc (y-axis). Colour-coded is the fraction of mass in the distribution. A similar plot comparing the calculation with optical depth effects and the optically thin case is shown in Fig. 9Mass weighted 2D-PDF of the excitation temperatures, T_{ex}, of the opacity affected and the optically thin [C II] line emission.figure.caption.12.

line). There are only minor differences between the maps at L10 with the different microturbulence, and no improvement in convergence when taking a microturbulence according to Larson.

APPENDIX C: TESTING ESCAPE PROBABILITY LENGTHS

When calculating the optical depth for the radiative transfer (Eq. (A5RADMC–3Dequation.A.5)), a velocity gradient is

required. If the velocity gradient becomes too small, or a velocity field is not even given in the simulation, there is the possibility to specify an escape probability length scale to RADMC–3D, so that it calculates the optical depth as

$$\tau_{ul}^{\mathrm{L}} = \frac{ch}{4\pi} \frac{n_{\mathrm{C}^+} L_{\max}}{\sqrt{\pi} a_{\mathrm{tot}}} \left(x_l B_{lu} - x_u B_{ul} \right). \qquad \text{(C1)}$$

Typically, $L_{\max}$ is set to the size of the simulation box. If an escape length probability is given, RADMC–3D calculates τ_{ul}^{LVG} and τ_{ul}^{L} and takes the minimum of it for the radiative transfer calculation. We test whether setting an escape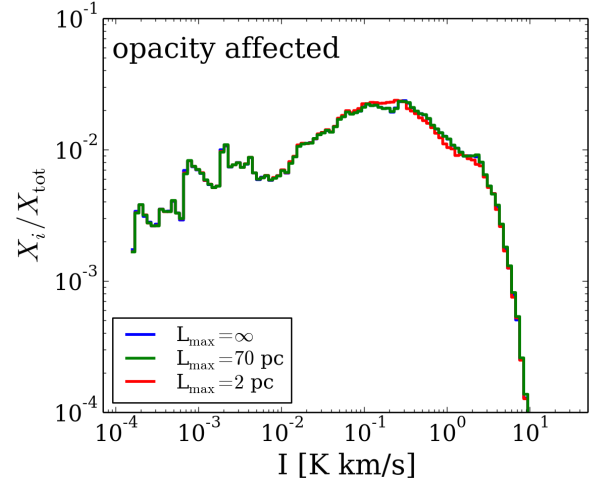 probability length scale influences the resulting synthetic emission maps. Figure C1Distribution of the intensities for the simulation at L10, when assuming different escape probability length scales. X_i/X_{tot} denotes the fraction of pixels in every intensity bin. $L_{\max} = \infty$ is chosen for the calculations within this work. Specifying $L_{\max}$ for the simulation has only a negligible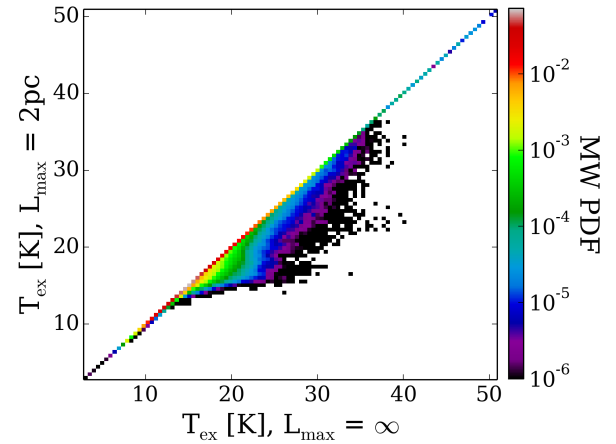 influence on the synthetic emission map.figure.caption.21 shows the distribution of the intensities when no escape probability length is given ($L_{\max} \to \infty$), and when it is set to 70 pc and 2 pc. An $L_{\max}$ of 70 pc corresponds to the size of the simulation box, and $L_{\max} = 2$ pc we chose for reason of comparison ($\Delta \log_{10}(I \, [\mathrm{K\,km\,s^{-1}}]) = 0.05$). As can be seen in Fig. C1Distribution of the intensities for the simulation at L10, when assuming different escape probability length scales. X_i/X_{tot} denotes the fraction of pixels in every intensity bin. $L_{\max} = \infty$ is chosen for the calculations within this work. Specifying $L_{\max}$ for the simulation has only a negligible influence on the synthetic emission map.figure.caption.21, the escape probability length scale has only an negligible influence on the intensity distribution. Figure C2Mass-weighted 2D-PDF of the excitation temperatures T_{ex} for the opacity affected [C II] line emission calculated without an escape probability length ($L_{\max} = \infty$, x-axis) and with $L_{\max} = 2$ pc (y-axis). Colour-coded is the fraction of mass in the distribution. A similar plot comparing the calculation with optical depth effects and the optically thin case is shown in Fig. 9Mass weighted 2D-PDF of the excitation temperatures, T_{ex}, of the opacity affected and the optically thin [C II] line emission.figure.caption.12. figure.caption.22 shows 2D-PDF (histogram) of the scatter plot between the excitation temperatures calculated with $L_{\max} = \infty$ and $L_{\max} = 2$ pc. This plot is similar to the one shown in Fig. 9Mass weighted 2D-PDF of the excitation temperatures, T_{ex}, of the opacity affected and the optically thin [C II] line emission.figure.caption.12, where the excitation temperatures of the [C II] line emission in the opacity affected and the optically thin case are presented. The x-axes in both plots are identical. When setting $L_{\max} = 2$ pc, T_{ex} is similar to T_{ex} of the optically thin emission for low intensities (cf. Fig. 9Mass weighted 2D-PDF of the excitation temperatures, T_{ex}, of the opacity affected and the optically thin [C II] line emission.figure.caption.12). For higher intensities, the excitation temperature of the calculation with $L_{\max} = 2$ pc has intermediate values between the optically thick and thin case. The smaller the value of $L_{\max}$ is chosen, the more T_{ex} approaches to the optically thin solution.

APPENDIX D: SPECTRAL RESOLUTION

In the synthetic [C II] emission maps for Section 3Synthetic emission maps at different resolutionssection.3 we
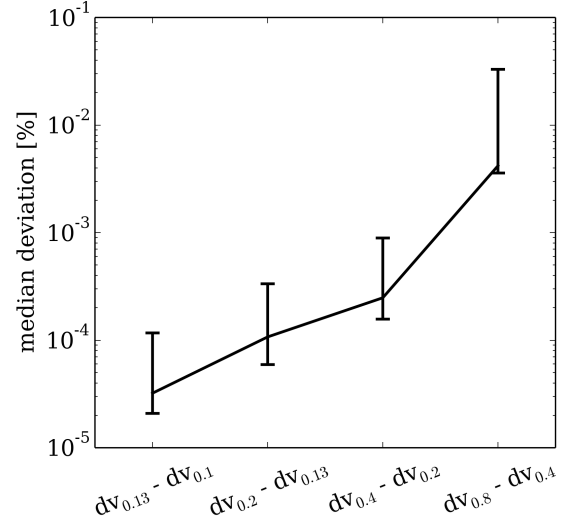

Figure D1. Deviation of the synthetic [C II] line emission maps (opacity affected) at different spectral resolutions.

chose a spectral resolution of $dv = 0.2$ km s^{-1}, inspired by the spectral resolution of the integrated line maps of the *Herschel* [C II] line emission in Orion. As the velocity range of ± 20 km s^{-1} in our synthetic observations is fixed, this corresponds to 201 channel maps. We test different spectral resolutions by setting the amount of channels to 401, 301, 201, 101 and 51, corresponding to $dv = 0.1, 0.13, 0.2, 0.4, 0.8$ km s^{-1}, respectively. We calculate for every pixel p in two spectral adjacent emission maps (p^{dv_x}, $p^{dv(x+1)}$, respectively) the deviation of the integrated intensities in percentage by

$$\Delta_v = (p^{dv_x} - p^{dv(x+1)}) \cdot \frac{100\%}{p^{dv_x}}. \qquad \text{(D1)}$$

We derive the median and the interquartile range of the absolute value of the distribution of Δ_v. The median is the value for that 50% of the distribution is included, and the interquartile range the difference at which 25% and 75% of the distribution are included. We show the result in Fig. D1Deviation of the synthetic [C II] line emission maps (opacity affected) at different spectral resolutions.figure.caption.23, where we present on the y-axis the median of the deviation Δ_v with the interquartile range as error bars, and indicate on the x-axis the spectral resolutions of the synthetic emission maps. Since the median deviation of Δ_v is less than 0.001% between the spectral resolutions $dv = 0.1$ and $dv = 0.2$ km s^{-1}, we conclude that a spectral resolution of $dv = 0.2$ km s^{-1} is sufficient to capture the [C II] line emission.

APPENDIX E: CONVERGENCE STUDIES

E1 Convergence of the emission maps

We investigate whether and how the change in resolution influences the synthetic [C II] line emission maps in the
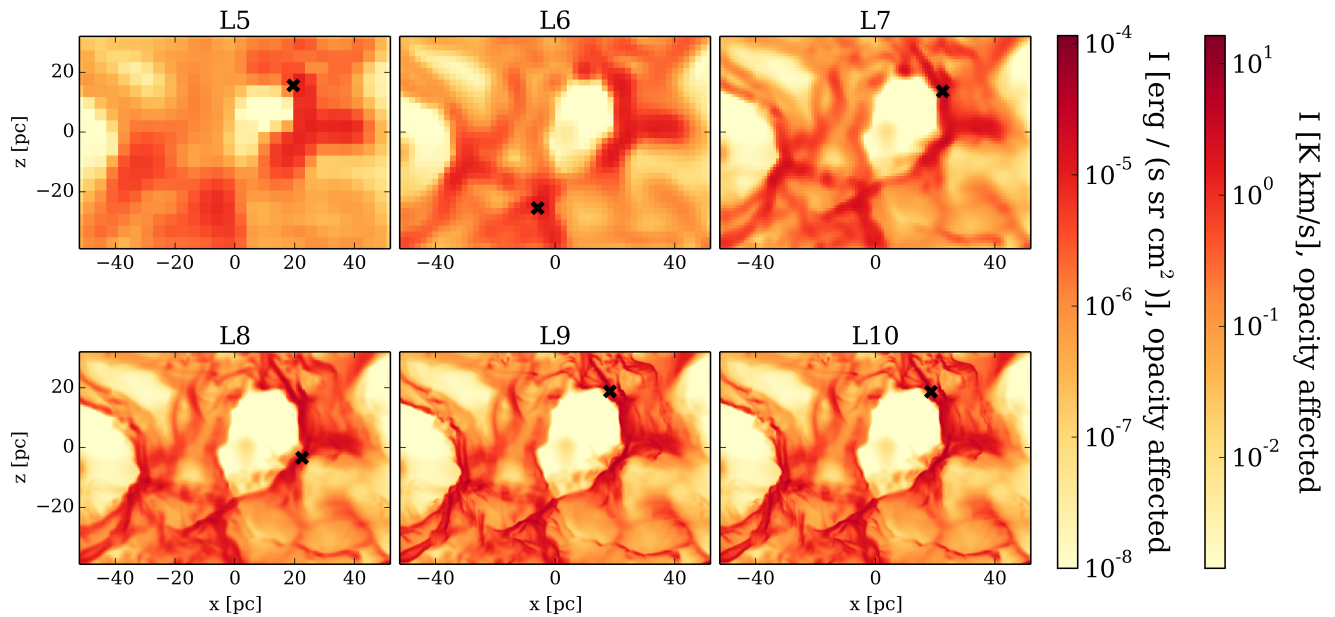
Figure E1. Synthetic [C II] line emission maps (opacity affected) of the zoom-in simulation at different resolution levels as listed in Table 1List of the zoom-in simulations used here, as named in S17 (first column) and named after their resolution level (second column). The third column gives the spatial resolution dx. Further, we list for the $x - z$ projection the integrated peak intensities and total luminosities $L_{\rm tot}$ for the opacity affected and the optically thin [C II] synthetic emission maps (fourth to seventh column, respectively; see Section 3Synthetic emission maps at different resolutionssection.3). table.caption.1. The crosses mark the position with the maximum integrated intensity in each map. From the refinement level L5 to L9 this position changes due to varying optical depths.

opacity affected and optically thin case. Figs. E1Synthetic [C II] line emission maps (opacity affected) of the zoom-in simulation at different resolution levels as listed in Table 1List of the zoom-in simulations used here, as named in S17 (first column) and named after their resolution level (second column). The third column gives the spatial resolution dx. Further, we list for the $x - z$ projection the integrated peak intensities and total luminosities $L_{\rm tot}$ for the opacity affected and the optically thin [C II] synthetic emission maps (fourth to seventh column, respectively; see Section 3Synthetic emission maps at different resolutionssection.3). table.caption.1. The crosses mark the position with the maximum integrated intensity in each map. From the refinement level L5 to L9 this position changes due to varying optical depths. figure.caption.24 and E2Similar to Fig. E1Synthetic [C II] line emission maps (opacity affected) of the zoom-in simulation at different resolution levels as listed in Table 1List of the zoom-in simulations used here, as named in S17 (first column) and named after their resolution level (second column). The third column gives the spatial resolution dx. Further, we list for the $x - z$ projection the integrated peak intensities and total luminosities $L_{\rm tot}$ for the opacity affected and the optically thin [C II] synthetic emission maps (fourth to seventh column, respectively; see Section 3Synthetic emission maps at different resolutionssection.3). table.caption.1. The crosses mark the position with the maximum integrated intensity in each map. From the refinement level L5 to L9 this position changes due to varying optical depths. figure.caption.24, the synthetic [C II] line emission maps for the optically thin case. The crosses mark the position

with the maximum integrated intensity in each map. Here, the position remains in the same area from L6 on, as the emission is optically thin. figure.caption.25 show the [C II] synthetic emission maps for these cases for all resolution levels for the x-z projection at an evolutionary time of $t_{\rm tot} = 13.9$ Myr. The crosses mark the positions of the maximum integrated intensity for each resolution. The values of the peak intensities and the luminosities integrated over these maps are summarised in Table 1List of the zoom-in simulations used here, as named in S17 (first column) and named after their resolution level (second column). The third column gives the spatial resolution dx. Further, we list for the $x - z$ projection the integrated peak intensities and total luminosities $L_{\rm tot}$ for the opacity affected and the optically thin [C II] synthetic emission maps (fourth to seventh column, respectively; see Section 3Synthetic emission maps at different resolutionssection.3). table.caption.1 in the fourth to seventh column. For opacity affected [C II], the position of the maximum of the integrated intensity jumps around for different refinement levels (L5 to L9), although the structures within the molecular clouds maintain their general morphology for all resolution levels. Regions that were optically thin before can become optically thick with a higher resolution, because the density fluctuations along one line of sight become more distinct. For the optically thin [C II] synthetic emission maps (Fig. E2Similar to Fig. E1Synthetic [C II] line emission maps (opacity affected) of the zoom-in simulation at different resolution levels as listed in Table 1List of the zoom-in simulations used here, as named in S17 (first column) and named after their resolution level (second column). The third column

Figure E2. Similar to Fig. E1Synthetic [C II] line emission maps (opacity affected) of the zoom-in simulation at different resolution levels as listed in Table 1List of the zoom-in simulations used here, as named in S17 (first column) and named af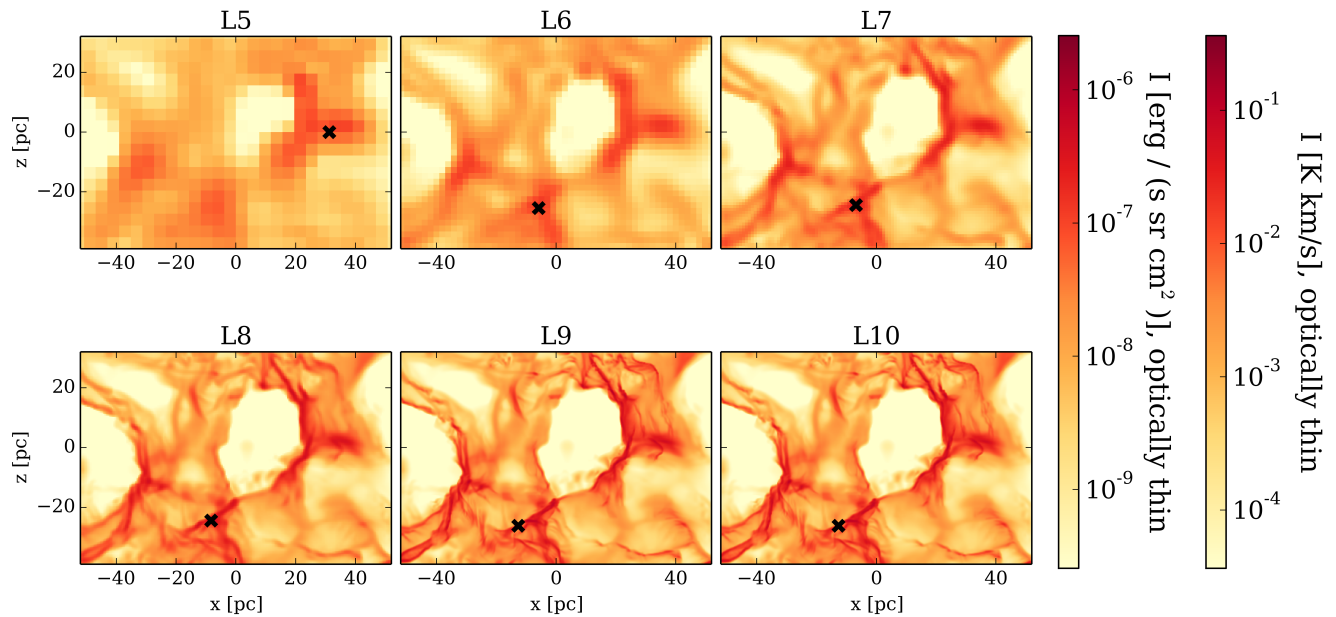ter their resolution level (second column). The third column gives the spatial resolution dx. Further, we list for the $x-z$ projection the integrated peak intensities and total luminosities $L_{\rm tot}$ for the opacity affected and the optically thin [C II] synthetic emission maps (fourth to seventh column, respectively; see Section 3Synthetic emission maps at different resolutionssection.3). table.caption.1. The crosses mark the position with the maximum integrated intensity in each map. From the refinement level L5 to L9 this position changes due to varying optical depths. figure.caption.24, the synthetic [C II] line emission maps for the optically thin case. The crosses mark the position with the maximum integrated intensity in each map. Here, the position remains in the same area from L6 on, as the emission is optically thin.

gives the spatial resolution dx. Further, we list for the $x-z$ projection the integrated peak intensities and total luminosities $L_{\rm tot}$ for the opacity affected and the optically thin [C II] synthetic emission maps (fourth to seventh column, respectively; see Section 3Synthetic emission maps at different resolutionssection.3). table.caption.1. The crosses mark the position with the maximum integrated intensity in each map. From the refinement level L5 to L9 this position changes due to varying optical depths. figure.caption.24, the synthetic [C II] line emission maps for the optically thin case. The crosses mark the position with the maximum integrated intensity in each map. Here, the position remains in the same area from L6 on, as the emission is optically thin. figure.caption.25) the position of the maximum integrated intensity changes only a little from refinement level L6 on, since the emission is not influenced by optical depth effects.

Figs. E3Total [C II] luminosity (opacity affected; left) for different resolution levels as listed in Table 1List of the zoom-in simulations used here, as named in S17 (first column) and named after their resolution level (second column). The third column gives the spatial resolution dx. Further, we list for the $x-z$ projection the integrated peak intensities and total luminosities $L_{\rm tot}$ for the opacity affected and the optically thin [C II] synthetic emission maps (fourth to seventh column, respectively; see Section 3Synthetic emission maps at different resolutionssection.3). table.caption.1, shown for all three projections. In the mid-

dle panel the median of the deviation between the synthetic emission maps of two adjacent resolution levels is shown. As error bars we use the interquartile range. The median of the deviation between the map of L9 and L10 is $< 0.5\%$. In the right panel, the peak intensities against the resolution level is plotted, which is not converged. figure.caption.26 and E4The same as Fig. E3Total [C II] luminosity (opacity affected; left) for different resolution levels as listed in Table 1List of the zoom-in simulations used here, as named in S17 (first column) and named after their resolution level (second column). The third column gives the spatial resolution dx. Further, we list for the $x-z$ projection the integrated peak intensities and total luminosities $L_{\rm tot}$ for the opacity affected and the optically thin [C II] synthetic emission maps (fourth to seventh column, respectively; see Section 3Synthetic emission maps at different resolutionssection.3). table.caption.1, shown for all three projections. In the middle panel the median of the deviation between the synthetic emission maps of two adjacent resolution levels is shown. As error bars we use the interquartile range. The median of the deviation between the map of L9 and L10 is $< 0.5\%$. In the right panel, the peak intensities against the resolution level is plotted, which is not converged. figure.caption.26, but for the synthetic [C II] line emission maps in the optically thin case. For the total luminosity all projections fall on to one curve. figure.caption.27 show in the left panels the [C II] luminosities integrated over the whole maps for the opacity affected (Fig. E3Total [C II] luminosity (opacity affected; left) for different resolution levels as listed in Table 1List
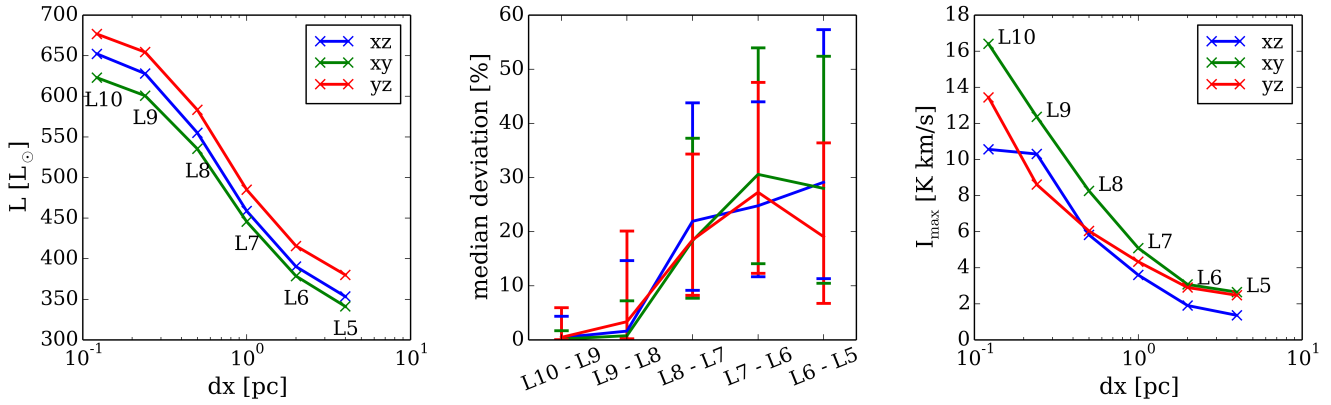
Figure E3. Total [C II] luminosity (opacity affected; left) for different resolution levels as listed in Table 1List of the zoom-in simulations used here, as named in S17 (first column) and named after their resolution level (second column). The third column gives the spatial resolution dx. Further, we list for the $x - z$ projection the integrated peak intensities and total luminosities L_{tot} for the opacity affected and the optically thin [C II] synthetic emission maps (fourth to seventh column, respectively; see Section 3Synthetic emission maps at different resolutionssection.3). table.caption.1, shown for all three projections. In the middle panel the median of the deviation between the synthetic emission maps of two adjacent resolution levels is shown. As error bars we use the interquartile range. The median of the deviation between the map of L9 and L10 is $< 0.5\%$. In the right panel, the peak intensities against the resolution level is plotted, which is not converged.

Figure E4. The same as Fig. E3Total [C II] luminosity (opacity affected; left) for different resolution levels as listed in Table 1List of the zoom-in simulations used here, as named in S17 (first column) and named after their resolution level (second column). The third column gives the spatial resolution dx. Further, we list for the $x - z$ projection the integrated peak intensities and total luminosities L_{tot} for the opacity affected and the optically thin [C II] synthetic emission maps (fourth to seventh column, respectively; see Section 3Synthetic emission maps at different resolutionssection.3). table.caption.1, shown for all three projections. In the middle panel the median of the deviation between the synthetic emission maps of two adjacent resolution levels is shown. As error bars we use the interquartile range. The median of the deviation between the map of L9 and L10 is $< 0.5\%$. In the right panel, the peak intensities against t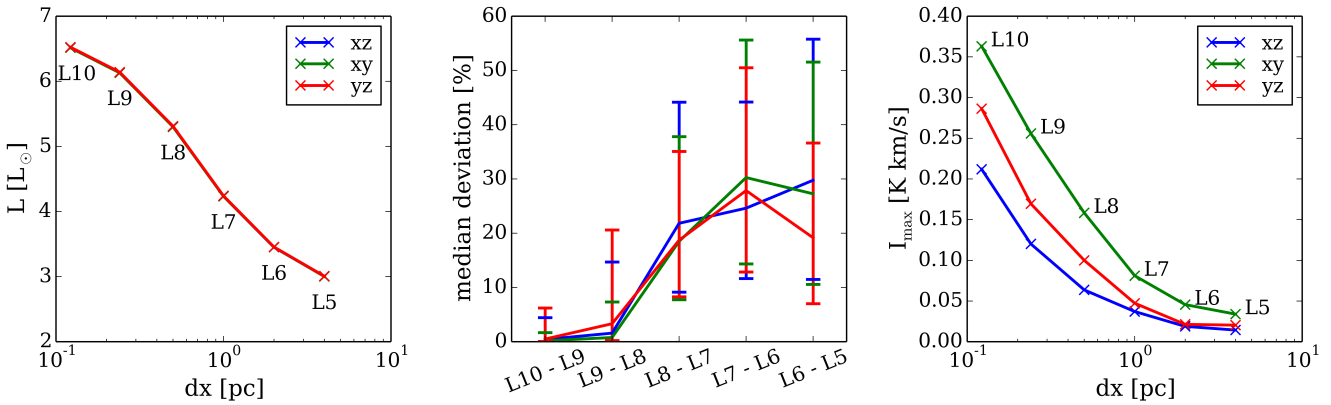he resolution level is plotted, which is not converged. figure.caption.26, but for the synthetic [C II] line emission maps in the optically thin case. For the total luminosity all projections fall on to one curve.

of the zoom-in simulations used here, as named in S17 (first column) and named after their resolution level (second column). The third column gives the spatial resolution dx. Further, we list for the $x - z$ projection the integrated peak intensities and total luminosities L_{tot} for the opacity affected and the optically thin [C II] synthetic emission maps (fourth to seventh column, respectively; see Section 3Synthetic emission maps at different resolutionssection.3). table.caption.1, shown for all three projections. In the middle panel the median of the deviation between the synthetic

emission maps of two adjacent resolution levels is shown. As error bars we use the interquartile range. The median of the deviation between the map of L9 and L10 is $< 0.5\%$. In the right panel, the peak intensities against the resolution level is plotted, which is not converged. figure.caption.26) and optically thin case (Fig. E4The same as Fig. E3Total [C II] luminosity (opacity affected; left) for different resolution levels as listed in Table 1List of the zoom-in simulations used here, as named in S17 (first column) and named after their resolution level (second column). The third col-

umn gives the spatial resolution dx. Further, we list for the $x - z$ projection the integrated peak intensities and total luminosities L_{tot} for the opacity affected and the optically thin [C II] synthetic emission maps (fourth to seventh column, respectively; see Section 3Synthetic emission maps at different resolutionssection.3). table.caption.1, shown for all three projections. In the middle panel the median of the deviation between the synthetic emission maps of two adjacent resolution levels is shown. As error bars we use the interquartile range. The median of the deviation between the map of L9 and L10 is $< 0.5\%$. In the right panel, the peak intensities against the resolution level is plotted, which is not converged. figure.caption.26, but for the synthetic [C II] line emission maps in the optically thin case. For the total luminosity all projections fall on to one curve. figure.caption.27) as a function of the maximum refinement level. The best refinement level L10 with $dx = 0.122$ pc is on the left hand side of each plot. For all three projections in both cases the luminosity increases with higher spatial resolution. Note that for the optically thin synthetic [C II] line emission the luminosities are the same for each projection. The difference between the maps of two adjacent resolution levels decreases with smaller dx. This can be seen in the middle panels, where we compare the integrated intensity values of the maps of two adjacent resolution levels, Lx and L($x + 1$). First we reduce the amount of pixels of the higher resolution to the lower one by averaging the values of four pixels p_i^{x+1} in each map of the resolution level L($x + 1$) to one value. Then we compare the result with the pixel value p^x of the map of level Lx:

$$\Delta = \left(p^x - \frac{1}{4} \sum_{i=1}^{4} p_i^{x+1} \right) \cdot \frac{100\%}{p^x}. \qquad (E1)$$

We take the median of the absolute values of the differences Δ for all pixels and present them on the y-axis of the plot. The median is the point at which 50% of the distribution is included. The x-axis indicates the corresponding resolution levels. The error bars are given by the interquartile range of the distribution of Δ, which are those points at which 25% and 75% of the pixels in the distribution are included. This technique has the advantage of being robust against individual spikes in a distribution. As seen from this plot the deviation decreases for all projections when going to higher resolution levels. This is in agreement with the smaller increase of the luminosity of the maps with higher resolution level, as shown in the left panels of Figs. E3Total [C II] luminosity (opacity affected; left) for different resolution levels as listed in Table 1List of the zoom-in simulations used here, as named in S17 (first column) and named after their resolution level (second column). The third column gives the spatial resolution dx. Further, we list for the $x - z$ projection the integrated peak intensities and total luminosities L_{tot} for the opacity affected and the optically thin [C II] synthetic emission maps (fourth to seventh column, respectively; see Section 3Synthetic emission maps at different resolutionssection.3). table.caption.1, shown for all three projections. In the middle panel the median of the deviation between the synthetic emission maps of two adjacent resolution levels is shown. As error bars we use the interquartile range. The median of the deviation between the map of L9 and L10 is $< 0.5\%$. In the right panel,
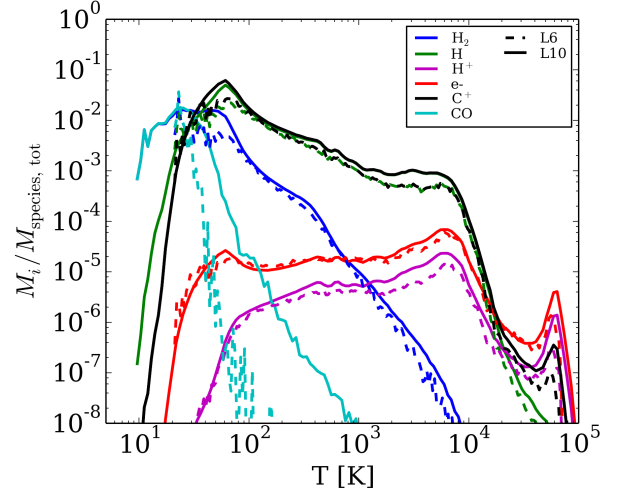

Figure E5. Comparison of the mass-weighted temperature distributions for all species for the resolution level L6 (dashed line) and the highest resolution level L10 (solid line). $M_i/M_{species, tot}$ denotes the mass fraction of each species normalized to the total hydrogen mass (for H and H_2), the total carbon mass (for C^+ and CO), or the total electron mass, respectively (see Section 4.1Temperature dependencesubsection.4.1).

the peak intensities against the resolution level is plotted, which is not converged. figure.caption.26 and E4The same as Fig. E3Total [C II] luminosity (opacity affected; left) for different resolution levels as listed in Table 1List of the zoom-in simulations used here, as named in S17 (first column) and named after their resolution level (second column). The third column gives the spatial resolution dx. Further, we list for the $x - z$ projection the integrated peak intensities and total luminosities L_{tot} for the opacity affected and the optically thin [C II] synthetic emission maps (fourth to seventh column, respectively; see Section 3Synthetic emission maps at different resolutionssection.3). table.caption.1, shown for all three projections. In the middle panel the median of the deviation between the synthetic emission maps of two adjacent resolution levels is shown. As error bars we use the interquartile range. The median of the deviation between the map of L9 and L10 is $< 0.5\%$. In the right panel, the peak intensities against the resolution level is plotted, which is not converged. figure.caption.26, but for the synthetic [C II] line emission maps in the optically thin case. For the total luminosity all projections fall on to one curve. figure.caption.27. The intensity distributions of the maps converge within 0.5% at L9 to L10. The right panels shows the peak intensity for every projection as a function of dx. Since the position of the maximum integrated intensity is not fixed and the volume density still increases with higher resolution level, we do not expect convergence for [C II] in this property.

E2 Chemical composition at different resolution levels

To see whether the abundances of the collisional partners as a function of the temperature change with the resolution level, we show the mass-weighted temperature distributions

of all chemical species for the levels L6 (dashed lines) and L10 (solid lines) in Fig. E5Comparison of the mass-weighted temperature distributions for all species for the resolution level L6 (dashed line) and the highest resolution level L10 (solid line). $M_i/M_{\mathrm{species,\ tot}}$ denotes the mass fraction of each species normalized to the total hydrogen mass (for H and H_2), the total carbon mass (for C^+ and CO), or the total electron mass, respectively (see Section 4.1Temperature dependencesubsection.4.1). figure.caption.28. In general, the gas at low temperatures is better resolved for L10, down to $T \sim 10$ K for all chemical species. For L6, the gas has only temperatures above 20 K and CO is not resolved. For the other species, the qualitative behaviour of the distributions are similar for $T \gtrsim 100$ K. Between 50 K and 100 K, H_2, H and C^+ are less abundant in L6 compared to L10. This explains the lower luminosity we find in L5 (cf. Figs. E3Total [C II] luminosity (opacity affected; left) for different resolution levels as listed in Table 1List of the zoom-in simulations used here, as named in S17 (first column) and named after their resolution level (second column). The third column gives the spatial resolution dx. Further, we list for the $x - z$ projection the integrated peak intensities and total luminosities L_{tot} for the opacity affected and the optically thin [C II] synthetic emission maps (fourth to seventh column, respectively; see Section 3Synthetic emission maps at different resolutionssection.3). table.caption.1, shown for all three projections. In the middle panel the median of the deviation between the synthetic emission maps of two adjacent resolution levels is shown. As error bars we use the interquartile range. The median of the deviation between the map of L9 and L10 is $< 0.5\%$. In the right panel, the peak intensities against the resolution level is plotted, which is not converged. figure.caption.26 and E4The same as Fig. E3Total [C II] luminosity (opacity affected; left) for different resolution levels as listed in Table 1List of the zoom-in simulations used here, as named in S17 (first column) and named after their resolution level (second column). The third column gives the spatial resolution dx. Further, we list for the $x - z$ projection the integrated peak intensities and total luminosities L_{tot} for the opacity affected and the optically thin [C II] synthetic emission maps (fourth to seventh column, respectively; see Section 3Synthetic emission maps at different resolutionssection.3). table.caption.1, shown for all three projections. In the middle panel the median of the deviation between the synthetic emission maps of two adjacent resolution levels is shown. As error bars we use the interquartile range. The median of the deviation between the map of L9 and L10 is $< 0.5\%$. In the right panel, the peak intensities against the resolution level is plotted, which is not converged. figure.caption.26, but for the synthetic [C II] line emission maps in the optically thin case. For the total luminosity all projections fall on to one curve. figure.caption.27 and Table 1List of the zoom-in simulations used here, as named in S17 (first column) and named after their resolution level (second column). The third column gives the spatial resolution dx. Further, we list for the $x - z$ projection the integrated peak intensities and total luminosities L_{tot} for the opacity affected and the optically thin [C II] synthetic emission maps (fourth to seventh column, respectively; see Section 3Synthetic emission maps at different resolutionssection.3). table.caption.1). In

general, the distributions for H and C^+ are aligned for the L6 and L10 simulations.

REFERENCES

Accurso G., Saintonge A., Bisbas T. G., Viti S., 2017, MNRAS, 464, 3315

Appleton P. N., Guillard P., Boulanger F., Cluver M. E., et al., 2013, ApJ, 777, 66

Barinovs Ğ., van Hemert M. C., Krems R., Dalgarno A., 2005, ApJ, 620, 537

Bertram E., Glover S. C. O., Clark P. C., Ragan S. E., Klessen R. S., 2016, MNRAS, 455, 3763

Beuther H., Ragan S. E., Ossenkopf V., Glover S., Henning T., Linz H., Nielbock M., Krause O., Stutzki J., Schilke P., Güsten R., 2014, A&A, 571, A53

Bisbas T. G., Bell T. A., Viti S., Yates J., Barlow M. J., 2012, MNRAS, 427, 2100

Bisbas T. G., Tan J. C., Csengeri T., Wu B., Lim W., Caselli P., Güsten R., Ricken O., Riquelme D., 2018, MNRAS

Bisbas T. G., Tanaka K. E. I., Tan J. C., Wu B., Nakamura F., 2017, ApJ, 850, 23

Boreiko R. T., Betz A. L., 1997, ApJS, 111, 409

Bouchut F., Klingenberg C., Waagan K., 2007, Numerische Mathematik, 108, 7

Clark P. C., Glover S. C. O., Klessen R. S., 2012, MNRAS, 420, 745

Conroy C., 2013, ARA&A, 51, 393

Croxall K. V., Smith J. D., Wolfire M. G., Roussel H., Sandstrom K. M., Draine B. T., et al., 2012, ApJ, 747, 81

De Looze I., Baes M., Bendo G. J., Cortese L., Fritz J., 2011, MNRAS, 416, 2712

De Looze I., Cormier D., Lebouteiller V., Madden S., Baes M., Bendo G. J., Boquien M., Boselli A., Clements e., 2014, A&A, 568, A62

Draine B. T., 1978, ApJS, 36, 595

Draine B. T., 2011, Physics of the Interstellar and Intergalactic Medium. Princeton University Press

Duarte-Cabral A., Dobbs C. L., 2016, MNRAS, 458, 3667

Dubey A., Fisher R., Graziani C., Jordan IV G. C., Lamb D. Q., Reid L. B., Rich P., Sheeler D., Townsley D., Weide K., 2008, in Pogorelov N. V., Audit E., Zank G. P., eds, Numerical Modeling of Space Plasma Flows Vol. 385 of Astronomical Society of the Pacific Conference Series, Challenges of Extreme Computing using the FLASH code. p. 145

Dullemond C. P., , 2012

Dullemond C. P., Juhasz A., Pohl A., Sereshti F., Shetty R., Peters T., Commercon B., Flock M., , 2012, RADMC-3D: A multi-purpose radiative transfer tool, Astrophysics Source Code Library

Ercolano B., Barlow M. J., Storey P. J., Liu X.-W., 2003, MNRAS, 340, 1136

Fryxell B., Olson K., Ricker P., Timmes F. X., Zingale M., Lamb D. Q., MacNeice P., Rosner R., Truran J. W., Tufo H., 2000, ApJS, 131, 273

Gatto A., Walch S., Low M.-M. M., Naab T., Girichidis P., Glover S. C. O., Wünsch R., Klessen R. S., Clark P. C.,

Baczynski C., Peters T., Ostriker J. P., Ibáñez-Mejía J. C., Haid S., 2015, MNRAS, 449, 1057

Gatto A., Walch S., Naab T., Girichidis P., Wünsch R., Glover S. C. O., Klessen R. S., Clark P. C., Peters T., Derigs D., Baczynski C., Puls J., 2017, MNRAS, 466, 1903

Girichidis P., Walch S., Naab T., Gatto A., Wünsch R., Glover S. C. O., Klessen R. S., Clark P. C., Peters T., Derigs D., Baczynski C., 2016, MNRAS, 456, 3432

Glover S. C. O., Clark P. C., 2012, MNRAS, 421, 116

Glover S. C. O., Federrath C., Mac Low M.-M., Klessen R. S., 2010, MNRAS, 404, 2

Glover S. C. O., Mac Low M.-M., 2007a, ApJS, 169, 239

Glover S. C. O., Mac Low M.-M., 2007b, ApJ, 659, 1317

Glover S. C. O., Smith R. J., 2016, MNRAS, 462, 3011

Goicoechea J. R., Teyssier D., Etxaluze M., Goldsmith P. F., Ossenkopf V., Gerin M., et al., 2015, ApJ, 812, 75

Goldsmith P. F., Langer W. D., Pineda J. L., Velusamy T., 2012, ApJS, 203, 13

Graf U. U., Simon R., Stutzki J., Colgan S. W. J., Guan X., Güsten R., Hartogh P., Honingh C. E., Hübers H.-W., 2012, A&A, 542, L16

Gullberg B., De Breuck C., Vieira J. D., Weiß A., Aguirre J. E., Aravena M., Béthermin M., et al., 2015, MNRAS, 449, 2883

Habing H. J., 1968, Bull. Astron. Inst. Netherlands, 19, 421

Hailey-Dunsheath S., Nikola T., Stacey G. J., Oberst T. E., Parshley S. C., Benford D. J., Staguhn J. G., Tucker C. E., 2010, ApJ, 714, L162

Herrera-Camus R., Bolatto A. D., Wolfire M. G., Smith J. D., Croxall K. V., Kennicutt R. C., Calzetti D., Helou G., Walter F., Leroy A. K., Draine B., Brandl B. R., Armus L., Sandstrom K. M., et al., 2015, ApJ, 800, 1

Hollenbach D. J., Werner M. W., Salpeter E. E., 1971, ApJ, 163, 165

Kapala M. J., Sandstrom K., Groves B., Croxall K., Kreckel K., Dalcanton J., Leroy A., Schinnerer E., Walter F., Fouesneau M., 2015, ApJ, 798, 24

Kennicutt Jr. R. C., 1998, ApJ, 498, 541

Klessen R. S., Glover S. C. O., 2016, Star Formation in Galaxy Evolution: Connecting Numerical Models to Reality, Saas-Fee Advanced Course, Volume 43. ISBN 978-3-662-47889-9. Springer-Verlag Berlin Heidelberg, 2016, p. 85, 43, 85

Langer W. D., Pineda J. L., Velusamy T., 2014, A&A, 564, A101

Langer W. D., Velusamy T., Pineda J. L., Goldsmith P. F., Li D., Yorke H. W., 2010, A&A, 521, L17

Langer W. D., Velusamy T., Pineda J. L., Willacy K., Goldsmith P. F., 2014, A&A, 561, A122

Larson R. B., 1981, MNRAS, 194, 809

Leitherer C., Ortiz Otálvaro P. A., Bresolin F., Kudritzki R.-P., Lo Faro B., Pauldrach A. W. A., Pettini M., Rix S. A., 2010, ApJS, 189, 309

Leitherer C., Schaerer D., Goldader J. D., Delgado R. M. G., Robert C., Kune D. F., de Mello D. F., Devost D., Heckman T. M., 1999, ApJS, 123, 3

Lesaffre P., Pineau des Forêts G., Godard B., Guillard P., Boulanger F., Falgarone E., 2013, A&A, 550, A106

Lique F., Werfelli G., Halvick P., Stoecklin T., Faure A., Wiesenfeld L., Dagdigian P. J., 2013, J. Chem. Phys., 138,

Nelson R. P., Langer W. D., 1997, ApJ, 482, 796

Neri R., Downes D., Cox P., Walter F., 2014, A&A, 562, A35

Olsen K., Greve T. R., Narayanan D., Thompson R., Davé R., Niebla Rios L., Stawinski S., 2017, ApJ, 846, 105

Ossenkopf V., 1997, New Astron., 2, 365

Ossenkopf V., Röllig M., Neufeld D. A., Pilleri P., Lis D. C., Fuente A., van der Tak F. F. S., Bergin E., 2013, A&A, 550, A57

Peters T., Naab T., Walch S., Glover S. C. O., Girichidis P., Pellegrini E., Klessen R. S., Wünsch R., Gatto A., Baczynski C., 2017, MNRAS, 466, 3293

Pineda J. L., Langer W. D., Goldsmith P. F., 2014, A&A, 570, A121

Pineda J. L., Langer W. D., Velusamy T., Goldsmith P. F., 2013, A&A, 554, A103

Pontoppidan K. M., Meijerink R., Dullemond C. P., Blake G. A., 2009, ApJ, 704, 1482

Rachford B. L., Snow T. P., Destree J. D., Ross T. L., Ferlet R., Friedman S. D., Gry C., Jenkins E. B., Morton D. C., Savage B. D., Shull J. M., Sonnentrucker P., Tumlinson J., Vidal-Madjar A., Welty D. E., York D. G., 2009, ApJS, 180, 125

Röllig M., Abel N. P., Bell T., Bensch F., Black J., Ferland G. J., Jonkheid B., Kamp I., et al., 2007, A&A, 467, 187

Schmidt M., 1959, ApJ, 129, 243

Schöier F. L., van der Tak F. F. S., van Dishoeck E. F., Black J. H., 2005, A&A, 432, 369

Seifried D., Walch S., Girichidis P., Naab T., Wünsch R., Klessen R. S., Glover S. C. O., Peters T., Clark P., 2017, MNRAS, 472, 4797

Sembach K. R., Howk J. C., Ryans R. S. I., Keenan F. P., 2000, ApJ, 528, 310

Shetty R., Glover S. C., et al., 2011a, MNRAS, 412, 1686

Shetty R., Glover S. C., et al., 2011b, MNRAS, 415, 3253

Smith R. J., Glover S. C. O., Clark P. C., Klessen R. S., Springel V., 2014, MNRAS, 441, 1628

Sobolev V. V., 1960, Moving envelopes of stars

Spitzer Jr. L., 1942, ApJ, 95, 329

Springel V., 2010, ARA&A, 48, 391

Stacey G. J., Geis N., Genzel R., Lugten J. B., Poglitsch A., Sternberg A., Townes C. H., 1991, ApJ, 373, 423

Stacey G. J., Hailey-Dunsheath S., Ferkinhoff C., Nikola T., Parshley S. C., Benford D. J., Staguhn J. G., Fiolet N., 2010, ApJ, 724, 957

Sutherland R. S., Dopita M. A., 1993, ApJS, 88, 253

Swinbank A. M., Karim A., Smail I., Hodge J., Walter F., Bertoldi F., et al., 2012, MNRAS, 427, 1066

Tielens A. G. G. M., Hollenbach D., 1985, ApJ, 291, 722

Turk M. J., Smith B. D., Oishi J. S., Skory S., Skillman S. W., Abel T., Norman M. L., 2011, ApJS, 192, 9

van der Tak F. F. S., Black J. H., Schöier F. L., Jansen D. J., van Dishoeck E. F., 2007, A&A, 468, 627

Vázquez G. A., Leitherer C., 2005, ApJ, 621, 695

Velusamy T., Langer W. D., 2014, A&A, 572, A45

Waagan K., 2009, Journal of Computational Physics, 228, 8609

Wakelam V., Herbst E., 2008, ApJ, 680, 371

Walch S., Girichidis P., Naab T., Gatto A., Glover S. C. O., Wünsch R., Klessen R. S., Clark P. C., Peters T., Derigs D., Baczynski C., 2015, MNRAS, 454, 238

Wiesenfeld L., Goldsmith P. F., 2014, ApJ, 780, 183

Wilson N. J., Bell K. L., 2002, MNRAS, 337, 1027

Wolfire M. G., Hollenbach D., McKee C. F., 2010, ApJ, 716, 1191

Wünsch R., Walch S., Dinnbier F., Whitworth A., 2018, MNRAS, 475, 3393

Xu D., Li D., Yue N., Goldsmith P. F., 2016, ApJ, 819, 22

Table 3. Same as Table 2Summary of the parameter space of the [C II] emitting gas, analysed for the optically thin [C II] line emission. We give the values of T_{kin}, n, the fractional abundance of H_2 (x_{H_2}), and the visual extinction (A_V) at which 25%, 50% (median) and 75% of the total luminosity are reached. The corresponding plots are shown in Figs. 7*Upper row, left:* Plot of the optically thin [C II] line luminosity originating from gas with $T \leqslant T_i$ for the total map (solid line) and the assumed observable region (dashed line). The cyan line represents the expectation if all of the C^+ ions were in LTE. The red shaded area and the grey, dashed vertical line mark the interquartile range and the median of the distribution derived for the total map. *Upper row, right:* The slope of the cumulative luminosity distribution, derived by taking the derivative of the luminosity with respect to the temperature. Most of the emission comes from $40 \lesssim T \lesssim 60$ K. *Bottom row, left:* Mass-weighted temperature distributions of the included species. $M_i/M_{\mathrm{species, \, tot}}$ indicates the mass fraction of every species with respect to the total hydrogen, carbon or electron mass, respectively. All collisional partners (H_2, H, e^-) coexist in the gas from which most of the [C II] line emission stems, although H is the most abundant one, followed by H_2. *Bottom row, right:* Mass-weighted excitation coefficients for every species (Eq. (A9RADMC–3Dequation.A.9)) as a function of the temperature. For $T < 40$ K collisions with H_2 dominate, whereas for $T > 40$ K collisions with H contribute most to the [C II] line emission. figure.caption.10 and 10Total (solid line) and observable (dashed line) luminosity of the optically thin [C II] line emission originating from the gas distinguished by its number density with $n > n_i$ (first row), its fractional abundance of H_2 (x_{H_2}; middle row), and its visual extinction (A_V; bottom row). In the left column, we show the cumulative distribution and in the middle column its derivative. Note that dense gas appears on the left-hand side of the x-axes. The right column depicts the mass-weighted species distributions (see Section 4.1Temperature dependencesubsection.4.1). The red shaded area and the grey, dashed vertical line mark the median and the interquartile range for the emission of the total map. figure.caption.13. The results are presented for the whole map and the observable region (where $I_{\mathrm{[CII]}} \geqslant 0.5$ K km s^{-1}). table.caption.8, but analysed for the opacity affected [C II] line emission. The values of the parameters are similar to the optically thin [C II] line emission. However, note that the results of the opacity affected [C II] line emission overestimate the total emission. This table is included here for the sake of completeness.

[C II], opac. aff.	taken pixels	L/L_{tot} $\geqslant 25\%$	$\geqslant 50\%$	$\geqslant 75\%$
T_{kin}	total	44 K	53 K	65 K
	observable	40 K	47 K	55 K
n	total	62 cm^{-3}	193 cm^{-3}	490 cm^{-3}
	observable	131 cm^{-3}	292 cm^{-3}	610 cm^{-3}
x_{H_2}	total	0.08	0.13	0.20
	observable	0.11	0.16	0.22
A_V	total	0.48	0.64	0.84
	observable	0.57	0.72	0.90